Influence of Zr, Cr and Sc alloying on the microstructure and mechanical properties of a Al-Mg-Si casting alloy

Vom Fachbereich Material- und Geowissenschaften

Der Technischen Universität Darmstadt

Zur Erlangung des Grades

Eines Doktors der Ingenieurwissenschaften

(Dr.-Ing.)

genehmigte Dissertation von

Prach Olena, M.Sc.

Aus Saporischschja, Ukraine

Hauptberichterstatter: Prof. Dr.-Ing. Karsten Durst

Nebenberichterstatter: Prof. Dr.-Ing. habil. Carolin Körner

Tag der Einreichung: 12.02.2020

Tag der mündlichen Prüfung: 09.06.2020

Darmstadt

Prach, Olena: Influence of Zr, Cr and Sc alloying on the microstructure and mechanical properties of a Al-Mg-Si casting alloy

Darmstadt, Technische Universität Darmstadt,

Jahr der Veröffentlichung des Dissertations: 2021

URN: urn:nbn:de:tuda-tuprints-172138

Tag der mündlichen Prüfung: 09.06.2020

Erklärung zur Dissertation

Hiermit versichere ich, die vorliegende Dissertation ohne Hilfe Dritter nur mit den angegebenen Quellen und Hilfsmitteln angefertigt zu haben. Alle Stellen, die aus Quellen entnommen wurden, sind als solche kenntlich gemacht. Diese Arbeit hat in gleicher oder ähnlicher Form noch keiner Prüfungsbehörde vorgelegn.

Darmstadt, den 10 März 2020

X

Olena Prach

Table of Contents

List of Acronyms

Symbol	Definition
ISO	International Organization for Standardization;
ASTM	American Society for Testing and Materials;
HPDC	High-Pressure Die Casting;
HT	Heat Treatment;
ST	Solution Treatment;
AA	Artificial Aging;
SSS	Supersaturated Solid Solution;
GP-zones	Guinier-Preston zones;
G	Shear modulus;
b	Burgers vector;
c	Foreign atom content in at. %;
r	Radius of spherical precipitate;
l	Average free spacing between precipitates;
TC	Thermo-Calc;
SEM	Scanning Electron Microscopy
TEM	Transmission Electron Microscopy
DSC	Differential Scanning Calorimetry ;
T_{onset}, T_{offset}, T_{peak}	Temperatures of the begin, end and peak of a reaction;
k	Partition coefficient;
DAS, ILS	Dendrite Arm Spacing and Interlamella Spacing;
HB, HV	Brinell hardness and Vickers hardness;
YS, UTS	Yield Strength and Ultimate Tensile Strength, MPa;
A	Elongation, %

Chapter 1

Introduction and Objectives

Increases in wealth and in the world population lead to the production of more products made from metal with steel being the most frequently used metal in the world, in spite of its relatively high density. Consequently, medium and high strength aluminum alloys are becoming increasingly popular in order to reduce weight and improve efficiency. The use of light metals in the transport sector reduces the total weight of a vehicle, leading to lower fuel consumption and significant savings in fuel usage and pollution. Additionally, aluminum is easy to recycle, with only 5 percent of the energy used to produce primary aluminum required for the recycling of it [1]. Intriguingly, approximately 75 % of all aluminum ever made is still in use [2,3]. Hence, light metals and in particular Al-alloys are becoming increasingly important and can be a good substitution for steel in the same applications.

Light-weight Al-alloys are important nowadays for energy saving and for fuel efficiency improvement in the transportation sector. Al-Mg-Si wrought alloys are widely used in the automotive industry because of their excellent strength potential [4–6] due to the ability of Mg and Si to form nanosized particles (otherwise known as precipitation hardening) during heat treatment (HT). Al-Mg-Si alloys, referred to as 6xxx of wrought alloys [7], are shaped in a soft condition, usually by extrusion or rolling, before being age hardened to their final strength.

With regard to cast products; more than 90% of today's aluminum castings are based on Al-Si, a binary system which provides excellent castability at low cost, leading to widespread employment of the alloy in the automotive industry [8]. Al-Mg-Si casting alloys are not so widely used as compared to the 6xxx series of wrought alloys. In recent years, several Al-Mg-Si casting alloys, with commercial names Hydronalium 511, Magsimal®59, Maxxalloy and Maxxalloy Ultra, Aural11 have been developed. These alloys are increasingly being used in the automotive and aerospace sectors, due to their good castability, corrosion resistance on one the hand and excellent mechanical properties in the as-cast state [9–12].

Optimisation of alloy properties is a never ending task, due to the appearance of new industrial and technical challenges. The aim of this thesis is to improve the mechanical properties of the commercially available alloy Magsimal®59 (Rheinfelden, Germany) by means of alloying of the base composition with Sc, Cr and Zr, all of which are known to have promising characteristics.

An addition of scandium to aluminum alloys, even in a rather small amount (up to 0.2 – 0.3 wt. %), significantly increases its strengthening due to the formation of fine coherent precipitates of Al_3Sc and it is comparable to the addition of several percentages of magnesium. Moreover, grain refinement can be achieved by Sc addition to Al-alloys [13–16]. Only a few studies, however, have been published for Al-Mg-Si casting alloys with scandium addition.

The first systematic development and investigation of Sc-containing alloys took place in the former USSR in the 1980s with an interest for scandium as a constituent in aluminum alloys, reaching the western world approximately 10 years later [13,17]. Even though a number of improvements of Al alloys have been demonstrated through the addition of scandium current use of such alloys is still very limited as a consequence of the very high price of scandium [17]. Zirconium (Zr) which also alone gives improved workability and formability of Al alloys is cheaper than Sc and is a relatively common alloying element today. Chromium (Cr) is commonly used for grain structure control in wrought Al-alloys to provide reduced susceptibility to stress corrosion and improve material toughness.

The main objectives of the work are as follows:

- To increase the knowledge of Sc-containing aluminum alloys as well as Zr- and Cr-containing alloys in general and to gain more insight about how single additions of Sc, Zr affects the microstructure and properties of Al-alloys.
- Taking into account the high price of the Al-Sc master alloys and of pure Sc (even a small addition of it can essentially increase the price of the alloy), an important motivation of this research is to explore the possibility of full or partial Sc substitution by Zr and/or Cr.

Thus, the main goal of this research is to make an attempt to obtain similar mechanical properties for the alloys containing Zr, Cr or their combination and Sc additions. In order to reach this goal, a number of different Sc, Zr-Cr and Sc-Zr containing alloys have been produced and investigated with respect to the improvement of mechanical properties and precipitation behaviour.

This research has been funded by German Academic Exchange Service (DAAD) and was done in cooperation with another DAAD scholarship holder Oleksandr Trudonoshyn. All investigated alloys have been produced at Friedrich-Alexander-Universität Erlangen-Nürnberg (FAU), Erlangen Germany. Moreover, Differential Scanning Calorimetry (DSC), Electron Microprobe Analysis (EMPA) and the thermodynamic calculations have been performed at FAU.

Chapter 2

Aluminum alloys: General Background

In the first part of this chapter, an overview of the general aspects of aluminum alloys, their classification and heat treatments along with the casting techniques is presented. In the second part, the main strengthening mechanisms employed in the aluminum alloys will be briefly discussed. The literature review of Al-M-Si system alloys and the effect from an alloying element on the final properties are presented in the concluding part of this chapter.

2.1 Application of Aluminum alloys

Aluminum alloys possess a lot of attractive characteristics such as high strength, good corrosion resistance, excellent workability, and high thermal and electrical conductivity, which together with their lightweight and high strength-to-weight ratio make them extremely attractive for many applications. The major fields of application are [18–21]:

- transportation;
- packaging/consumer market;
- building and construction;
- electrical engineering;
- others (high-pressure gas cylinders, machined components, ladders and access equipment, bicycles, sporting goods, road barriers and signs, lithographic plates).

The changes in the application fields for 2007 in comparison to 2015 are shown in Figure 2.1.

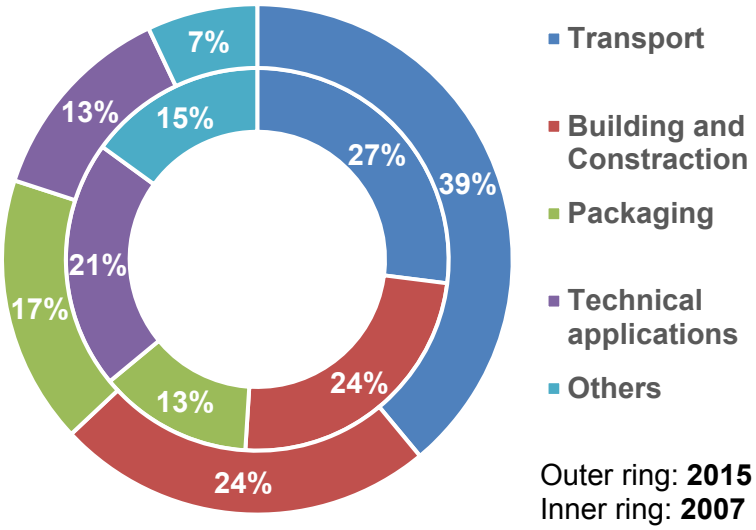

Figure 2.1 Fields of the application of Al alloys in 2007 and 2015 as for comparison, adapted from [22].

The successive replacement of heavy cast iron components in the automotive industry by lighter cast and wrought aluminum alloys is increasing the world rate production (**Figure 2.2**). Over 80% of energy consumption and corresponding emissions are associated with the automotive industry. The goal is to reduce the energy consumption during the life cycle of a vehicle by weight reduction. The present trends show that aluminum becomes a key material: 1 kg of aluminum replacing 2kg of heavier materials (steel or cast iron) in a car or in a small truck can save 20 kg of CO_2 over the life of the vehicle or up to 80 kg CO_2 in trains [23,24]. The demand for lightweight construction will increase intensity of use: in the year 2000 each automotive vehicle contained on average 100-120 kg of aluminum; in 2012 it was around 158 kg; by 2025 it is expected to be 250 kg [25,26]. During the last decade, the European automotive industry has more than doubled the average amount of aluminum used in passenger cars and this amount will continuously increase in the future [27]. An average of 102 kg aluminum was used in automotive parts in Western Europe in the year 2000 with 59 kg in engine parts, 11 kg in structural parts, 6 kg chassis applications and 5 kg for body-in-white[*](21 kg others).

[*] Car body with all joined together body's components before painting or further assembling.

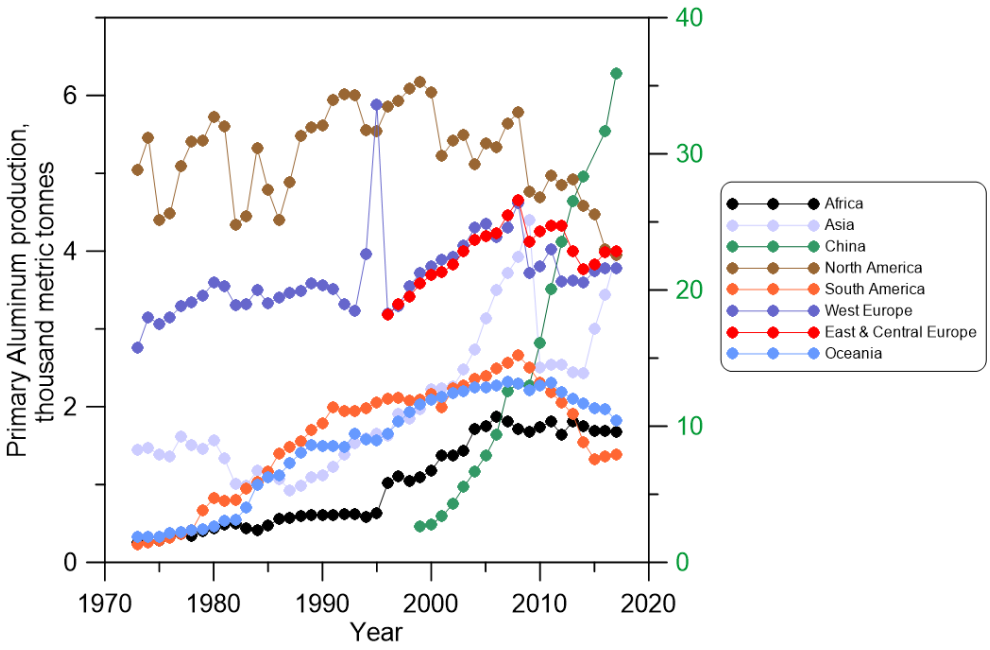

Figure 2.2 World aluminum production, adopted from [18].

Figure 2.3 shows an average amount of semi-product of aluminum alloys in a vehicle including demand for cast alloys. About 660 million tonnes of greenhouse gases could be saved during the use phase if all transport units (including road vehicles, trains and aircraft) were replaced by lightweight vehicles of a current design with the same functional properties [24,28].

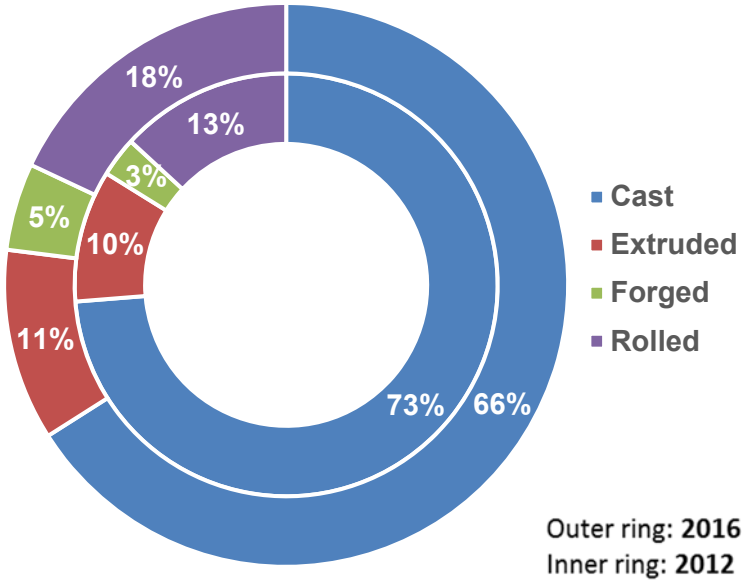

Figure 2.3 Semi-product of aluminum alloys, adapted from [22].

2.2 Casting of aluminum alloys

The main driving force behind the development of aluminum alloys is the growing requirement of the weight reduction of structures, increased cost-effectiveness and environmental friendliness of parts production in the automotive and aerospace industries [29,30]. This determines the progress in the development of new casting technologies and the development of new alloys adapted to modern casting processes. At the same time, the main direction in the investigations of new alloys is, first of all, their versatility and the possibility of obtaining good mechanical properties, regardless of the casting technology that has been applied. The main demands for casting aluminum alloys are good corrosion resistance, high level of mechanical properties (ultimate tensile strength (UTS), yield strength (YS), and elongation (A)) and, of course, good castability. The optimization of these properties depends on a number of factors during casting, including formation of hot cracking, fluidity in the molten state and the minimization of shrinkage porosity.

Casting is the original and most widely used method of forming aluminum into products [31]. Technical advances have been made, but the principle remains the same: molten aluminum is poured into a mold to duplicate the desired geometry. The final mechanical properties are effected by alloy microstructure, which in turn depends on cooling rate. Thus, this parameter should be controlled for each casting technique. The three most important techniques are die casting, simple permanent mold or gravity casting and sand casting (which belong to the expandable mold processes). Figure 2.4 schematically shows the existing casting processes. In the present work all alloys have been prepared using a high-pressure die casting (HPDC) machine equipped with a cold chamber.

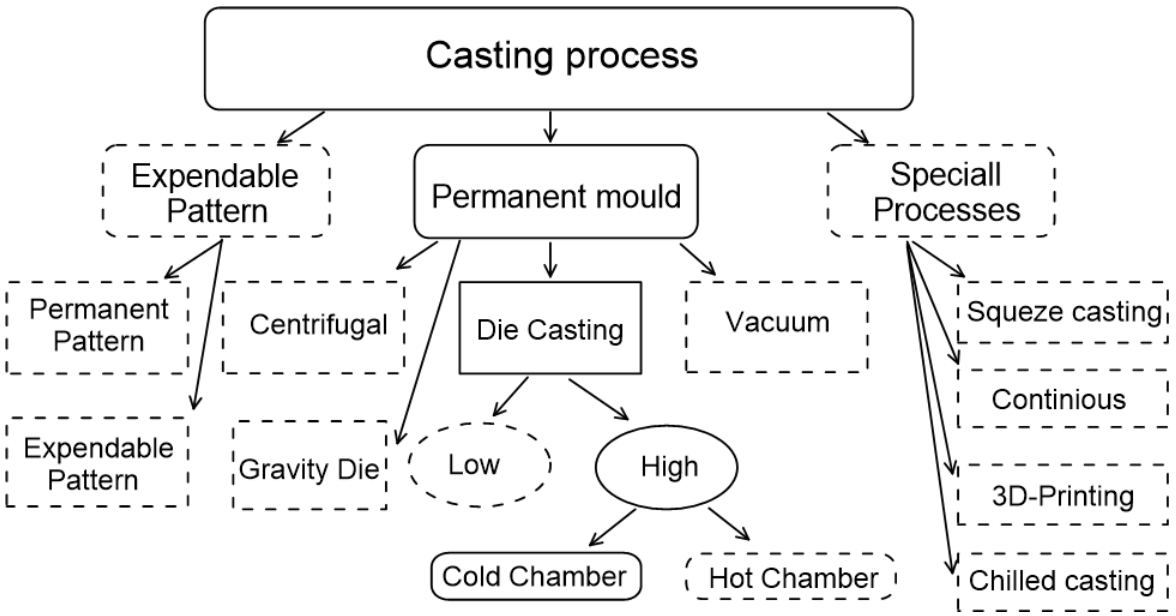

Figure 2.4 Classification of the casting techniques. Adopted from [31]

High Pressure Die casting (HPDC)

High pressure die-casting is a widely spread casting technique, representing around 50% of the total aluminum production. Nowadays the products for automotive front-end structures and instrument panels are cast by this technique, mostly from magnesium or Al-Si alloys. However, for HPDC and for some complex geometries it can be difficult to achieve acceptable fatigue properties due to the presence of porosity in the cast component.

During HPDC the molten aluminum is feed into a steel die (mold) under a pressure (low or high) [32]. This manufacturing technique is normally used for high-volume production because precisely formed aluminum parts requiring a minimum of machining and finishing can be produced through this casting method (R_a=2.5-1.25 μm)[31]. Die-cast components can be produced in a wide range of alloy systems, including aluminum, magnesium, zinc, lead, and brass.

Two basic die casting approaches exist:

- A hot-chamber process, where a significant portion of the metal injection system is immersed in the molten metal at all times. The main feature of this process is the minimization of cycle time. (**Figure 2.5a**).

- In a cold-chamber die casting machine the metal injection system is only in contact with the molten metal for a short period of time (**Figure 2.5b**). Liquid metal is ladled into the shot sleeve for each cycle [32]. A typical casting cycle of HPDC used in this work can be found in Appendices (**A.1**).

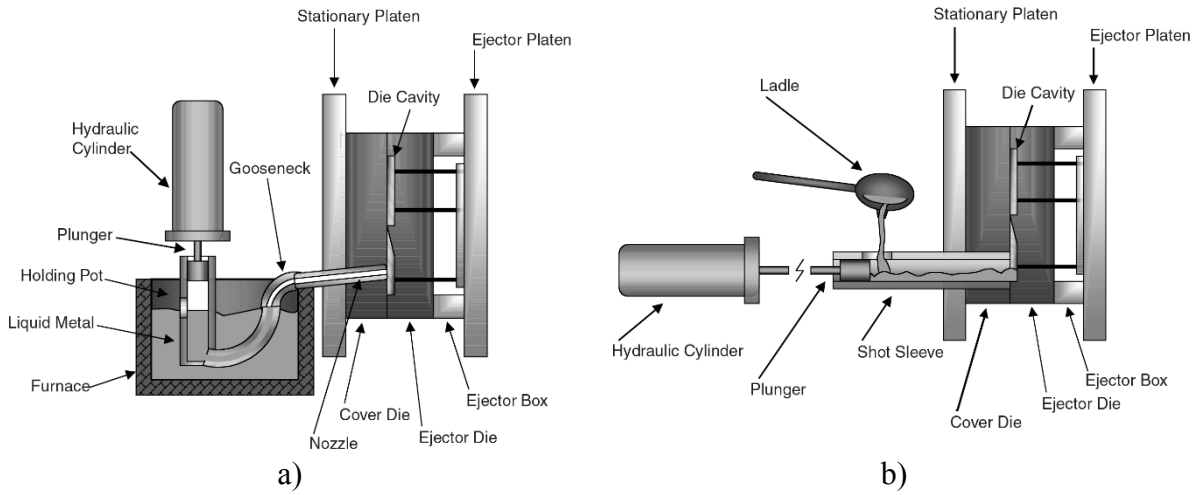

a) b)

Figure 2.5 Graphical illustration of a) hot-chamber, b) cold-chamber die casting machine[32]

In spite of a long list of advantages and great potential the HPDC process has a major limitation, which prevents its use on a broader scale. HPDC is notable for short cycle times and a high speed of solidification. As a consequence, dissolved gases do not have enough time to coalesce and form porosity. Thus, a common defect which can be found in cast is porosity, which is caused by trapped gases. It limits the use of the HPDC in favour of products fabricated by other means, either "dictate" a form and complexity of the cast. In spite of all advantages of the HPDC, the main flaw of this casting technique is a hidden porosity, which detection is rather difficult. This hidden porosity can be detected only by subsequent machining or after heat treatment [32–34]. However, in some cases, a small amount of porosity in as-received component is acceptable.

Porosity is attributed to two main sources: solidification shrinkage and gas entrapment [32,35]. Mainly alloys have a higher density in their solid-state as compared to their density in the liquid state. As a consequence, shrinkage porosity forms during solidification. Also, due to the turbulent manner in which metal enters and fills the die cavity, gas often becomes entrapped in the metal, resulting in porosity. The presence of porosity highly negatively affects the

mechanical properties, load bearing capacity and durability of the final product as it acts as a stress concentrator creating initiation sites for fracture and fatigue cracking.

Three solidification zones, formed during casting in a cast mold, are schematically shown in **Figure 2.6a**. In the close to the edge region (mold/metal interface) the solidification speed is high due to the comparative low temperature of mold and surrounding temperature. As consequence, many small grains nucleate and form an outer equiaxed zone. The small grains closer to the middle part of cast increase in size, becoming dendritic, develop long dendritic arms and form a columnar zone (**Figure 2.6b**). In the centre part of the casting another equiaxed zone is usually formed due to the remaining undercooling liquid. More detail on the solidification process can be found in [36]. A microstructure containing aluminum dendrites in the investigated alloy is shown in **Figure 2.6c**. The three-dimensional shape of the dendrites can be observed from the micro shrinkage cavities in **Figure 2.6d**.

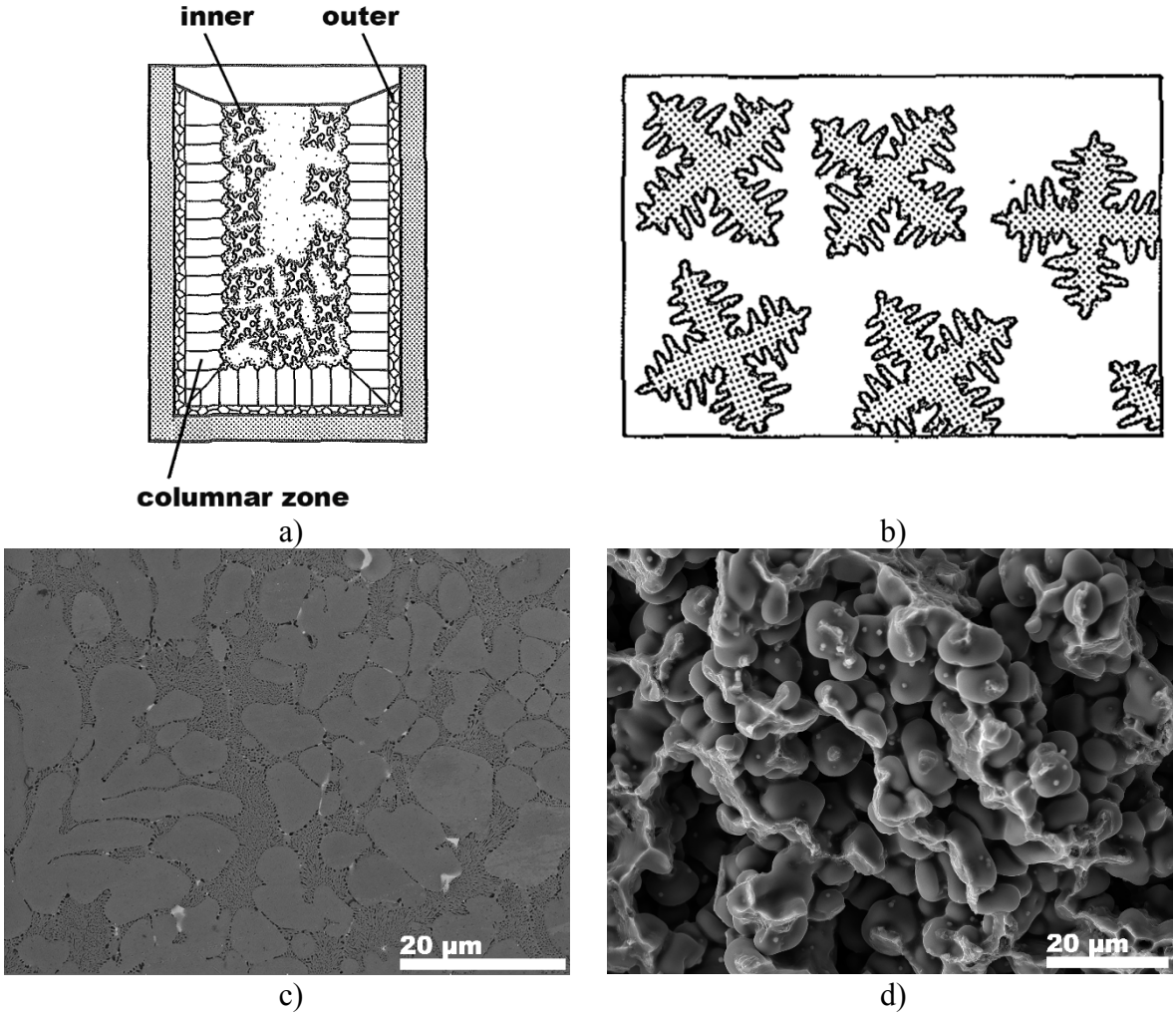

Figure 2.6 a) Structural zone formation in castings [36], b) dendritic arms [36], c) SEM image of dendrites in Al-Mg-Si alloys (present work), d) SEM image of aluminum dendrites in the fractured surface of a tensile test bar of the Al-Mg-Si alloy (present work).

2.3 Classification, heat treatment and strengthening mechanisms of aluminum alloys

Aluminum alloys are classified by many different organizations. For example, some common aluminum alloy compositions are registered with the Aluminum Association (AA). Currently, there are over 400 wrought aluminum and over 200 aluminum alloys in the form of castings and ingots registered with the Aluminum Association. On the other hand, many other organizations publish more specific standards for the manufacturing of aluminum alloys, including the Society of Automotive Engineers Standards and the ASTM (American Society for Testing and Materials). Alternatively, aluminum alloys can be classified by a number system

(e.g., ANSI) or by names indicating their main alloying constituents (e.g., DIN and ISO) [7,37,38].

Aluminum alloys can be categorized into a number of groups based on the particular material's characteristics, such as its ability to respond to thermal and mechanical treatment, and based on the primary alloying element, which is added to the aluminum alloy. And, as it was mentioned earlier, all aluminum alloys can be divided into two main groups, depending on the manufacturing method, e.g. wrought and casting aluminum alloys. Table 2.1 shows the series and systems of the aluminum casting alloys according to the Aluminum Association. In contrast to the wrought systems, casting alloys do not use 6XX.X series and Al-Mg-Si belongs to the 5XX.X of casting alloys.

Aluminum alloys are classified as heat treatable or non-heat treatable, depending on, whether they respond to precipitation hardening or not [8,38]. The heat treatable alloys contain elements that decrease in solid solubility with decreasing temperature, and in concentrations that exceed their equilibrium solid solubility at room temperature and moderately higher temperatures [38].

To the heat treatable alloys belong the following systems: Al-Cu (2XX.X), Al-Si-Mg (3XX.X), Al-Zn (7XX.X) and Al-Sn (8XX.X). Mechanical properties of heat treatable alloys (strength, ductility, toughness, residual stress, resistance to corrosion, etc.) can be significantly improved by heat treatment [35,39]. In Table 2.1 a heat treatment and temper designation system of aluminum alloys are presented. This classification of wrought and cast aluminum alloys has been implemented by the Aluminum Association.

In addition to the basic temper designation, there are two subcategories, one addressing the "H" Temper – Strain Hardening, and the other addressing the "T" Temper – Thermally Treated designation. More information can be found in Appendices (A.2) [38].

Table 2.1 Classification of casting aluminum alloys according to Aluminum Association (AA) and European Norms, [38]

Series	System	Precipitation hardening/ Heat treatment	Tensile strength range, [MPa]
1XX.X	Al	non heat treatable alloys	75
4XX.X	Al-Si		228-296
5XX.X	Al-Mg		276-310
8XX.X	Al-Sn		138-221
2XX.X	Al-Cu	heat treatable alloys	220-470
3XX.X	Al-Si-Cu		160-270
	Al-Si-Mg		160-345
6XX.X	unused		-
(5XX.X)	Al-Mg-Si		240
7XX.X	Al-Zn-Mg		241

Al-Si alloys are the most usable system for engineering applications due to their fluidity since they are close to eutectic composition. These alloys are remarkable due to a high corrosion resistance and good weldability. On the other hand, one of the most useable systems from wrought alloys is the Al-Mg-Si system, while for casting alloys this system is not widely applicable. Several alloys, which belong to the Al-Mg-Si casting system in accordance with the DIN EN 1706, are used in manufacturing. They have a high strength and ductility in the as-cast state as well as the ability to be strengthened by heat treatment.

Heat treatment

Solution treatment

Solution treatment is used in order to eliminate segregation of elements in the cast structure. Microsegregation results in the formation of concentrated micro-inhomogeneity and non-uniform distribution of alloying elements and impurities across the volume [8,40,41]. The prediction of non-equilibrium segregation and phase stability as a function of cooling rate within castings can be done using Scheil equilibrium [41,42]. On the other hand, microsegregation depends on the partition coefficients, which can be defined as the slope of the liquidus over the slope of the solidus lines in a binary phase diagram of the particular elements

in aluminum [42–44]. **Figure 2.7** shows the SEM image of the Al-Mg-Si-Sc-Zr alloy with the corresponding EDX maps of Mg, Si, Sc, Zr. Moreover, the evolution of composition as a function of distance along the measured line is presented. The partition coefficient can be less or exceed 1, thus, the elements segregate differently. In the case of k is close to 1, the element has little tendency for segregation in the Al (such as Mn see **Figure 5.6** and Sc see **Figure 2.7** [45]). The segregation coefficient of Zr exceeds 1 and is mostly enriches the dendritic core. Thus, Mg as well as Si, which have a segregation coefficient in Al less than 1 (~0.5 and ~0.1 respectively) [42,46], enrich the dendritic edge and mainly accumulate in the eutectic regions (**Figure 5.6**).

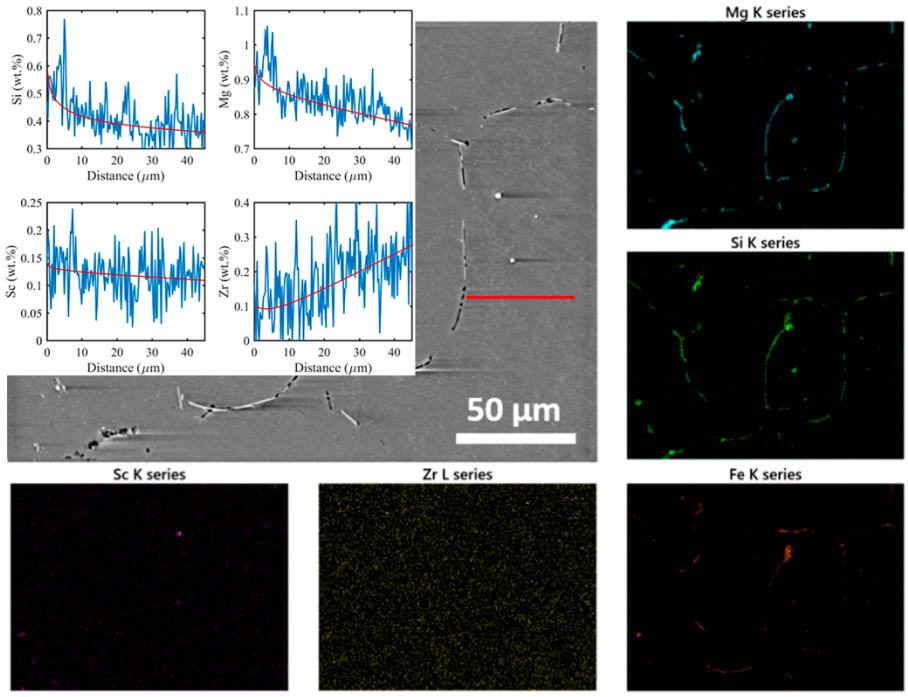

Figure 2.7 SEM image of the Al-Mg-Si-Sc-Zr alloy with the EDX maps of Mg, Si, Sc, Zr and composition vs distance along the line [45].

In order to minimize such inhomogeneity, solution treatment (ST) or homogenization of the part can be done. The following processes during ST of aluminum alloys take place [8]:

1. Dissolution of non-equilibrium phases and corresponding constituent particles.
2. Elimination of concentration inhomogeneity for the alloying elements (micro segregation).
3. Changes in phase composition and constituent particle morphology.
4. Changes in grain and dislocation microstructures of aluminum solid solution.

5. Decomposition of aluminum solid solution in the course of isothermal heat treatment accompanied by the formation of dispersoids* (in alloys containing additions of transition metals).

Usually, for a solution treatment, temperatures between the solvus and the solidus are used. For casting and wrought aluminum alloys temperatures in range of~ 450 - 650°C (Figure 3.11 b) are used. Moreover, this procedure requires rapid cooling (e.g. quenching in water) for the formation of a super saturated solid solution (SSS) and further precipitation formation [17,38,47,48]. The change of the Mg_2Si lamellar shape morphology during solution treatment in hypoeutectic Al-Mg_2Si alloy is shown in **Figure 2.8**.

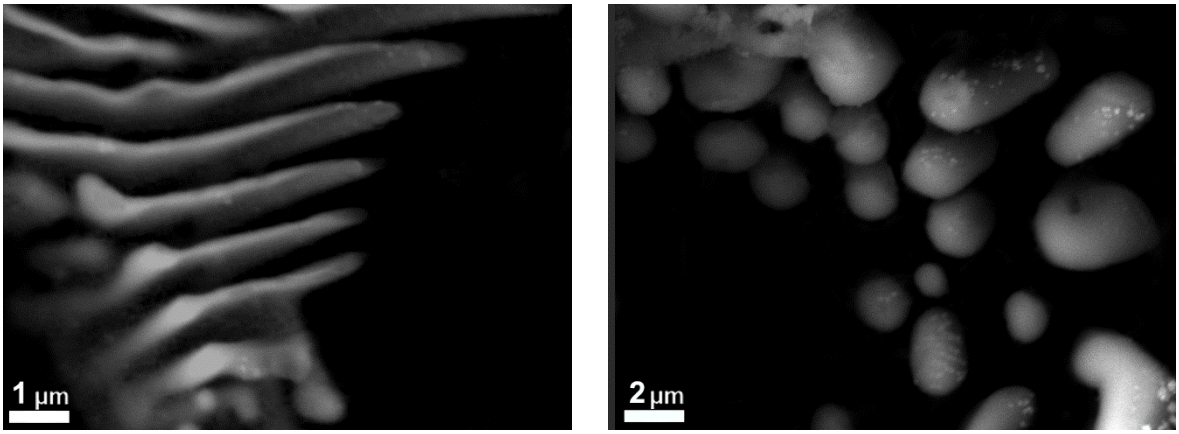

a) b)

Figure 2.8 Morphology of the Mg_2Si eutectic in the a) as-cast Al-Mg_2Si alloy and b) after solution treatment at 575°C [49].

Artificial Aging

Aluminum alloys are usually subjected to aging either natural or artificial aging. Artificial and natural aging can be applied to Al alloys. Natural aging is industrially used for alloys that display the most significant changes in microstructure and properties over a period of a few days at room temperature (< 4 days). The T1–T3 tempers correspond to heat treatment immediately after casting, and the T6–T7 tempers refer to immediate quenching after ST. Consequently, the original (i.e., before aging) microstructure could be as-cast or obtained after homogenization and quenching [8]. Decomposition of SSS (in order to obtain fine

* In this work term "dispersoids" is used to define precipitates with a diameter of 10-500nm, which have been formed during solution treatment in a range of 400-550ºC.

strengthening precipitates) is controlled by aging. A detailed study on precipitation sequence in the Al-Cu system can be found in the following works [50,51]. Edwards *et al.* provided an explicit research on the precipitation formation on 6061 alloy [52].It was found that such fine precipitates can significantly improve yield and tensile strength of alloys.

Strengthening mechanisms

The following chapter gives a summarized overview of strengthening mechanisms in the Al-alloys. Background can be found in [53,54].

Figure 2.9 represents all strengthening mechanisms which can take place in wrought and cast Al alloys [50]. Usually, in alloys for structural application several mechanisms are used. In contrast to wrought alloys, cast alloys cannot be exposed to any kind of deformation such as plastic deformation or work hardening. Thus, the mechanical properties of a cast alloy are a result of casting parameters (casting technique, heating and cooling rate etc.), alloying elements and heat treatment. In the casting alloys the following strengthening mechanisms can take place: two-phase strengthening, precipitation strengthening, and/or solid solution strengthening. The resulting tensile yield strength is the sum of these mechanisms.

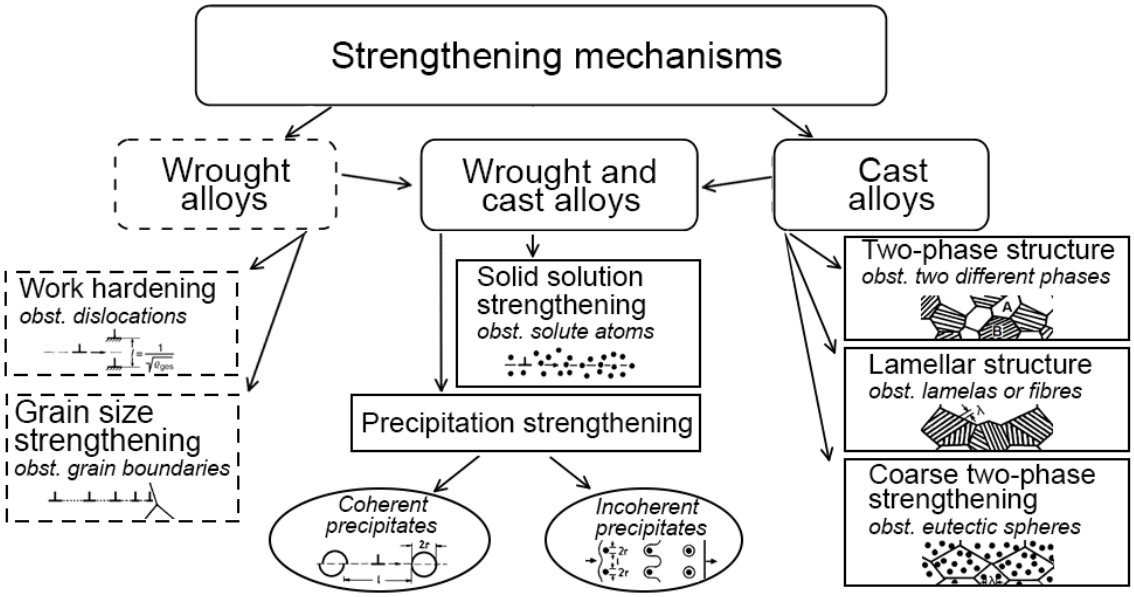

Figure 2.9 Schematic representation of a strengthening mechanisms in Al. Adopted from [50]

2.3.1 Solid solution strengthening

When foreign atoms are dissolved in a lattice, they can act as additional obstacles to dislocation movement, thus increasing the strength of the base material. Such strengthening is called solid solution strengthening and is the easiest mechanism of strengthening of Al. In general, all existing series of aluminum alloys (regardless of wrought or cast alloy) are strengthened by solid solution.

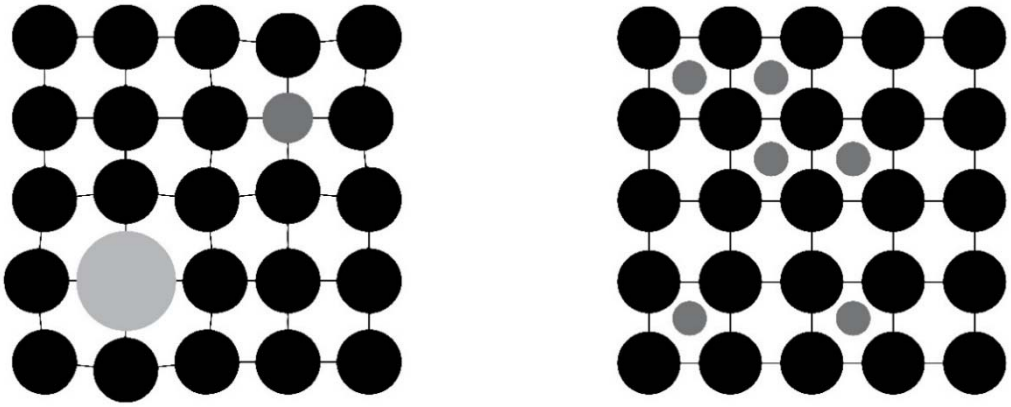

a) b)

Figure 2.10 Different types of solid solutions a) Substitutional and b) interstitial solid solution. Adapted from [55].

Depending on the position of solute atoms in the lattice sites, they can be categorized as substitutional and interstitial solid solution. In the first case the solutes replace atoms of the solvent in the crystal lattice (**Figure 2.10 a)**, whereas in the second case the foreign atoms sit in interlattice positions between the original atoms (**Figure 2.10 b**).

Substitutional atoms act as an obstacle for dislocation movement, thus the size of these atoms plays an important role. If the dissolved atoms are larger than the host atoms, they produce compressive stresses in their vicinity, whereas smaller substitutional atoms produce tensile stresses (**Figure 2.10 a**).

A first investigation on the solid solution hardening of Al alloys was undertaken by Mott and Nabarro in 1948 and later by Fleischer in 1963. Labusch then implemented changes to Fleischer's theory, in which the strengthening was evaluated through statistical consideration of the interaction between dislocation and solute atoms [56].

The solubility of alloying elements in Al binary systems at room temperature and melting point is summarized in Table 2.2.

Table 2.2 Summary of alloying elements used in this study, their solubility at different temperatures and their classification [44,57–59]

System	Eutectic (e) / peritectic (p) temperature, °C	Maximum solubility, wt. %	
		at eutectic/peritectic melting point	at 20°C
	high solubility		
Al-Mg	450 (e)	17.4	<1.9
Al-Si	577 (e)	1.65	<0.01
Al-Mn	660 (p)	1.82	~0.05
	low solubility		
Al-Zr	660 (p)	0.28	-
Al-Cr	660 (p)	0.8	-
Al-Sc	665 (e)	0.27	<0.20
Al-Fe	652 (e)	0.03-0.05	<0.01

The effect of the presence of Mg and Mn in solid solution on the mechanical properties in commercial alloys has been discussed by Reyn *et.al.* [60]. Elements with high solubility in Al (*e.g.* Mg, Si, Mn) provide the main contribution to solution strengthening of the material.

It was experimentally determined that the relationship between strengthening and concentration of the dissolved element in the material can be written as:

$$\Delta\sigma_{SSH}=Hc^{n} \qquad (2.4.1)$$

where c is the concentration of an element in the solid solution, n is a constant that depends upon the nature of interaction between the solute and dislocation (n is in the range 0.5 to 0.75) and H is the solid solution hardening coefficient [40,60].

According to Fleischer's theory n = 0.5 for a weak pinning of dislocations, where solute atoms act as point defects that resist dislocation motion [56,61]. Whereas, for a stronger pinning of dislocations according to Labusch's theory n = 2/3 [56,62].

2.3.2 Precipitation hardening

The age hardening potential of Al-Cu alloys was discovered by Alfred Wilm who, in 1906 developed a new Al-3.5–5.5%Cu-Mg-Mn alloy, with the commercial name Duralumin [63]. Precipitation hardening can be achieved either by heat treatment (solution treatment in order to dissolve the second phase with rapid cooling down to precipitate nanoparticles and following artificial aging) or at room temperature with time, so-called natural aging. The heat treatments have been previously discussed in Chapter 2.3.

Age hardening takes place in alloys for which the solubility of the solute element increases with decreasing temperature. In the case of Al-Mg-Si, with the eutectic temperature around 595°C, it is necessary to treat the material with a temperature close to eutectic to dissolve all Mg and Si atoms into the aluminum matrix. With a fast cooling rate from near eutectic temperature down to room temperature, there will not be sufficient time for precipitation. As a consequence, a supersaturated solid solution (SSS) is obtained. This sequence creates a driving force for precipitation of a second phase since the temperature and solute fraction determines the two-phase region in the phase diagram. This means that the supersaturated solid solution is not energetically stable. It was found that a long-term natural aging between SSS and further artificial aging can lead to the formation of addition Mg/Si cluster [52,64]. Afterwards, the alloy should be aged in order to achieve precipitation formation in the matrix.

The precipitation sequence in Al-Mg-Si systems is:

SSS → transition structure (GPI and GPII zones and β″) → aged phase (β′ and β-Mg_2Si)

The sequence of precipitation is decomposition of the energetically unstable supersaturated solid solution (SSS) and the formation of GP-Zones. These zones are needles oriented in the <001> direction; they are rather stable and can exist up to 260 ºC [44,65,66]. A detailed study on GP in Al-Mg-Si alloys was done by Matsuda *et.al.* [67]. During the next stage of ageing the formation of a needle and rod-like intermetallic phase, so-called β″ and β′ particles take place. These particles are semi-coherent, and the rod axes are parallel to [001]. As a final

stage, the Mg_2Si phase (β) is formed as incoherent platelets. The density of GP zones can be up to 10^{17}-10^{18} cm^{-3} [52,67–70]. Different crystallographic relationships between matrix and second phase are depicted in **Figure 2.11 a-c**.

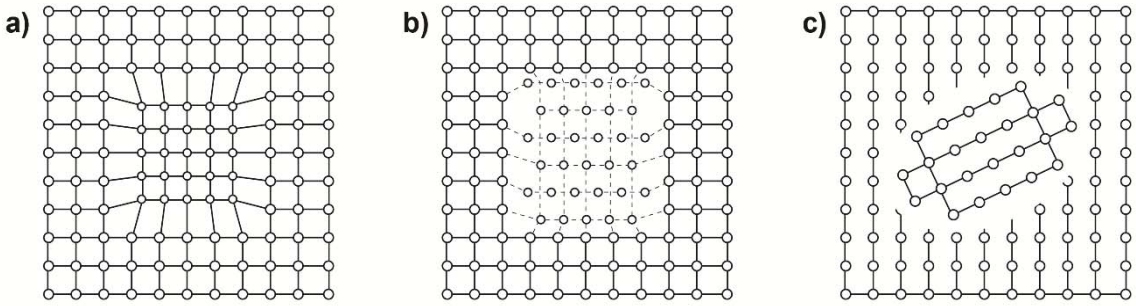

Figure 2.11 Crystallographic relationships between matrix and second phase. a) coherency with strained, but continuous, lattice planes across the boundary, b) semicoherent, c) incoherent equilibrium precipitate. Adapted from [54,66]

During precipitation hardening fine particles are formed due to the changes in solid solubility with temperature and time. These particles impede the movement of dislocations in a crystal's lattice. The basic mechanisms of precipitate-dislocation interactions are the Friedel effect (cutting) and Orowan bowing (looping). **Figure 2.12** schematically shows both mechanisms.

Dislocations can move through the matrix, regardless of the strength of the obstacles. While bypassing the precipitates, the dislocation is pinned by the obstacles. At the same time, the remaining part of the dislocation tries to move further, two sides of one dislocation encounter and annihilate one another, due to the opposite orientation, resulting in a dislocation loop around the obstacle and a free dislocation. The Orowan mechanism is shown schematically in **Figure 2.12**.

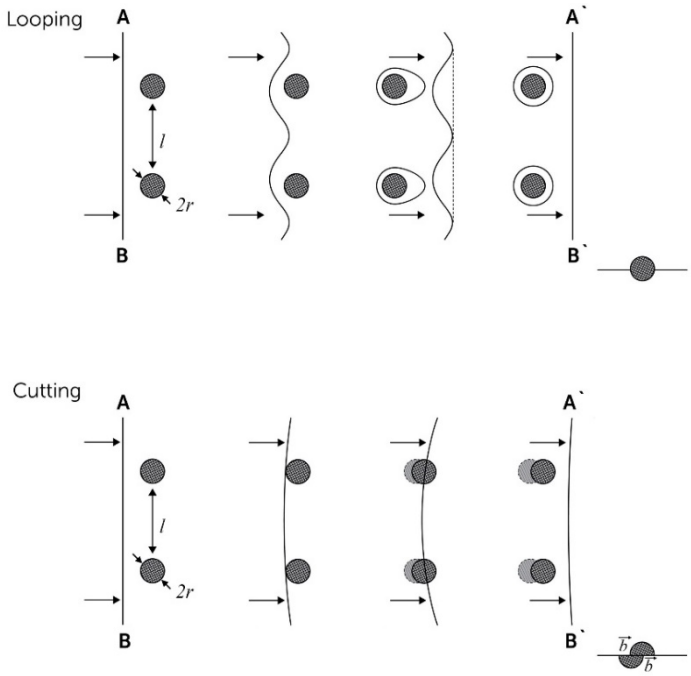

Figure 2.12 Schematic illustration of interaction mechanisms between dislocations and precipitates: particle looping and particle cutting. Adapted from [71].

The process of overcoming an obstacle is called the Orowan mechanism. The stress required to bend and loop a dislocation is inversely proportional to the interspacing *l* or to a radius *r* of the particles in the matrix [66]:

$$\tau \approx \frac{Gb}{l} = \frac{Gb}{2r} \tag{2.4.2}$$

where *G* is the shear modulus and b the Burgers vector.

In case the strength of the obstacle is not sufficient to retain the dislocation, the dislocation passes through the obstacle. Cutting of particles is easier for small coherent particles that tend to behave as segregated solute atoms. Cutting and shearing of the obstacle is shown in **Figure 2.12**.

In other words, during the initial stage, as precipitation or aging continues, the precipitate particles increase in size and volume. With an increase in size and amount of particles, more work needs to be done by the dislocation in shearing the particles. Thus, the shear strength τ of the alloy depends on the particle radius r and the particle volume fraction f according to the proportionality [66]:

$$\tau \approx \sqrt{rf} \tag{2.4.3}$$

The size (radius) of the precipitate plays an important role in the strengthening mechanism. In the case of small particle size, dislocations cut the precipitate. For particles with large sizes, dislocations bypass (Orowan bowing) the particles. Particle bypass results in a high density of dislocation loops, thus leading to a higher work hardening rate. In addition, strength is strongly dependent on particle size (**Figure 2.13**).

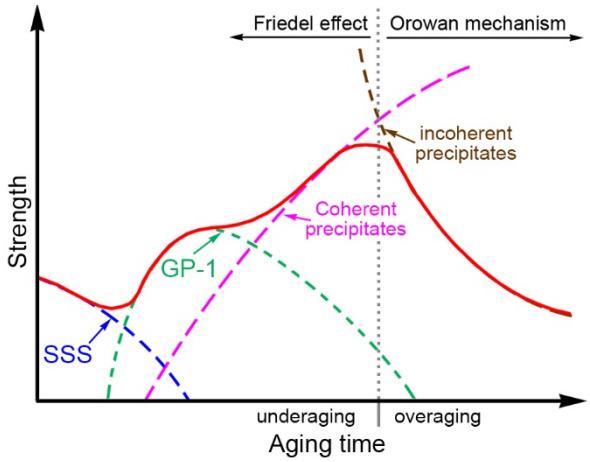

Figure 2.13 Strength vs size of particles, adopted from [50,51].

The strength vs size curves in **Figure 2.13** can also be described as age-dependent and divided into two stages. The first stage is under-aging and the second is over-aging. During the first stage, the strength constantly increases, whereas during the second stage, the strength gradually starts to decrease. During the second stage, where the material is already over-aged, dislocations are forced to loop around the precipitates due to their large size, and the yield strength decreases.

Chapter 3

Al-Mg-Si alloys

In this chapter, a literature overview on the equilibrium phase diagrams of Al-Mg-Si system will be provided. Phase diagrams are visual representations of the state of alloys as a function of temperature and concentrations of the alloying elements. The analysis of the phase diagram is the starting point for the design of new alloys, their development, processing, and basic understanding. For the thermodynamic and phase diagram calculations of multi-component systems the Thermo-Calc (TC) software has been used (TCAl2: Al-alloys v2.1 database)[*].

Several possible compositions for new casting alloys have been proposed in the literature, and analysis of multicomponent phase diagrams of their systems is presented below.

3.1 Effect from the main alloying elements in aluminum alloys

As was mentioned earlier the degree of solubility of an element in the matrix can bring about a different strengthening effect. Here the main alloying elements will be considered:

Magnesium

As noted previously, Al-Si casting alloys become heat-treatable by addition of magnesium, due to the formation of a Mg_2Si hardening-phase. Magnesium has good solid solubility in aluminum and reaches (up to 0.7wt% of Mg) a maximum value of 17.4% at the eutectic temperature of 450°C [44]. It is well known that the addition of magnesium to aluminum increases strength by solid solution strengthening. Due to the high corrosion resistance and attractive combinations of strength and ductility of the binary Al-Mg alloys, they are widely used in marine constructions and, because of their excellent response to chemical finishing treatments, in applications requiring a bright surface finish. Common compositions

[*]The calculations have been performed at the Friedrich-Alexander-Universität Erlangen-Nürnberg (FAU), Material Science Department (WTM), Erlangen Germany.

range from 4 to 10% Mg, and compositions containing more than 7% Mg are heat treatable [31].

Investigation of the influence of Mg addition on the Al-Si system led to the development of a series of new casting alloys containing a fundamentally new combination of elements. In these alloys, the phase equilibria are shifted to the magnesium-enriched region. Wrought alloys of Al-Mg-Si system (alloys of 6XXX series, 6061, etc.) are the most widely used.

Al-Mg alloys “Magsimal-59” Rheinfelden Aluminum, Germany, "Maxxalloy 59" SAG, Austria and Aural 11 Alcan, as well as 515 and 518 Al-Mg alloys have been developed for die casting. These alloys have good mechanical properties on the as-cast state as well as after heat treatment and self-aged conditions. Alloys 515 and 518 in the as-cast state have almost doubled values of strength ranges as compared to the A356 (Al-Si alloy) in the as-cast state [72].

Silicon

Al-Si base alloys are the most popular casting alloys, due to improvement of casting characteristics, caused by Si addition to Al. Addition of silicon significantly improves fluidity (castability) and feeding characteristics, reduces hot-brittleness, and decrease the melting point. Si has a high solubility in Al, 1.65 wt. % of Si can be dissolved at the eutectic temperature, while the eutectic reaction occurs at 12.6 wt. % Si and 577°C. The amount of Si content should be chosen according to the casting process. For processes with a higher-solidification-rate such as pressure die and permanent mold casting and especially for thin walled casting, with a rapid solidification, the typical silicon concentration varies between 8.00 wt. % and 12.00 wt. %.

The ultimate tensile strength of pure Al (99.9999) is 78 MPa [73]. Si addition in the amount of 7.00 wt. %, increases UTS up to 210 MPa. Commercial Al-Si alloys can be divided depending on the Si content into the hypoeutectic and hypereutectic (up to 30% Si) [38]. Silicon itself is a brittle material and due to the negligible amount of Mg in the Al-Si alloys a brittle, needle-shaped Al+Si eutectic and primary Si phases can be formed [74]. As a consequence, Al-Si alloys have rather low mechanical properties in the as-cast state (with elongation to failure only around 3% in the as-cast state and unmodified Al-Si eutectic [38]). Nevertheless, it was found that the eutectic can change its morphology from long plates to fine acicular fibers when small amounts of Na or K as well as Sc are added to the melt or after heat treatment [75,76].

Si with Mg can form Mg_2Si in heat treatable alloys. It interacts with iron and other elements forming complex insoluble phases. Al-Si alloys, even with a low amount of Mg (in comparison to wt. % of Si) and with or without Cu addition belong to the 3.XXX series of heat treatable alloys. These alloys, especially in T6 condition, show significant increase in the mechanical properties in comparison to Al-Si casting alloys [77].

Manganese

Manganese improves the strength of Al alloys by means of solution strengthening. The main aim of Mn in casting alloys, however, is to bond Fe and Si. These elements are harmful for aluminum, due to their low solidification range, which can lead to the formation of needle-shaped brittle particles [78–80]. These iron-rich phases lead to a degradation of mechanical properties, in particular ductility. Addition of Mn to such alloys leads to changes in the morphology of Fe-containing phases from its typical platelet/acicular to a more cubic phase that is less harmful to ductility in Al-Si, Al-Si-Mg and Al-Mg-Si alloys [81–85]. The absence of Mn, or even low concentrations thereof, result in the formation of intermetallic compounds such as α-(Al_8Fe_2Si) phase, π-($Al_8FeMg_3Si_6$) phase and especially the β-phase (Al_5FeSi). These phases are considered to be detrimental to the ductility of the material [80,81,85]. The β-phase has a needle shape form and usually can be found in the interdendritic regions. All of these phases behave as a stress concentrators, which lead to degradation of mechanical properties of the cast part. In the Al-Mg-Si wrought alloy, Mn binds with Fe and promotes the formation of fine-scale dispersoids, which are identical to the α-Al(Mn,Fe)Si phase [86]. In the HPDC Al-Mg-Si alloys, Mn suppresses the formation of the needle-shaped β-AlFe phase and modifies it to a compact cubic α-AlFeMnSi phase [84].

3.2 Al-Mg-Si alloy system

The first and the most substantial overview of the Al-Mg-Si phase diagram was given by Mondolfo [57]. A more detailed analysis of the Al-Mg-Si system was performed later by several authors [4,59,87–91].

The main attribute of the Al-Mg-Si system is the presence of a pseudobinary cross-section around 13.9 wt. % Mg_2Si, in which the ternary system can be considered as binary [90]. Pseudobinary cross-section can be defined as a vertical section between a congruently melting binary compound, pure Al on one side and Mg_2Si on the other, where congruent melting is

defined by the fact that the composition of liquid and the solid phase is the same. **Figure 3.1** shows the aluminum rich side of the Al-Mg-Si phase diagram with the pseudobinary cross section (marked as a red line) [91]. According to Kumar *et al* [88], the Al-Mg_2Si section is not exactly pseudobinary due to a Mg content twice as high as the Si content in the eutectic maximum. It was found that actual pseudobinary section is shifted to the Mg-rich side (**Figure 3.1**, dashed line A-A') and has a melting point of 595°C. This statement was also experimentally proven by Barabash [4]. Reactions which take place during melt solidification are shown in Table 3.1 [88,92,93].

An excess of Mg (at. % Mg/Si > 2.0) in the Al-Mg-Si system moves the eutectic point to the Al-rich side (**Figure 3.1**a) [81,94]. The microstructure of hypereutectic alloys consists of α-Al matrix, eutectic and primary Mg_2Si crystals. It was found that Mg excess in Al-Mg_2Si alloys can effect formation of the Mg_2Si primary crystals. Moreover, the increase of Mg content in the alloy leads to a decrease in a volume fraction of the α-Al matrix and, as a result, to increase in the volume fraction of Al-Mg_2Si eutectic [94–96]. **Table 3.1** and **Figure 3.1c** present all existing reactions, which take place in the Al-Mg-Si system.

An excess of Si in aluminum alloys effects the Mg and Si diffusion into the Al. With Si increase in the Al-Mg_2Si-Si composites, the crystallization range is also increased. It is well known that Si excess in aluminum alloys can lead to the decrease of the mechanical properties such as ductility due to formation of silicide and brittle secondary needle-shaped phases [81]. Nonetheless, alloys with the Si excess which have been heat treated show significant improvement in their mechanical properties (namely, tensile strength and ductility) [81,97].

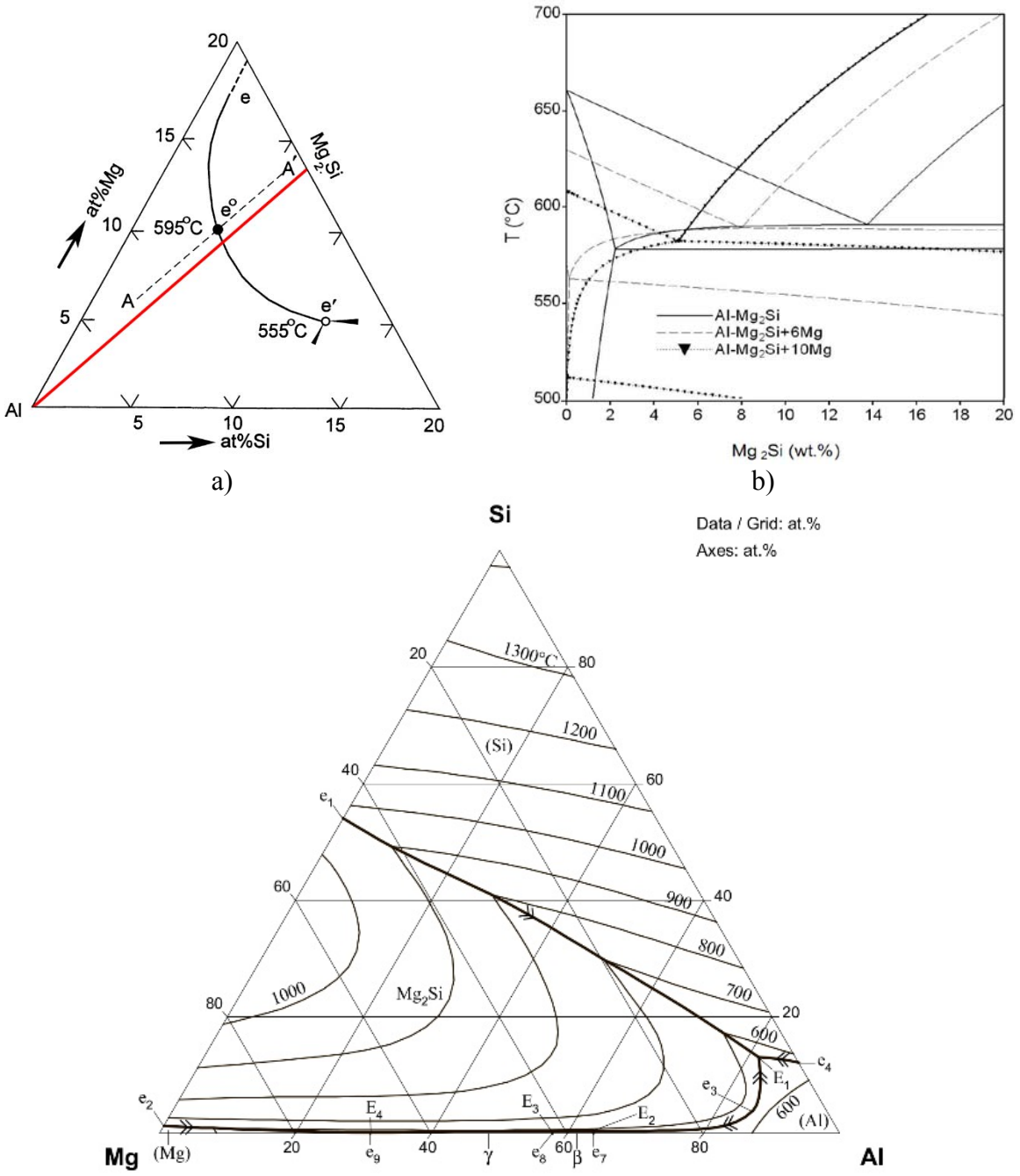

a) b)

Figure 3.1 a)Ternary Al-Mg-Si diagram with the pseudobinary line (red) and an experimentally established an invariant line of L → (Al) + Mg_2Si (black curved line), b) binary Al-Mg2Si phase diagram, showing an influence of excess Mg [94] and c) Al-Mg-Si Liquidus surface [88].

Table 3.1 Reactions, which take place in Al-Mg-Si system [88,92,93]

№	Reaction			Temperature, [°C]		Type
1.	**L → (Al) + Mg_2Si**			**594**		**e_3**
	Composition, [at%]	Phase	Al	Mg	Si	
		L	85.3	10.8	3.9	
		(Al)	97.1	2.7	0.2	
		Mg_2Si	0	66.7	33.3	
2.	**L → (Al) + (Si) + Mg_2Si**			**557**		**E1**
	Composition, [at%]	Phase	Al	Mg	Si	
		L	81.5	5.4	13.1	
		(Al)	98.0	0.70	1.3	
		(Si)	0	0	100.0	
		Mg_2Si	0	66.7	33.3	
3.	**L → γ + Mg_2Si**			**462,5**		**e_5**
	Composition, [at%]	Phase	Al	Mg	Si	
		L	46.1	53.8	0.1	
		γ	46.1	53.9	0	
		Mg_2Si	0	66.7	33.3	
4.	**L → β + Mg_2Si**			**451,2**		**e_6**
	Composition, [at%]	Phase	Al	Mg	Si	
		L	61.0	38.9	0.1	
		β	61.1	38.9	0	
		Mg_2Si	0	66.7	33.3	
5.	**L → (Al) + β + Mg_2Si**			**450**		**E_2**
	Composition, [at%]	Phase	Al	Mg	Si	
		L	64.0	36.3	0.1	
		(Al)	83.4	16.5	$4.0 \cdot 10^{-6}$	
		β	61.1	38.9	0	
		Mg_2Si	0	66.7	33.3	
6.	**L → β + γ + Mg_2Si**			**449**		**E_3**
	Composition, [at%]	Phase	Al	Mg	Si	
		L	57.4	42.5	0.1	
		β	61.1	38.9	0	
		γ	51.9	48.1	0	
		Mg_2Si	0	66.7	33.3	
7.	**L → (Mg) + γ + Mg_2Si**			**435,6**		**E_4**
	Composition, [at%]	Phase	Al	Mg	Si	
		L	30.9	69.0	0.1	
		(Mg)	11.6	88.4	$5.5 \cdot 10^{-5}$	
		γ	39.9	60.1	0	
		Mg_2Si	0	66.7	33.3	

3.3 Commercial Al-Mg-Si casting alloys

Hypoeutectic wrought alloys of the Al-Mg-Si system are widely used due to their relatively high strength. Alloying by other elements does not lead to a silicide formation, because of low Si content, therefore a wide range of elements can be used for the improvement of the mechanical properties. The first and most widely used is alloying by manganese. It is well known that addition of Mn provides a solution strengthening effect, even more so after heat treatment of 6XXX wrought alloys. Manganese binds with iron and forms Mn-containing dispersoids [86].

Notwithstanding the fact that wrought aluminum alloys of the Al-Mg-Si system are still more popular than casting alloys, during the last years several commercial alloys, namely Hydronalium 511, Magsimal®59 [10], Magsimal Plus, Maxxalloy and Maxxalloy Ultra, Aural11 [12] have been developed and are increasingly used in the automotive and aerospace industries for critical structural applications. This is in large part due to their excellent castability and corrosion resistance and, in particular, high mechanical properties in as-cast state. The nominal chemical composition is almost the same for all of these alloys: 5.00 wt. % Mg, 2.00 wt. % Si and 0.60 wt. % Mn (**Table 3.2**) [98]. In comparison to the most useful, successful and popular casting alloy A356 (AlSi7Mg0.3) with 0.3 wt. % Mg, 7 wt. % Si, this composition provides a high strength and ductility in the as-cast state (**Table 3.3**). Recently, an alloy with improved composition from Rheinfelden Alloys GmhH & Co. Magsimal-59Plus, with a Zr content of 0.1-0.3% (**Table 3.2**) has been released. Mg concentration is increased in order to avoid the presence of free Si in the microstructure. This Mg/Si ratio promotes around 40% of Mg_2Si eutectic fraction [99], which leads to an improvement in corrosion resistance and mechanical properties in as-cast state (UTS up to 348 MPa and uniform elongation up to 10%).

Table 3.2 Chemical composition of commercial casting alloys (Al-balance)

Alloy	Elements content, wt. %						
	Si	Mg	Fe	Mn	Cu	Ti	Other
Maxxalloy	1.8-2.6	5.0-6.0	0.45-0.9	0.5-0.8	0.08	0.05-0.15	Be
Magsimal-59	1.8-2.5	5.0-5.8	0.15	0.5-0.8	0.05	0.15	Be
Magsimal Plus	2.1-2.6	6.0-6.4	0.15	0.5-0.8	0.05	0.05	Zr
Aural 11	1.8-2.2	4.0-5.0	0.15-0.22	0.5-0.6	0.03	0.04-0.08	
Hydronalium	1.0	5.0	0.3	0.2	-	0.1	-
A356	6.5-7.5	0.2-0.45	0.6	0.35	0.25	0.25	Zn

Al-Mg-Si casting alloys possess good corrosion resistance, weldability, high quality surface finish and high mechanical properties in the as-cast condition. Alloys with the nominal composition AlMg5Si2Mn produced using HPDC show a high level of elongation (up to 18%), yield strength (up to 220 MPa) and ultimate tensile strength (up to 340 MPa) in comparison to other casting alloys (**Table 3.3**).

Table 3.3 Mechanical properties of commercial alloys [12,100,101]

Alloy	Young's Modulus, GPa	Tensile Strength, MPa	Yield Strength, MPa	HB	Elongation %
Maxxalloy	75	210-250	100-145	70-85	7-10
Magsimal-59 (wall thickness 6-12mm)	70-80	220-260	120-145	70-85	8-12
Magsimal-59 (wall thickness 2-4 mm)	-	160-220	310-340	-	12–18
Magsimal Plus (wall thickness 3 mm)		200-220	340-360	-	9-12
Hydronalium	65-75	193	90	77	8
A356	71	220	120	75	2

For the development of new alloys, the commercial Magsimal®59 alloy has been used as a base. This alloy belongs to the Al-Mg-Si system of alloys according to DIN EN 1706 and is widely used in the Europe, particularly in the automotive industry [10,11,102]. In recent years, it has gained even more popularity in comparison to the A356 alloy (which belongs to the 4.XXX system of casting alloys) due to its relatively high strength in the as-cast state and rather low porosity level in the thin-wall cast, which results in good weldability [103].

The commercial alloy Magsimal®59 belongs to the hypoeutectic alloy category and contains 6 wt. % of Mg_2Si and ratio of Mg to Si ≥2.0 (in at. %). Minor additions such as Mn, Zr and Sc do not significantly affect the Al-Mg_2Si system equilibrium. Due to the low solubility of the alloying elements in Al, a new primary phase is formed, significantly changing of the mechanical properties.

Thermodynamic calculations of the Al-Mg-Si alloys

In order to understand phase formation in the new alloys, Magsimal®59 which will be used as the base alloy, will be discussed in the following chapter. **Figure 3.2a** shows the binary phase diagram for Al-Mg_2Si. As was mentioned previously, in this diagram the equilibrium point is slightly moved to the Al-rich side. However, due to the presence of other alloying elements, this diagram should be recalculated in accordance with the chemical composition of interest in this work. The Al-5Mg-2Si-(0…2.0)Mn binary phase diagram, calculated using the Thermo-Calc approach for the base alloy, is shown in **Figure 3.2b**. The calculated phase diagram should be considered as a quasi binary phase diagram. The left side of phase diagramm presents Al-5Mg-2Si rich side with increasing Mn-content on the concentration axis. $Al_{15}(MnFe)_3Si_2$ forms during eutectic reaction at 623°C and 0.6 wt. %. Thus the purple line in **Figure 3.2b** shows the solubility of Mn in Al-5Mg-2Si. The straight lines (yellow and brown) indicate the formation temperature of α-Al and Mg_2Si phases, which are not affected by the Mn concentration. Whereas with an increase of Mn concentration, the formation temperature of $Al_{15}(MnFe)_3Si_2$ continuesly increases (purpule line). In this alloy system the following phases can be observed: α-Al, β-Mg_2Si, and Mn-containing phases usually reported as $Al_{15}(MnFe)_3Si_2$ [104].

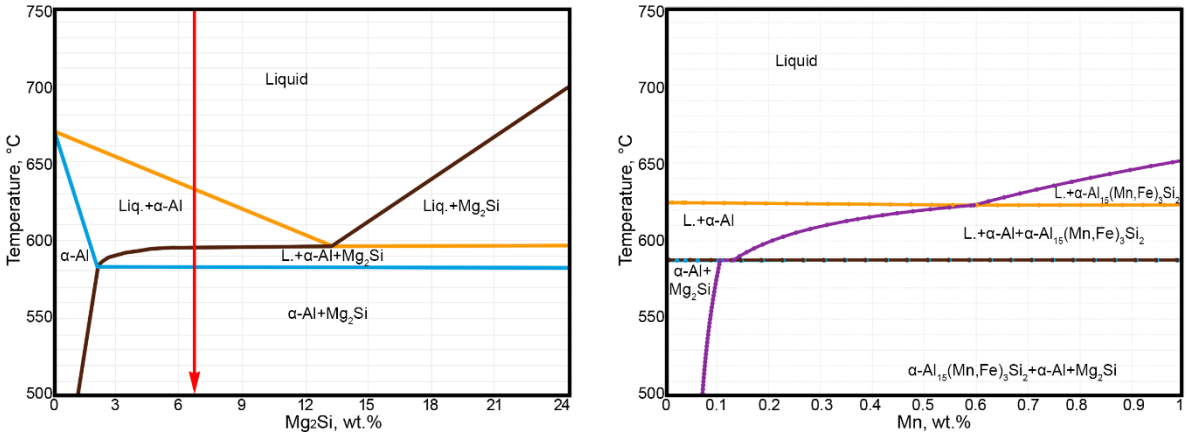

a) b)

Figure 3.2 Binary phase diagram a) Al-Mg_2Si, the investigated alloy is marked with arrow, adapted from [87] and b) calculated Al-5Mg-2Si-(0…2.0)Mn phase diagram.

Reactions and temperature formations of the existing phases for investigated alloy during solidification are presented in **Table 3.4**.

Table 3.4 Sequence of the reactions in the alloy during equilibrium solidification

TºC	Reaction
624	$L+ Al_{15}(MnFe)_3Si_2$
615	$L+ Al_{15}(MnFe)_3Si_2 + Al$
591	$Al_{15}(MnFe)_3Si_2 + Al+ Mg_2Si$

3.4 Effect of minor alloying elements on Al-Mg-Si alloys

Transition metals (Cr and Zr)

The addition of Cr to aluminum alloys has a significant influence on the microstructure. Cr in aluminum typically forms the compound $CrAl_7$ [105], which has low solubility. Cr, as well as Mn, can be used in order to prevent the harmful effect of Fe on aluminum alloys. In the following works [86,106,107] it was mentioned that Cr can be added in order to control the grain structure in Al-Mg alloys and to prevent recrystallization in Al-Mg-Si and Al-Mg-Zn alloys. Moreover, chromium improves corrosion resistance and toughness in certain alloys and increases quench sensitivity at higher concentrations [44,108].

An addition of Zr is commonly used for Al-Zn-Mg-Cu alloys, because of their ability to improve corrosion resistance, increase grain refinement and improve the mechanical properties [109]. It was reported that Zr has a positive effect on the Al-Mg-Si alloy due to the formation of cubic and tetragonal Al_3Zr precipitates [109–111]. Moreover, Zr is used in order to replace Ti, as it can also behave as a refining additive, increasing the recrystallization temperature. Moreover, in combination with Sc, it can form strengthening $Al_3(Sc,Zr)$ particles[112–114].

G. Timelli *et al.* [115] reported that Cr, as well as Mn, is tied up with trace elements, thus penetrating the already existing phase and forming the α-$Al_x(Fe,Mn,Cr)_ySi_z$ intermetallic phase. Consequently, such intermetallic particles with irregular distribution and chaotic clustering can act as stress concentrators resulting in material failure at relatively low stresses.

Scandium

The addition of Sc to aluminum leads to the formation of a supersaturated solid solution in $\alpha-Al$ during solidification. After its decomposition during aging above 300°C, highly dispersed coherent cubic-shaped Al_3Sc precipitates will be formed [44,58].

Even a small amount of Sc in aluminum alloys (0.20-0.30 wt. %) can make a significant contribution to the strength of an alloy, comparable with several percentages of magnesium [16]. Sc has a grain refining effect, leading to the formation of small equiaxed grains instead of long dendrites, and furthermore reduces hot-cracking. It was found that the hypereutectic addition of Sc (>0,55wt%) to Al leads to the formation of fine spherical grains instead of large dendritic grains [116].

The first publications of the Al-Sc phase diagram in English were presented by Savitsky in 1964 [117] and Naumkin *et al.* in 1965 and later published in the second edition of the Mondolfo handbook [44]. A more plausible phase diagram was proposed by Drits *et al.* in 1973. With further investigations, the Al-Sc diagram underwent minor changes [118,119] and Okamoto presented the latest phase diagram for Al-Sc, shown in **Figure 3.3a** [120]. The Al-rich side of the Al-Sc phase diagram can be found in **Figure 3.3b** and to date small differences in the maximum solid solubility and melting point can be found. Thus the maximum solid solubility at eutectic concentration ~38 wt. % occur at the melting point of Al (660°C), which is nearly equal to the eutectic temperature [17,44,121]. Scandium is observed to have a low solubility in Al, which is typical for transition metal additions to Al [57,58].

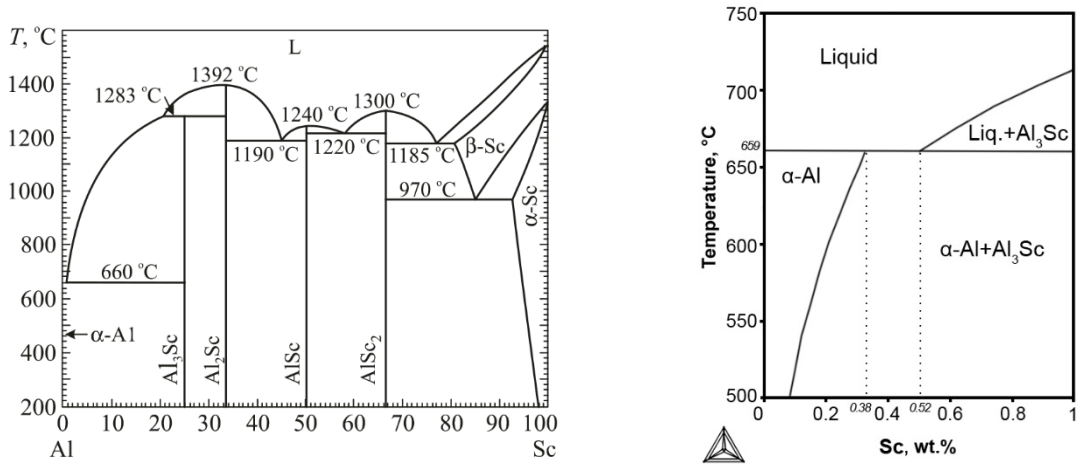

a) b)

Figure 3.3 a) Al-Sc phase diagram [120], b) Al-rich side of Al-Sc diagram calculated by Thermo-Calc.

With the decomposition of the Al(Sc) solid solution, highly stable, cuboidal, and coherent Al_3Sc precipitates form. They have an equilibrium morphology consisting of 6 {100}, 12 {110}, and 8 {111} facets, which form a great rhombicuboctahedron [122]. Al_3Sc precipitates are coherent and highly stable in the α-Al matrix due to their high melting temperature as compared to Al [119]. These precipitates have an ordered $L1_2$ -type structure, where Sc atoms sit at the corner sites and Al atoms sit on the faces of a fcc lattice (**Figure 3.4**).

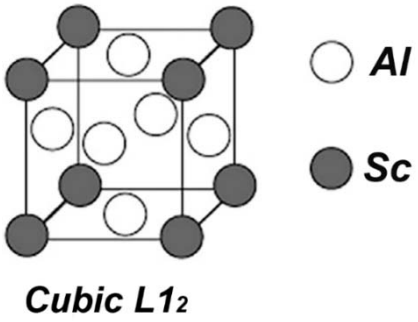

Figure 3.4 Scheme of the $L1_2$-type structure of Al_3Sc precipitates

An extensive study of existing commercial alloys with the addition of Sc has was performed by J. Røyset [17]. Commercial wrought aluminum alloys containing Sc have been compared to alloys with the same chemical composition excluding Sc. Almost all Sc containing alloys show a doubling of the values for ultimate tensile strength and yield strength in comparison to those which have not been alloyed by Sc.

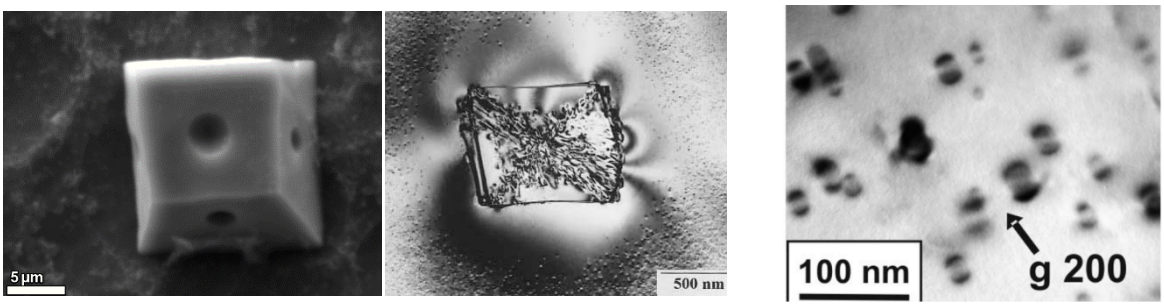

a) b) c)

Figure 3.5 a) SEM image of Al_3Sc particle found in Al-2Sc master alloy [123], b) TEM bright-field image of the Al_3Sc particle in Al-0.7Sc alloy [116] and c) TEM bright-field image of Al_3Sc precipitates [111].

Until now no commercial Al-Mg-Si casting alloy exists with scandium. Only a few references to work on the commercial Al-Si-Mg casting alloys with Sc addition were found [15,16]. In the following literature [122,124–126] Al_3Sc precipitation behaviour in the Al-Sc and Al-Mg-Sc casting alloys have been investigated. Dang *et al*. [127] reported that the strongest effect on the tensile strength in commercial Al-Mg alloy is an addition of Sc and alloying with Zr is the next one. It was also found that the positive effect on the mechanical properties of the Al-Mg-Si alloys is due to the grain refinement effect of Sc [128].

Figure 3.5 presents the morphology of the Al_3Sc particles and precipitates formed during heat treatment. **Figure 3.5a** shows primary Al_3Sc particles found after deep etching in the Al-2Sc master alloy [123]. Binary Al-Sc alloys with the amount of Sc (0.7Sc) exhibit the cusped cubic shapes of primary Al_3Sc particles [116,129] (**Figure 3.5b**). It was established that size and morphology strongly depend on the Sc content and the composition of the alloy. Litynska *et al* (**Figure 3.5c**) reported that the size of the primary Al_3Sc particles varies from 60 to 80 nm and has a spherical morphology for the alloys containing up to 0.4wt% Sc.

Alloys from the Al-Mg-Si system experience precipitation hardening by formation of Mg_2Si nanoscale precipitates after the T6 regime. This regime includes solid solution treatment close to the melting temperature, followed by water quenching, and then artificial aging at comparatively low temperatures. On the other hand, Al_3Sc precipitates form at 250-350°C [13]. As a consequence, determining an optimal heat treatment regime that enables the combination of precipitation hardening of Al-Mg-Si alloys with precipitation hardening of Al_3Sc presents significant challenges.

Zirconium

Al and Zr form a peritectic diagram, the Al-rich side of which is shown in **Figure 3.6a**. The solubility of Zr in aluminum is very low, ~ 0.083 at. % (0.28 wt. %) at peritectic reaction (see also **Table 2.2**), L+Al_3Zr→Al, which takes place at 660.8°C [44,57,130,131]. The Zr-rich precipitates can form a semi-coherent tetragonal equilibrium phase or as Al_3Sc a coherent cubic structure which is shown in **Figure 3.6b**.

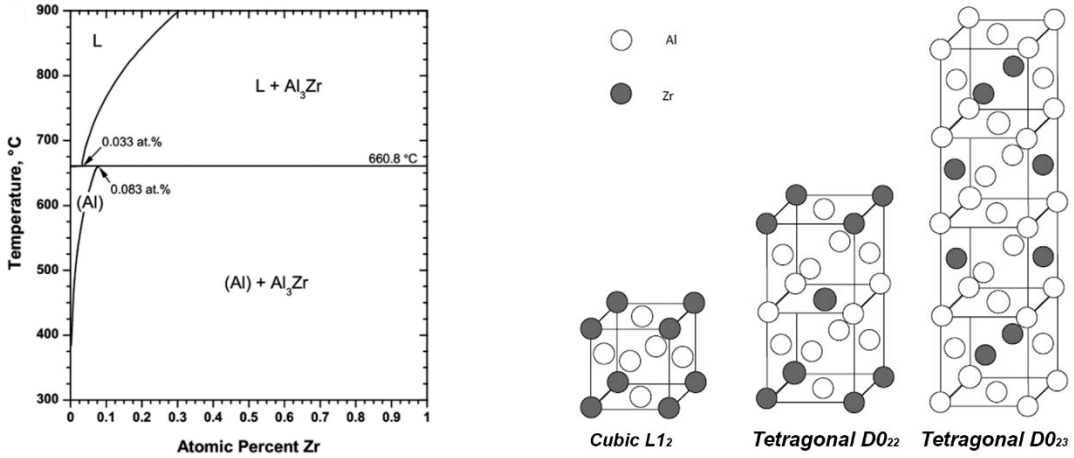

a) b)

Figure 3.6 a) Al-rich side of Al-Zr diagram and b) variety of the crystal structures [130].

There have been intensive investigations of the effect of Zr addition on aluminum wrought alloys. Initially Zr was used as an alloying element for Al-Zn-Mg and Al-Zn-Mg-Cu systems in order to improve recrystallization behaviour, toughness and stress-corrosion resistance [132,133]. In the works of Litynska and Rakhmanov [111,130] it was shown the positive effect of Zr on the mechanical properties in the Al-Mg-Si and Al-Si alloys is due to the formation of coherent Al_3Zr nanoparticles after heat treatment. It was also found that annealing of alloys in a range of 450-540 °C leads to a coarsening of Al_3Zr precipitates from spherical $L1_2$ to an elongated $D0_{22}$ structure. TEM images of the Al_3Zr precipitates found by Litynska *et al* [111] in the Al-Mg-Si wrought alloys are shown in **Figure 3.7**.

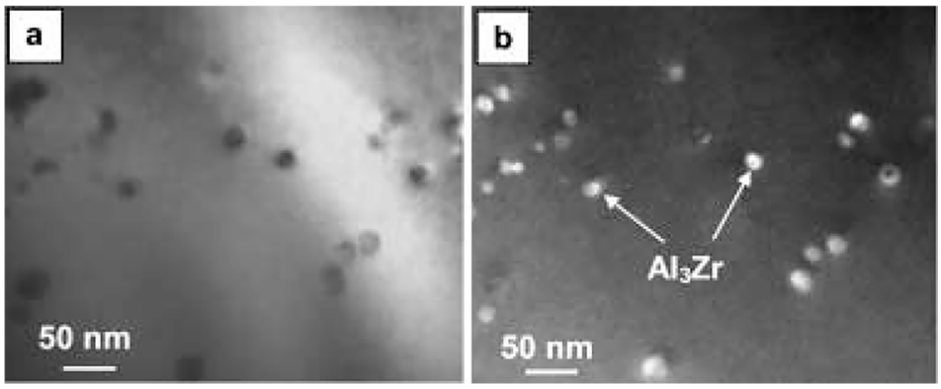

Figure 3.7 TEM images of a) bright and b) dark-field of Al-Mg-Si-Zr wrought alloy after annealing [111]

Scandium and Zirconium

Multicomponent systems are quite difficult to handle, and addition of alloying elements make this task more difficult. Extensive research has been focused on these activities, which will be discussed below. The following review will be divided into the simple analysis of the Al-Sc and Al-Zr phase diagrams and a literature overview of the Sc and Zr addition and its effect on the Al-Mg-Si alloys.

Despite the fact that Sc leads to a significant improvement of mechanical properties, it could not be widely used due to its high price. Even the very low addition of 0.20 wt. % Sc can increase the price per kg of the alloy by 5 US$. The addition of Zr in order to substitute Sc has therefore been pursued extensively. Moreover, such partial substituting leads to effective grain refinement at a lower Sc content and is the most promising combination with Sc to date with respect to recrystallization resistance. This can be attributed to fast precipitation and slow coarsening of the precipitates [17,48].

Effects which can be produced by the single Sc or Zr addition were already briefly discussed. Wrought alloys with the addition of Sc or Zr have excellent mechanical properties due to the formation of Al_3Sc or Al_3Zr nanoparticles (**Figure 3.6** and **Figure 3.7**). These particles are coherent with the α-Al matrix and are effectively dispersed within the grains and grain boundaries, thereby blocking the movement of the dislocations and stabilizing a fine-grained structure [134].

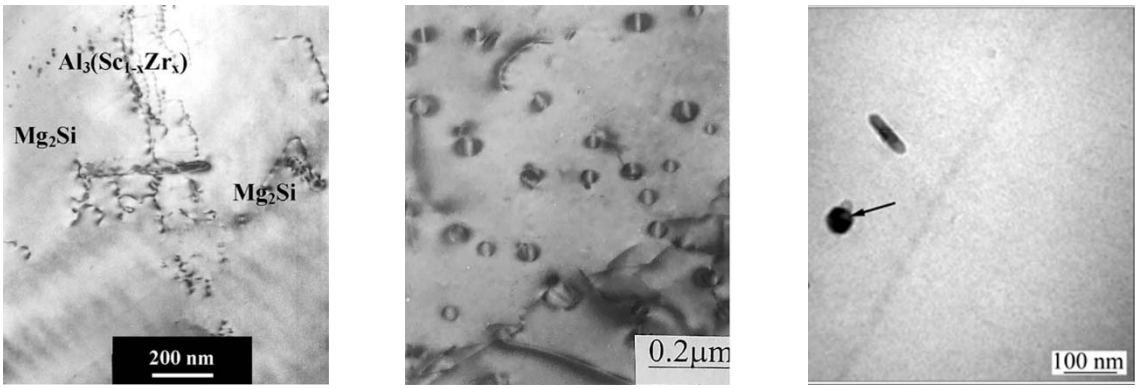

a) b) c)

Figure 3.8 Bright field TEM images of the $Al_3(Sc,Zr)$ nanoparticles, a) [114], b) [135], c) [128]

The combination of Sc and Zr can be more effective in refining as-cast microstructures and moreover, can reduce the amount of Sc by partial substitution of Zr. Due to the high solubility of Zr (up to 50%) in the Al_3Sc phase, $Al_3(Sc_{1-x}\ Zr_x)$ precipitates tend to form [136]. Thus, the joint addition of Sc+Zr leads to the formation of the simple $Al_3(Sc,Zr)$ and complex $Al_3(Sc_{1-x},Zr_x)$ precipitates, which have an $L1_2$ crystal structure (**Figure 3.8**) [111,113,137–139]. Meng *et al* [128] reported that the ratio of Zr to Sc strongly influences grain refinement in the as-cast state. In addition it was mentioned that the morphology of the $Al_3(Sc,Zr)$ can change from coffee bean-like to spherical. Al-Mg cast alloys with the addition of Sc+Zr show a pronounced increase in strength in comparison to alloys with an Sc addition only [135]. In addition, the combination of Sc+Zr improves creep resistance at high temperatures, but results in only a small increase of the microhardness in the as-cast state (mold casting).

3.5 Alloy design

In this subchapter, the proposed alloys, corresponding phase diagrams and heat treatment modes, will be discussed. Based on the above literature overview, solid solution strengthening and precipitation hardening are assumed to be the main strengthening mechanisms in new alloys.

Thermodynamic calculations

Thermodynamic modelling is becoming an important tool in alloy development, helping to determine phase formation under equilibrium condition and enabling the prediction of formation of new phases in alloys. The Thermo-Calc approach was used to calculate binary phase diagrams (**Figure 3.2, Figure 3.9 and Figure 3.10**) and to assess the effect of the alloying elements for the temperature range 500-700°C, based on the literature discussed above. The proposed alloys are marked with lines, which illustrate where a new phase appears or disappears. All studied alloys in the cast state have new phases in comparison with the base composition. Zr addition leads to the formation of Al_3Zr, Cr to $Al_{45}Cr_7$ and Sc to Al_3Sc primary phases. The existing phases along with the reaction sequence are listed in Appendix A.3

Alloys with Zr and Cr+Zr additions

Figure 3.9 presents the calculated phase diagrams for Sc-free alloys, containing the addition of Zr and the combination Cr+Zr. Zr has the lowest peritectic concentration among all the alloying elements (0.07 wt. %). Alloys with Zr (Z1 with 0.1 wt. % Zr and Z2 with 0.2 wt. % Zr) addition have only one new phase - Al_3Zr phase (**Figure 3.9a**) as compared to the base alloy. Even a high temperature solution treatment of alloys with Zr (Z1 and Z2 alloys) doesn't dissolve the new Al_3Zr phase in α-Al matrix. Alloys with the combination of Cr+Zr have, in addition to the Al_3Zr phase, $Al_{45}Cr_7$, which is more frequently referenced as Al_7Cr [44,140] (**Figure 3.9b**), and which forms earlier then $Al_{15}(Mn,Fe)_3Si_2$ phase. Addition of Cr to Zr-containing alloys (CZ11, CZ22, and CZ33 see also **Table 3.6**) increases the temperature formation of $Al_{15}(Mn,Fe)_3Si_2$ phase and at the same time reduces the formation temperature of α-Al.

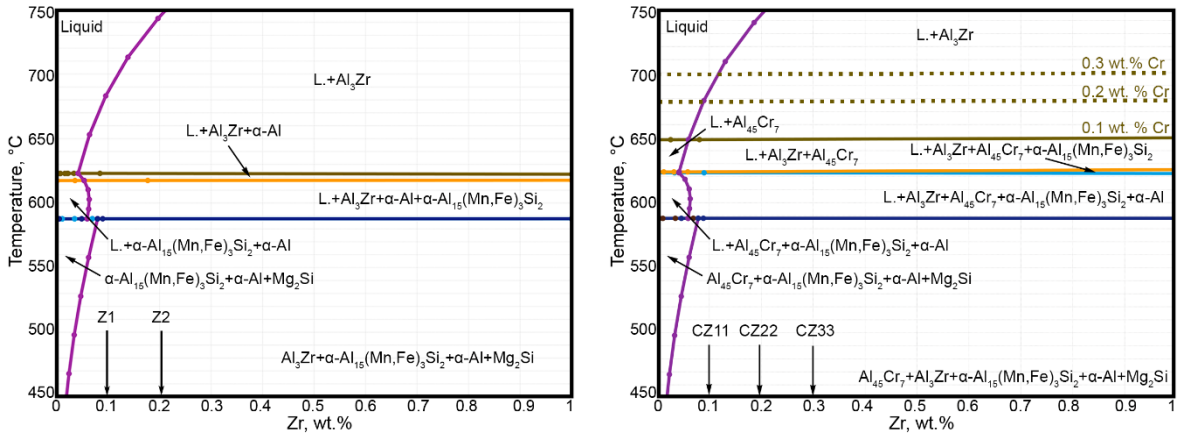

a) b)

Figure 3.9 Calculated phase diagrams of the investigated alloys, AlMg5Si2Mn with additions of a)Zr, b) Cr and Zr

Alloys with Sc and Sc+Zr additions

Figure 3.10 shows the calculated phase diagrams for Sc-containing alloys for the temperature ranges of 450-750°C. The peritectic concentration in Sc-containing alloys amounts to 0.12 wt. % and takes place at 591 °C (**Figure 3.10a**). As it was mentioned in **Table 2.2**, Sc and Zr have low solubility. The solubility of Sc sharply decreases during solidification, resulting in a drop to 0.03 at 450°C and to near zero at room temperature. The Al_3Sc intermetallic phase is present in both alloys with 0.1 and 0.2 wt. % Sc. However, in the alloy S1 (0.1 wt. % Sc), the Al_3Sc phase is dissolved during the solution treatment at temperature of 560°C and above. For the S2 (0.2 wt. % Sc) alloys, HT at the allowable temperature ranges does not lead to dissolving of the Al_3Sc phase.

Alloys with the combination of Sc+Zr (see **Table 3.6**) have two additional phases as compared to the base alloy, Al_3Sc and Al_3Zr (**Figure 3.10b**). The phase diagram is rather similar to the Al-5Mg-2Si-0.6Mn-(0…1.0)Sc phase diagram.

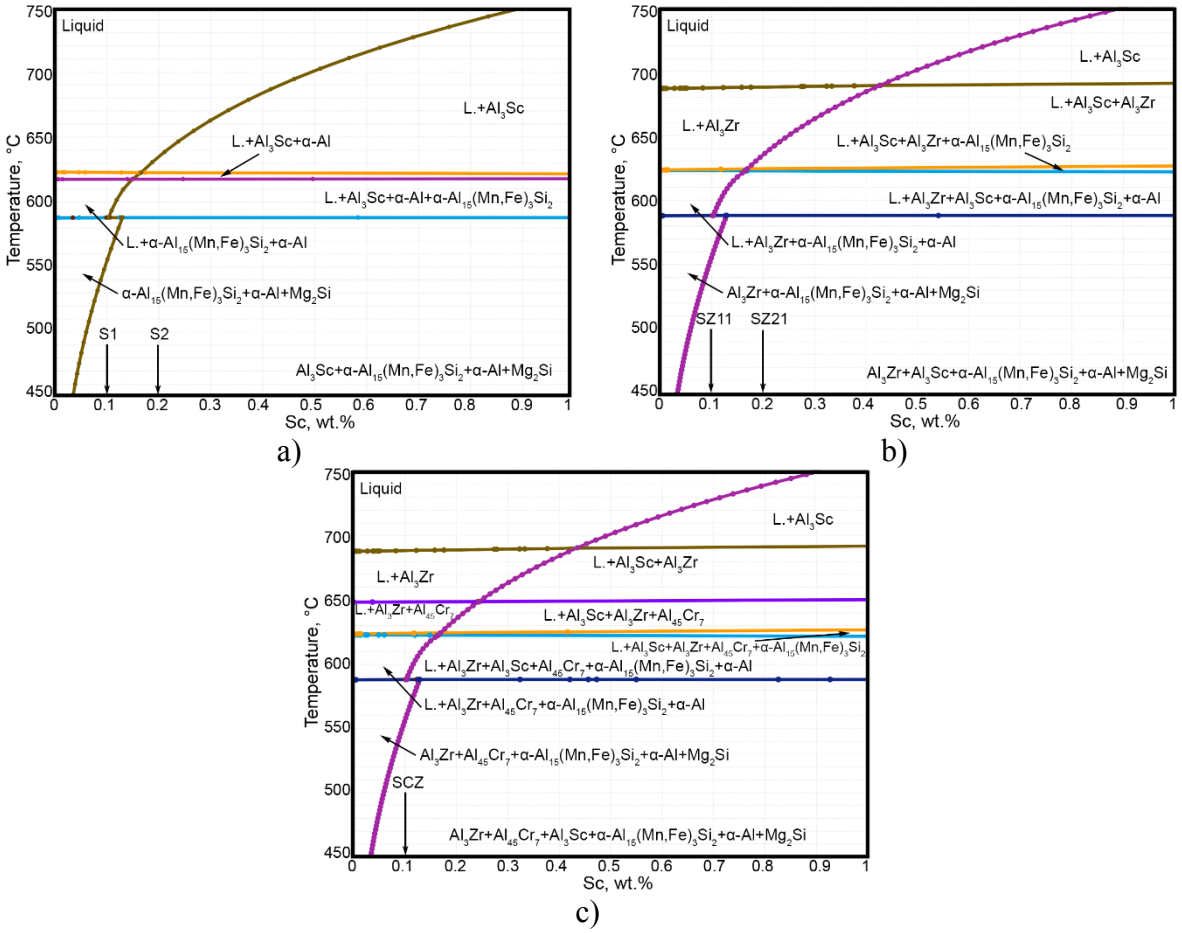

Figure 3.10 Phase diagrams of the investigated alloys, AlMg5Si2Mn with additions of a) Sc, b) Sc and Zr, c)Sc, Cr and Zr.

3.6 Proposed compositions and heat treatment of new alloys

Based on the study of the phase diagrams and literature overview which have been presented above, it seems possible to develop new Al-Mg-Si based alloys with improved mechanical properties by combined additions of Sc and Zr.

In order to reach this goal, the correct amount of the alloying elements must be used and knowledge of the solubility of the chosen elements in the aluminum is needed. Solubility data of the main alloying elements in the aluminum are summarized in **Table 3.5.**

Table 3.5 Solubility data of binary aluminum alloys

Element	Mg	Si	Mn	Fe	Sc	Zr
C_{max}, wt. %	17.4	1.65	1.82	0.052	0.38	0.28
T, °C	450	580	660	655	659	663

The novelty of this research is that only a few investigations on the addition of Sc and Zr on Al-Si-Mg and Al-Mg cast alloys have been undertaken to date [15,16,141–143] and no research has been performed on the Al-Mg-Si system. Furthermore, close inspection of previous experimental results reveals that the primary research focus was on wrought alloys [13]. The automotive industry, however, requires new cast aluminum alloys with improved yield strength and at least comparable elongation to existing commercial alloys. **Table 3.6** presents the chemical composition for the alloys used in this research.

Table 3.6 Summary of the main alloying elements of the developed alloys, Al-balanced

Alloy	Chemical composition in wt. %					
	Mg	Si	Mn	Cr	Zr	Sc
Z1	5	2	0.5	-	0.1	-
Z2	5	2	0.5	-	0.2	-
CZ11	5	2	0.5	0.1	0.1	-
CZ12	5	2	0.5	0.1	0.2	-
CZ22	5	2	0.5	0.2	0.2	-
CZ33	5	2	0.5	0.3	0.3	-
S1	5	2	0.5	-	-	0.1
S2	5	2	0.5	-	-	0.2
SZ11	5	2	0.5	-	0.1	0.1
SZ21	5	2	0.5	-	0.1	0.2
M59	5	2	0.6	-	0.03%Fe	-

Heat treatment

Al-Mg-Si alloys have one of the highest solidus temperatures among all Al alloys and can be heat treated at temperatures up to 575ºC [144–146]. **Table 3.7** represents the proposed temperatures for the solution treatment artificial aging of the binary Al-X systems in comparison to the base alloy (M59) according to the literature data [13,147–150] and the solubility of the Sc and Zr in the Al-5Mg-2Si-0.6Mn-X systems based on calculated diagrams (**Figure 3.9-3.8**). It can be seen that the difference in solubility between 520 ºC and 540ºC is negligible. The new phases can be dissolved at around 0.07 wt. % Sc and 0.04 wt. % Zr.

Table 3.7 The solubility of Sc and Zr for Al-Mg-Si system along with the used HT modes according to the literature overview.

	Temper		Solubility of the alloying element in Al-Mg-Si system [wt. %]					
System	ST	AA	591ºC	540ºC	520ºC	500ºC	480ºC	460ºC
Al-Sc	500-600	250-350	0.07	0.05	0.04	0.03	0.02	0.01
Al-Zr		-	0.12	0.09	0.07	0.05	0.03	0.02
Al-Mg-Si	480-575	170-250						

According to Röyset [13], Sc in supersaturated solutions may precipitate as finely dispersed Al_3Sc particles in the temperature range 250°C – 350°C (**Table 3.7** and **Figure 3.11a**), whereas for the Al-Mg-Si alloys the commonly used temperature for industrial purposes is in the range of 560-580°C (T6 regime) [151] (**Table 3.7** and **Figure 3.11a** and **b**). It seems that the combination of precipitation hardening of Al_3Sc with precipitation hardening Mg_2Si is not straightforward. Formation of one of these precipitates can exclude the formation of the other. Nevertheless, it was thought to be possible to combine two mechanisms: precipitation hardening and solid solution strengthening; or alternatively to find the optimal heat treatment for the investigated alloys.

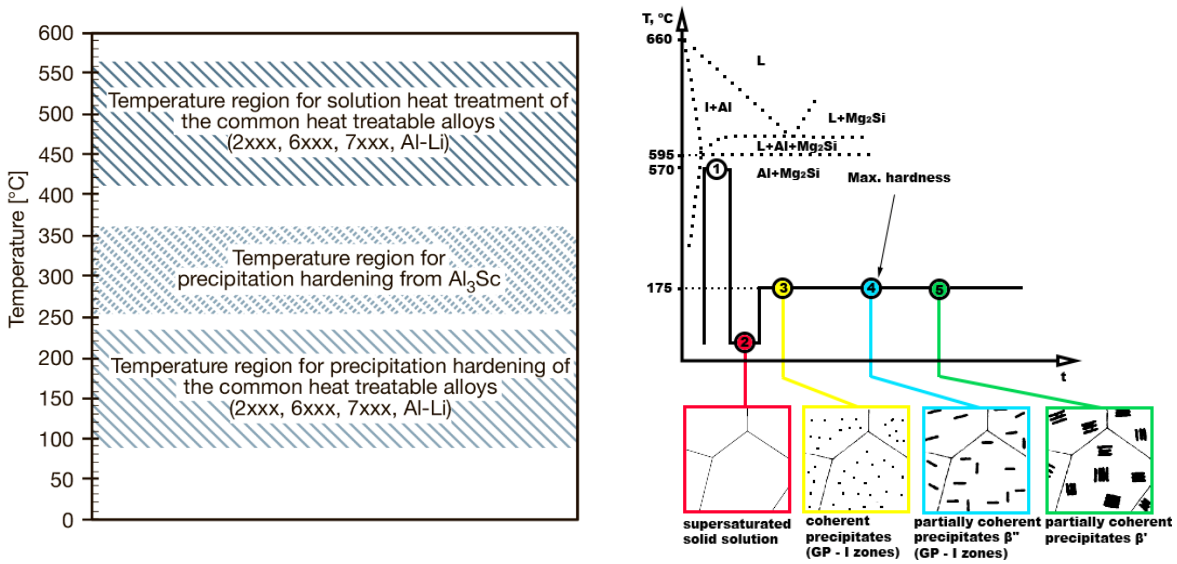

a) b)

Figure 3.11 a) Typical temperature regions for solution heat treatment and precipitation hardening [13] and b) Precipitation sequence of the investigated alloys, adapted from [50]

Chapter 4

Materials and Experimental Methods

This chapter presents the experimental techniques used and procedures followed in this investigation. The present work has been concentrated on the Al-Mg-Si alloys with addition of Zr, Cr, and Sc with the focus on precipitates formed in the matrix prior to heat treatment and changes of mechanical properties from the as-cast state to age hardening. During this investigation the following methods have been used: optical microscopy, scanning electron microscopy (SEM) in combination with Energy Dispersive Spectrometry (EDS) and transmission electron microscopy (TEM).

4.1 High Pressure Die Casting (HPDC)

The specimens were cast at the Friedrich-Alexander-Universität Erlangen-Nürnberg (FAU), Erlangen Germany. The composition of the investigated alloys is shown in Table 3.6. The commercial Magsimal59® produced by "Rheinfelden Alloys GmbH" (Rheinfelden, Germany) was used as a starting alloy. Blocks of the Magsimal59® were stored in the preheated furnace at 250°C for 24 hours in order to avoid moisture before being transferred into the melt with a temperature of 720°C. For achieving the aimed compositions, commercial AlCr20, AlZr15 and AlSc2 master alloys were successively added into the melt. For degassing the melt was impelled and the density index controlled by a vacuum density tester in combination with the density index balance (MK 3VT and MK3000). The chemical composition was controlled by spark emission spectroscopy (Ametek Spectromaxx). The plate specimens (Figure 4.1 a) with dimensions of 300x150x4 mm were cast using a cold chamber HPDC unit (Frech DAK 450-54 with 4500 kN mold clamping force) at the following parameters: melt temperature T_m=720°C, mold temperature T_d=200°C, piston speed υ=2m/s, final (post) pressure p=250 bar.

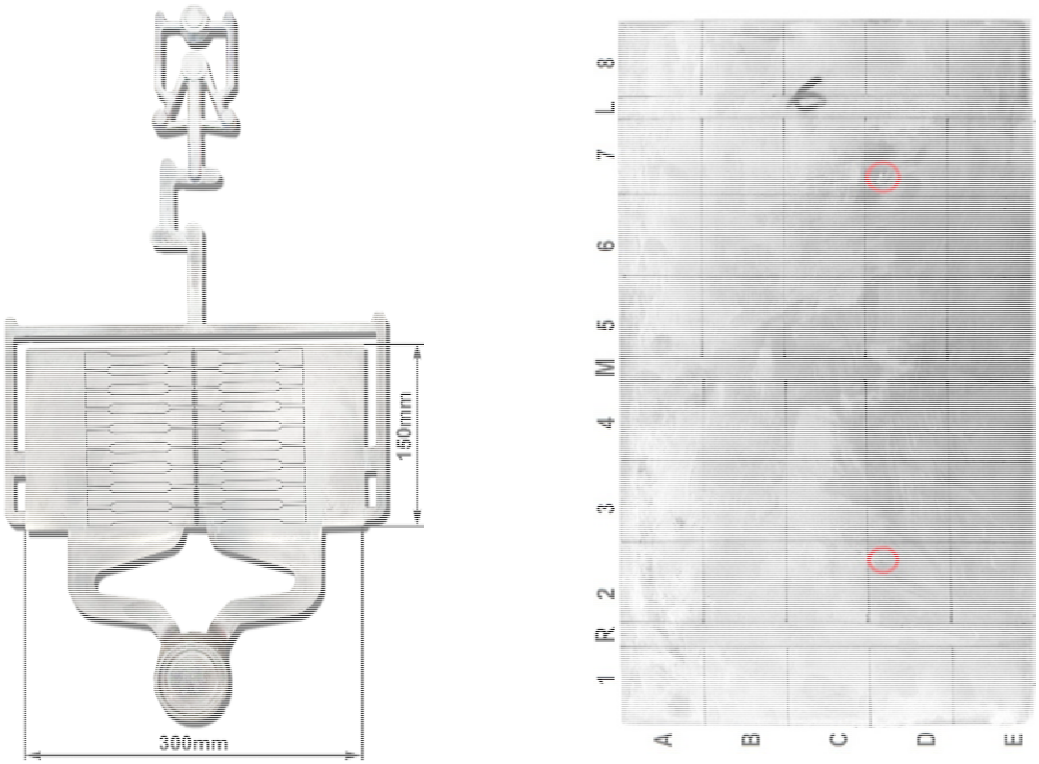

a) b)

Figure 4.1 a) As-caste plate with gating system and overflow directly after withdrawing from the HPDC machine and b) after removal of the casting system.

The base alloy alloy, M59 was chosen for the examination of the casting quality. The plate was divided into several areas (Figure 4.1b) and hardness measurements were taken across it. The results show that hardness in the side areas is higher, than in the central section. Also in three areas (named R, M and L) lower hardness values compared to those in the other areas were observed. In some plates visual defects such as bubbles were detected. The gas quantity inside high-pressure die castings varies with the part complexity, die spray, venting efficiency, and other factors. The existence of a degree of porosity in die-cast components is normally accepted. The casting defects were analysed by FAU. All plates were examined using X-ray tomography and the M59 base alloy was chosen to determine the porosity.

4.2 Differential scanning calorimetry

Differential scanning calorimetry (DSC) was performed with the assistance of P. Randelzhofer the Friedrich-Alexander-Universität Erlangen-Nürnberg (FAU), Erlangen Germany.

The measurements were performed using a NETZSCH device (heat flux type DSC) using disc-shaped specimens with a weight of 20 mg. During DSC studies the chamber was protected by purified argon gas (99.99% purity) with 10-20 cm^3/min flow rate. Temperature scans were made in the range from room temperature ~ 25 to 710°C with computer controlled heating and cooling.

Before the measurement, the DSC was calibrated using the standard calibration program and tools supplied by NETZSCH. In order to check the reliability of the melting onset temperature, aluminum specimens of different purities were heated and cooled down at a rate of 5 K min^{-1}.

4.3 Heat treatment

Two types of heat treatment were applied: T6, which combines solution treatment (ST) at the temperature ranges between 480 and 570°C, water quenching and artificial aging (AA) at the temperature ranges between 175°C-325°C for various times. The second type was T5, AA at 125°C, 175°C, 220°C and 325°C from the as-cast state for various times.

In order to ensure an equal heating rate and temperature distribution, the specimens were positioned in the central part of the preheated furnace. To control temperature, a K-type thermocouple was placed directly at the surface of the specimens.

4.4 Specimen preparation

Microstructural examinations and characterization of the mechanical properties of all the investigated materials were carried out. During the metallographic preparation the samples were ground. The sequence of papers used was: 220, 500, 800, 1200, 2500, 4000 SiC-grit. The next step was polishing with different diamond suspensions up to a minimum of 1 μm particle size. After each polishing step, the specimens were ultrasonically cleaned with alcohol for 3

min and then dried. The finishing process was vibration polishing using non-crystallized colloidal silica (0.04 μm). The details for the grinding and polishing steps are summarized in Table 4.1.

For the scanning electron microscopic microstructure analysis (SEM), the samples were applied directly to the aluminum holder (without embedding agent between the holder and the sample). For the nanoindentation measurements the samples were bonded to the aluminum holders using Cyanoacrylate "superglue".

Thin foil preparation for transmission electron microscopy (TEM) studies was carried out in a twin jet STRUERS Tenupol 3 electropolishing machine. Disks with diameter 3 mm and a thickness less than 100 μm were electropolished using an electrolyte with 25% of nitric acid and 75% methanol, kept at -25 °C and a voltage of 5 V.

Table 4.1 Details of grinding and polishing steps

	Type	Lubricant	Time, in min
Grit SiC Paper	220	water	3
	500		1
	800		1
	1200		1
	2500		1
	4000		2
Polishing pad	NAP	DP 3 μm	5
	NAP	DP 1 μm	5
Vibropol	NAP	Silica+water	30

4.4.1 Light and scanning electron microscopy

Microstructural parameters such as the phase average size, its distribution and volume fraction, the dendritic arm spacing (DAS) and the interlamellar space (ILS) of the eutectic were investigated and measured using ImageJ software. In order to obtain a statistical average of the distribution, a series of at least 15 micrographs for each specimen were taken. For the

calculation of the average grain size at least 70 individual grains were measured. The length of the Al_3Zr phase was calculated for the largest diameter. Owing to the presence of a difference in ILS between the middle and close to edge parts and the orientation of the lamellas and the way it was cut, the mean ILS value was measured for the mid-central region of the plate only.

The microstructural analysis was carried out using a TESCAN Mira3 SEM operating at 15kV and equipped with an EDS (Energy Dispersive Spectrometry) detector. The electron probe microanalysis (EPMA) was performed using the JEOL JXA-8100 operating at a voltage of 15 keV with a spot size of 10 μm, a step size of 0.25 μm and a dwell time of 500 ms.

4.4.2 Transmission electron microscopy

A Philips CM20 microscope was used to perform the TEM investigations with the measurements being carried out 200 kV accelerating voltage. Bright-field (BF) images were used for observing the morphology of solid solution grains, intermetallics and precipitates.

4.5 Hardness measurements

The hardness of each sample was measured by a Brinell tester under a load of 306.56 N (31.25kp) with a ball diameter of 2.5 mm for 10 sec. For each composition 10 tests were performed and the average value has been calculated.

Vickers hardness measurements were performed using a Zwick Roell Hardness Testing Machine. The loads used were 0.1 and 0.05 kgf with a dwell time 10 seconds. For each alloy at least 10 measurements were done.

Microhardness is determined from the relation of applied load to the contact area of the indentation by measuring the diagonals d_1 and d_2 of the indentation (Figure 4.2 a). The following equation is used in order to obtain hardness of the specimen:

$$H_v = \frac{2F \sin\frac{\alpha}{2}}{d^2} \tag{4.5.1}$$

where F is the load (kgf), α=136° is the angle between two facets of the Vicker's pyramid and d is the average value of d_1 and d_2 (mm).

In Figure 4.2 b the microhardness imprint HV0.05 in the α-Al matrix is shown.

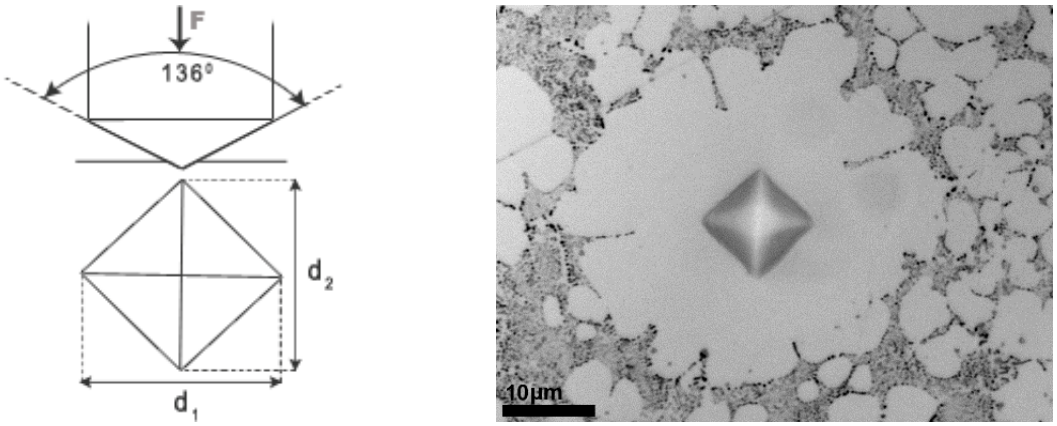

a) b)

Figure 4.2 a) Schematic illustration of the indentation imprint and its diagonals measurement and b) Image of a microhardness imprint on a polished surface

4.6 Nanoindentation measurements

Instrumented indentation testing or nanoindentation is used to determine the nanohardness and Young's modulus of materials at small length scales. During nanoindentation, the load and displacement are continuously measured, as the material is indented using an indenter of known geometry. A typical load displacement response is schematically illustrated in Figure 4.3.

The nanoindentation measurements were performed on two separate instrumented nanoindenters, iNano (Nanomechanics inc., USA) and G200 (Keysight Technologies, USA) using the diamond indenter Berkovich tip. Both nanoindenters are equipped with load controlled (LC) and continuous stiffness measurement (CSM) units. For each hardness measurement 10 indents were performed with a maximum load of 25 mN. Average hardness values were calculated in a range of 700 nm to the maximum indentation depth of 900 nm in order to avoid surface roughness and indentation size effects.

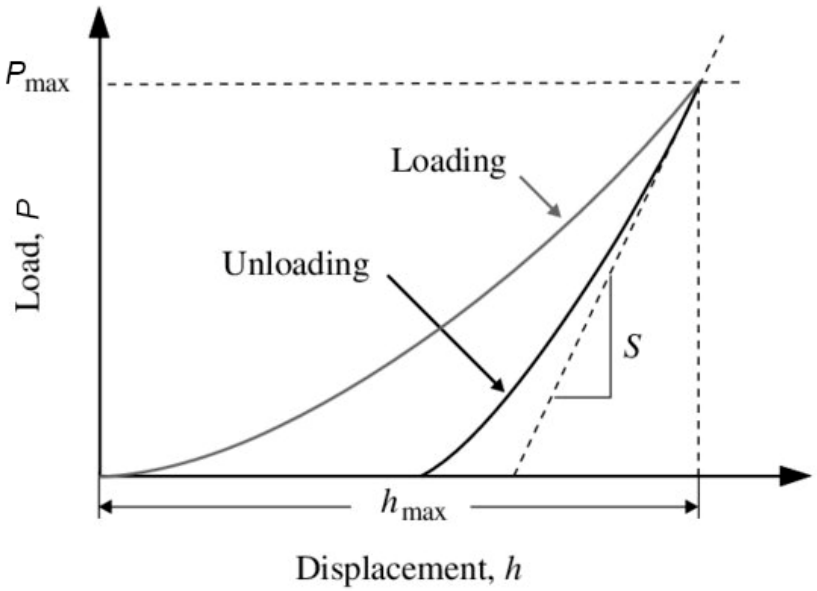

Figure 4.3 Schematic illustration of a load displacement curve

Amorphous silica mounted on an aluminum base was used for calibrating the area function of the tip. Load and penetration depth were measured for all indentation tests and hardness values were obtained using the Oliver-Pharr method (4.6.1) [152]. The hardness can be calculated using the maximum force P_{max} and the relevant contact area, A_c:

$$H = \frac{P}{A_c} \tag{4.6.1}$$

4.7 Tensile Tests

Standard, room temperature uni-axial tensile tests using flat rectangular specimens (**Figure 4.4**) were performed on an Instron 5967 testing machine at a cross head speed of 1 mm/min, giving an initial strain rate of 8.3×10^{-4} 1/s The dog-bone shaped specimens with a rectangular cross-section were prepared in accordance with ASTM E8_E8M_13a (**Figure 4.4**). The specimens were taken from the central areas of the plates (areas 2-4 and 5-7 in **Figure 4.1b**). The Instron machine is equipped with an extensometer that provides the local strain values for each sample. For each composition 10 tensile tests were performed and the average values of the yield strength, ultimate tensile stress and elongation to failure in both as-cast state and after heat treatment have been calculated.

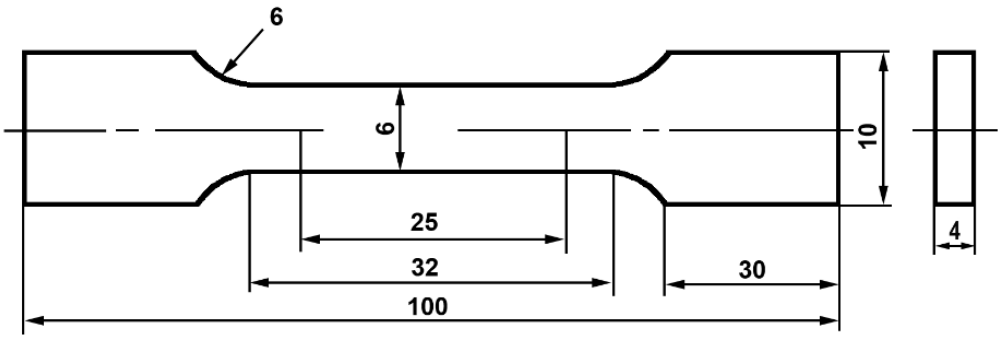

Figure 4.4 Schematic illustration of the tensile test samples

Chapter 5

As-cast state of Al-Mg-Si alloys with alloying elements

The microstructural characterization of the alloys has a fundamental importance for the understanding and correlation to the mechanical properties. The main interest in this chapter will be focused on: differential scanning calorimetry study, phase identification and determination of their morphology together with EDX analysis of the existing phases after additional alloying.

5.1 Differential scanning calorimetry (DSC)

Figure 5.1 shows the DSC curve for the commercial AlMg5Si2Mn HPDC alloy, which is used as a base material. The melting behaviour can be seen from the upper part of the curve, i.e. an endotherm. Upon cooling down the crystallization of the α-Al and secondary phases yields and shows exotherm (lower curve of the DSC plot). Two cycles of heating and cooling were performed in order to verify the effect of the aging on the melting behaviour. Only one sharp endothermic peak was detected, which can be characterized by three specific temperatures:

- melting onset temperature T_{onset} - 591,9°C;
- peak temperature T_{peak} - 610,8°C;
- melting outset temperature T_{offset} - 630°C.

The melting onset temperature of 591.9°C is close to those which can be found in the literature (594 °C) and according to the **Table 3.1**, corresponds to the first endothermic reaction (Al) + Mg_2Si → L, melting of the (Al)+(Mg_2Si) eutectic. The second endothermic peak appears with the following heating and related to the melting of α-Al matrix. The end of melting is specified by melting offset temperature. For the base alloy it was found to be 630°C.

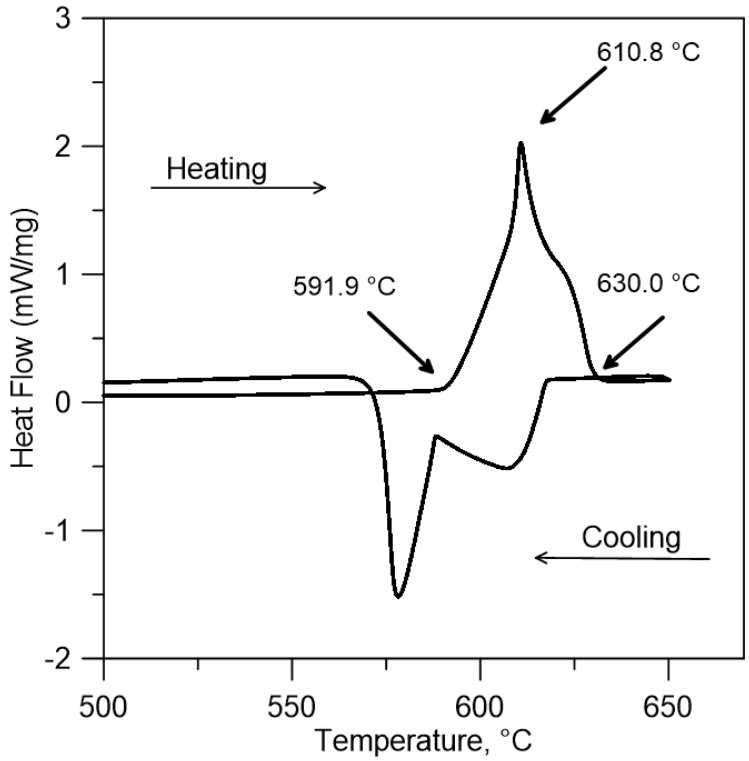

Figure 5.1 DSC curve of the base alloy in as-cast state.

Calorimetric study of the Sc-free alloys

Figure 5.2 (a) and **Table 5.1** give an overview of the melting and cooling behaviour of the investigated Sc-free alloys. Alloys with additions of Zr up to 0.2 wt. % and Cr with Zr up to 0.3 wt. % of each will be discussed here. The position and shapes of the DSC curves, obtained from Zr and Cr+Zr containing alloys, are similar to the base alloy, thereby indicating that alloying of Al-Mg-Si alloys with Zr and Cr+Zr does not affect the phase equilibrium. However, a difference of ±2°C in the melting temperatures in comparison to the base M59 alloy was detected.

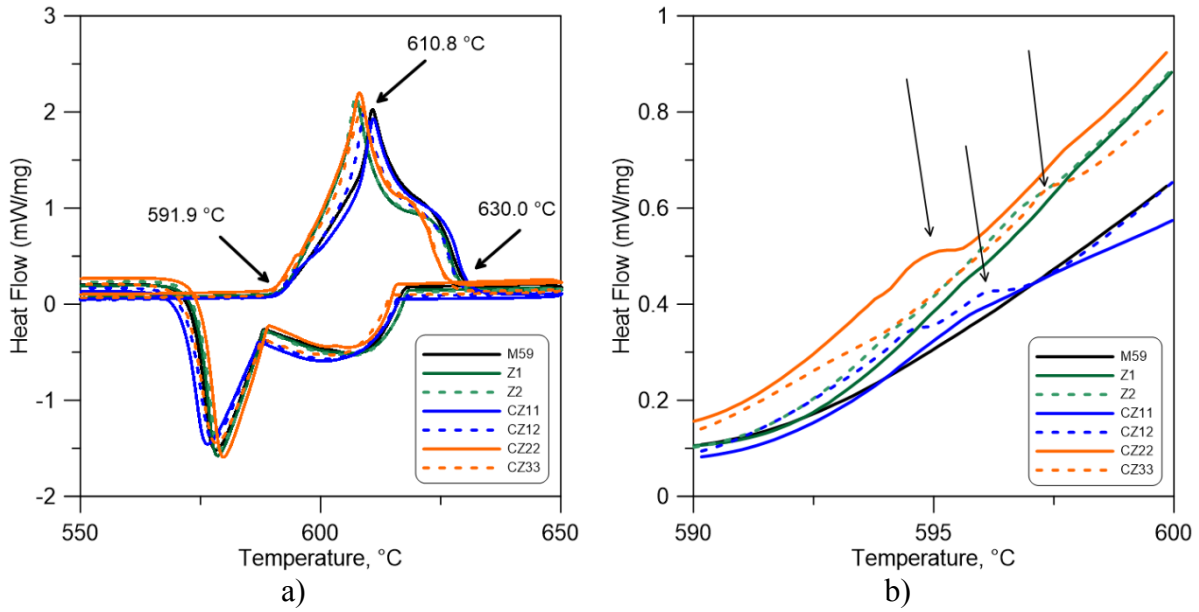

Figure 5.2 a) DSC heating and cooling curves of the Sc free alloys, b) enlarged DSC traces for these alloys in a range of 590-600°C.

Figure 5.2 (b) shows enlarged DSC traces for the Sc-free alloys. In the temperature range 590-600°C small peaks (marked by arrows) were observed, which can be related to the melting of the (Cr, Zr)-containing phases and this will be discussed later. Therefore, it can be concluded that two main reactions take place. (Al) + Mg_2Si → L reaction at ~592°C and (Al) → L at ~630°C. Addition of Cr and Zr does not change the solidification range.

Table 5.1 Measured temperatures of the Sc-free alloys, at heated rate of 5 K/min, in °C

Alloy	T_{onset}	T_{peak}	T_{offset}
Z1	592.1	607.5	628.9
Z2	591.5	607.4	628.6
CZ11	591.7	610.9	630.6
CZ12	591.0	609.3	629.0
CZ22	590.8	608.0	625.7
CZ33	589.3	608.6	626.3

Calorimetric study of the Sc-containing alloys

The second set of the alloying elements contains Sc and Zr. The investigated alloys comprise alloys with the addition of Sc only in the amount of 0.1 and 0.2 wt. % and alloys with a combination of Sc and Zr as well as a mixture of Sc, Zr, and Cr. The high temperature parts of the DSC heating curves of Sc-containing alloys with a heating rate of 5 K/min are shown in **Figure 5.3**. The DSC traces for the Sc- containing alloys are quite similar to each other and in comparison to the base and Sc-free alloys.

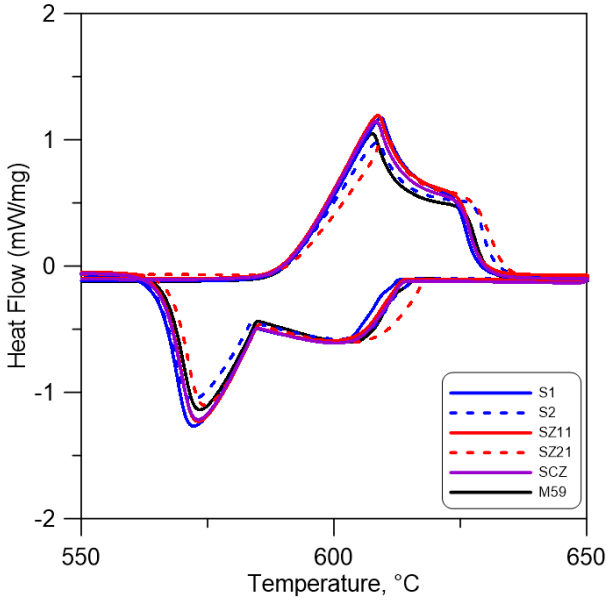

Figure 5.3 DSC heating and cooling curves of the Sc containing alloys

The different melting temperatures are shown in **Table 5.2**. Onset, peak, and offset temperatures were very close to those obtained for Sc-free alloys, thus confirming that addition of Sc+Zr and Sc+Zr+Cr has no effect on the eutectic melting temperature and melting of the α- Al solid solution. In the alloys with a high concentration of the alloying elements new phases have been observed during microstructural investigation (**Figure 3.9**). Nevertheless, due to the low volume fraction of these intermetallic phases, only small implicit peaks were observed in the DSC curves. In the alloys with the 0.2 wt. % Sc, a minor increase in the solidification range was detected.

Table 5.2 Measured temperatures of the Sc-free alloys, at heated rate of 5 K/min, in °C

Alloy	T_{onset}	T_{peak}	T_{offset}
S1	588.2	611.3	629.9
S2	588.4	611.1	633.2
SZ11	590.0	610.9	630.7
SZ21	590.3	610.0	634.2
SCZ	589.4	610.8	630.6

5.2 Microstructure study of Al-Mg-Si alloys

A typical cross-section of a plate is shown in **Figure 5.4**. The volume fraction of eutectic close to the edge region (marked with arrows on the upper image) is higher in comparison to the middle section of the plate. Thus, all measurements have been performed on the middle section. The difference in volume fraction of eutectic and α-Al will be discussed in the Chapter 5.3.

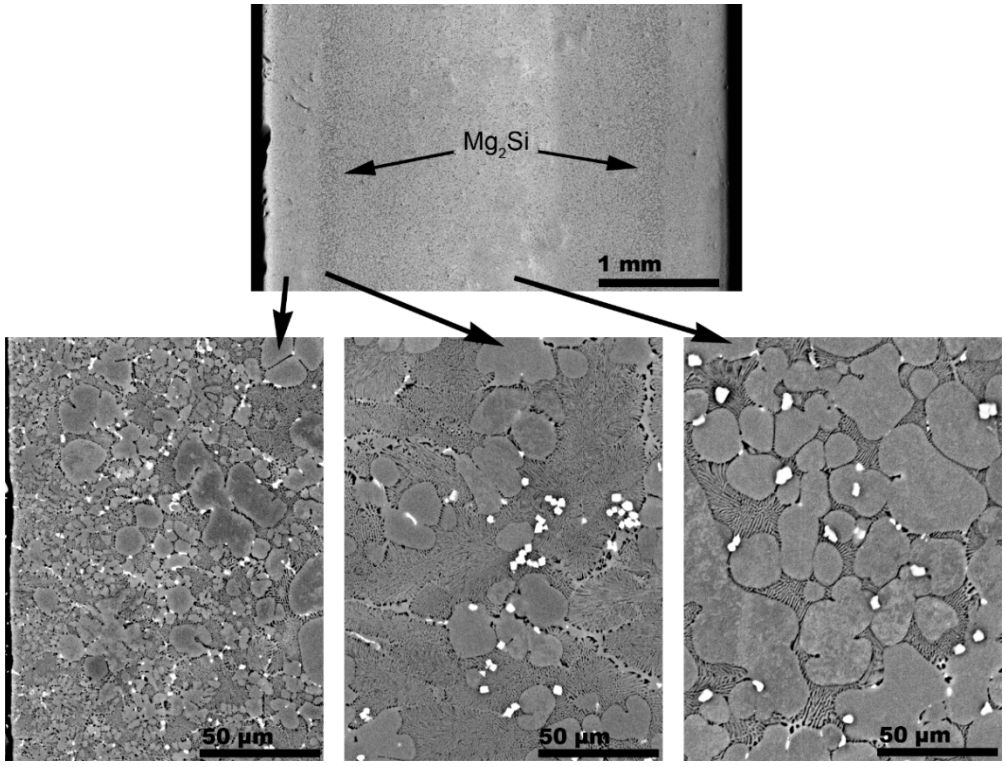

Figure 5.4 Cross section of the plate with the corresponding microstructures.

Figure 5.5 represents an overview of the base alloy (M59) and the chemical composition is listed in **Table 3.6**. The structures of the base alloy are composed of α-Al solid solution, Al+Mg_2Si eutectic, α-$Al_{15}(Mn,Fe)_3Si_2$ phase. The Al+Mg_2Si eutectic has a lamellar and/or fibers morphology, where long Mg_2Si plates and fibers alternate with α-Al.

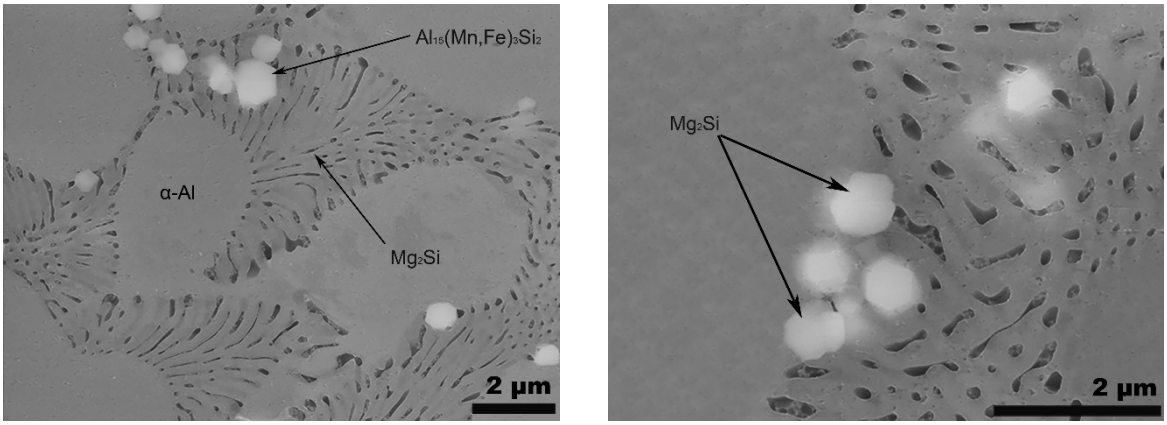

a) b)

Figure 5.5 SEM image of a base alloy: a) an overview of a microstructure, b) Mn- containing intermetallic phase.

The composition of the Mn-phases and α-Al solid solution was measured by EDS analysis using SEM. The chemical compositions of α-Al solid solution and Al(Mn,Fe)Si phase are presented in **Table 5.3**. Despite the different morphologies of Mn-containing phase (hexagonal or cubic), these particles have the same composition and belong to the α- AlMnFeSi phase. The α-AlMnFeSi phases are mostly located in the interdendritic region and inside eutectic colonies (**Figure 5.5**). More rarely they can be found apart in the α-Al (**Figure 5.7**). This phase can be identified as α-$Al_{15}(Mn,Fe)_3Si_2$ [153–155].

An identification of the composition of the Al+Mg2Si eutectic is rather difficult, due to the small size of the lamellas compared to the relatively huge EDX spot of a few micrometers, which can engage surrounding elements to the spectrum.

Table 5.3 Average composition of the α-Al solid solution and Mn-containing phase in base alloy

Element	α-Al dendrites, in wt. %	Mn-phase, in wt. %
Mg	2.86	5.05
Al	96.13	72.49
Si	0.44	6.6
Mn	0.38	12.86
Fe	0.05	2.78
Ti	0.13	0.2

From the literature, it is known that the α-Al contains around 2.7 wt. % of Mg and around 0.2 wt. % Si at the eutectic temperature (~594°C) [88]. These values are close to those obtained from our analysis at RT. Nevertheless, a small deviation can be caused, due to the fact that the chemical composition of the base alloy refers to a hypereutectic alloy and the solidification runs under non-equilibrium conditions. It should be mentioned, that measurements were performed in the centre of each grain. In the regions close to the Al+Mg_2Si eutectic an increase in the Si and Mg content was observed, due to the low (<1) partition coefficient of Mg and Si in Al [46].

The segregation of the main alloying elements for the base alloy was studied using EPMA measurements. SEM images with the corresponding maps are given in **Figure 5.6**. Due to the different partition coefficients elements segregate differently. The partition coefficients are defined as the slope of the liquidus over the slope of the solidus lines in a binary phase diagram of the particular elements in aluminum [42]. Where k is close to 1, the element has a little tendency for segregation in the Al. Thus, Mg as well as Si, which has a segregation coefficient in Al less than 1 (~0.5 and ~0.1 respectively) [42,46], enrich the dendritic edge and mainly accumulate in the eutectic regions. Mn is homogeneously distributed across α-Al and mainly accumulated in the regions of α-$Al_{15}(Mn,Fe)_3Si_2$ phases.

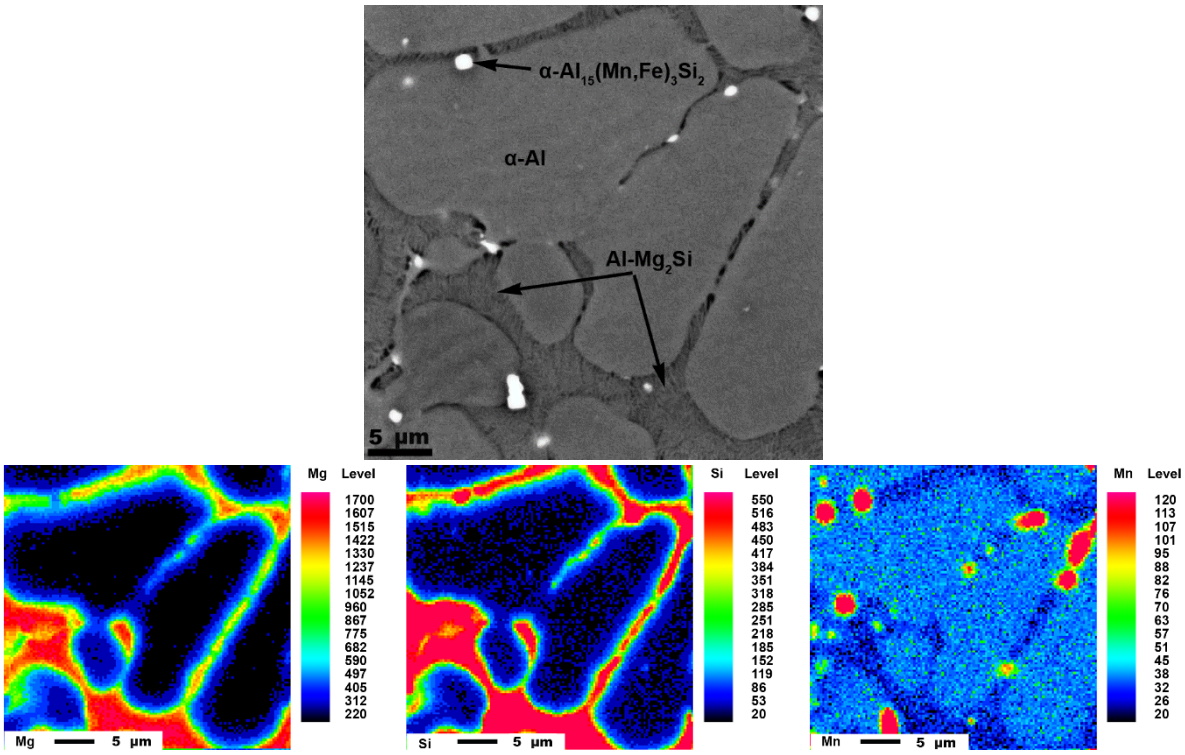

Figure 5.6 SEM image of the base alloy and EMPA maps of the dendritic area

5.2.1 Effect of Zr and (Zr+Cr) addition

Figure 5.7 shows the microstructure of the alloys containing Cr and Zr additions. The structure of the new alloys mainly consists of the same phases as the base one (α-Al grains, Al+Mg_2Si eutectic and α-$Al_{15}(Mn,Fe)_3Si_2$ phase). A new Al_3Zr phase was found (**Figure 5.14**), however, in the alloys with the addition of Zr of 0.2 wt. %. The presence of this phase was also predicted by the thermodynamic calculations (**Figure 3.9**). **Table 5.4** shows an average chemical composition for the α-Al solid solution. The main alloying elements (Mg, Si, Mn), present in the solid solution, remain at the same level as in the base alloy. The average content of the additional elements (Zr and Cr) is close to the amount of Zr and Cr in α-Al matrix, added to the base alloy. And that was also confirmed directly after casting by OES.

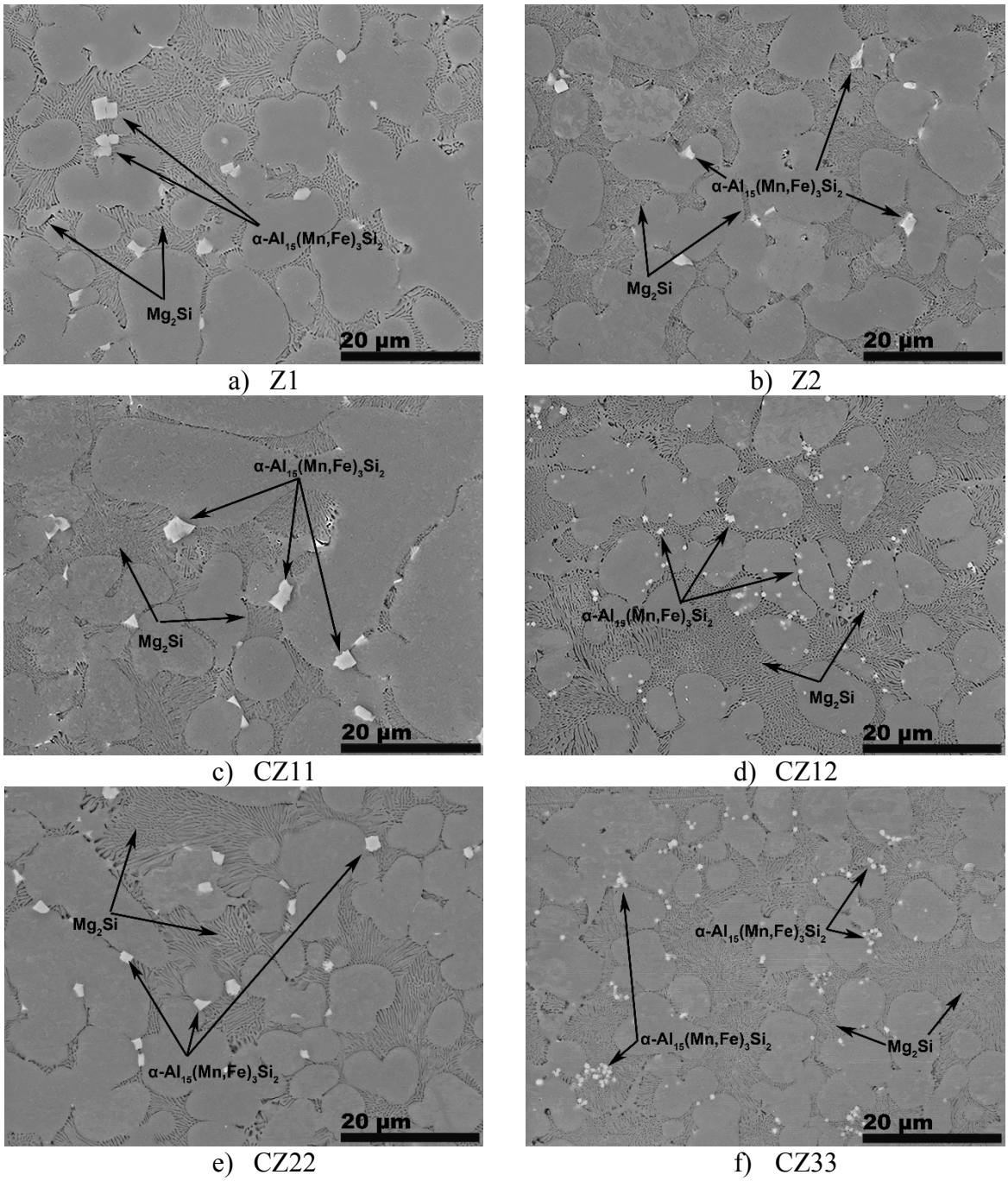

Figure 5.7 SEM micrographs of the Sc free alloys

Table 5.4 Average composition of the α-Al solid solution

Element, wt. %	Alloy						
	M59	Z1	Z2	CZ11	CZ12	CZ22	CZ33
Mg	2.86	2.89	2.63	2.62	3.06	2.94	3.55
Al	96.13	96.22	96.43	96.28	95.57	95.61	94.47
Si	0.44	0.33	0.36	0.39	0.40	0.38	0.49
Mn	0.38	0.28	0.31	0.29	0.37	0.40	0.37
Fe	0.05	0.10	0.05	0.07	0.11	0.11	0.23
Cr	-	-	-	0.11	0.17	0.22	0.35
Zr	-	0.13	0.12	0.10	0.18	0.23	0.33
Ti	0.13	0.05	0.10	0.13	0.14	0.07	0.21

Figure 5.8 presents the SEM images of the Z1 and Z2 alloys with the EMPA maps of Zr distribution across the marked area. During solidification transition metals (Zr, Cr) segregate to the Al-dendrites [46]. Zr, with k ~2.5 [42], is enriched at the aluminum dendrite core and lean at the dendritic edge. It can be seen that the interdendritic area in these alloys is slightly poor with Zr. An increase in the Zr content leads to an enrichment in the α-Al solid solution.

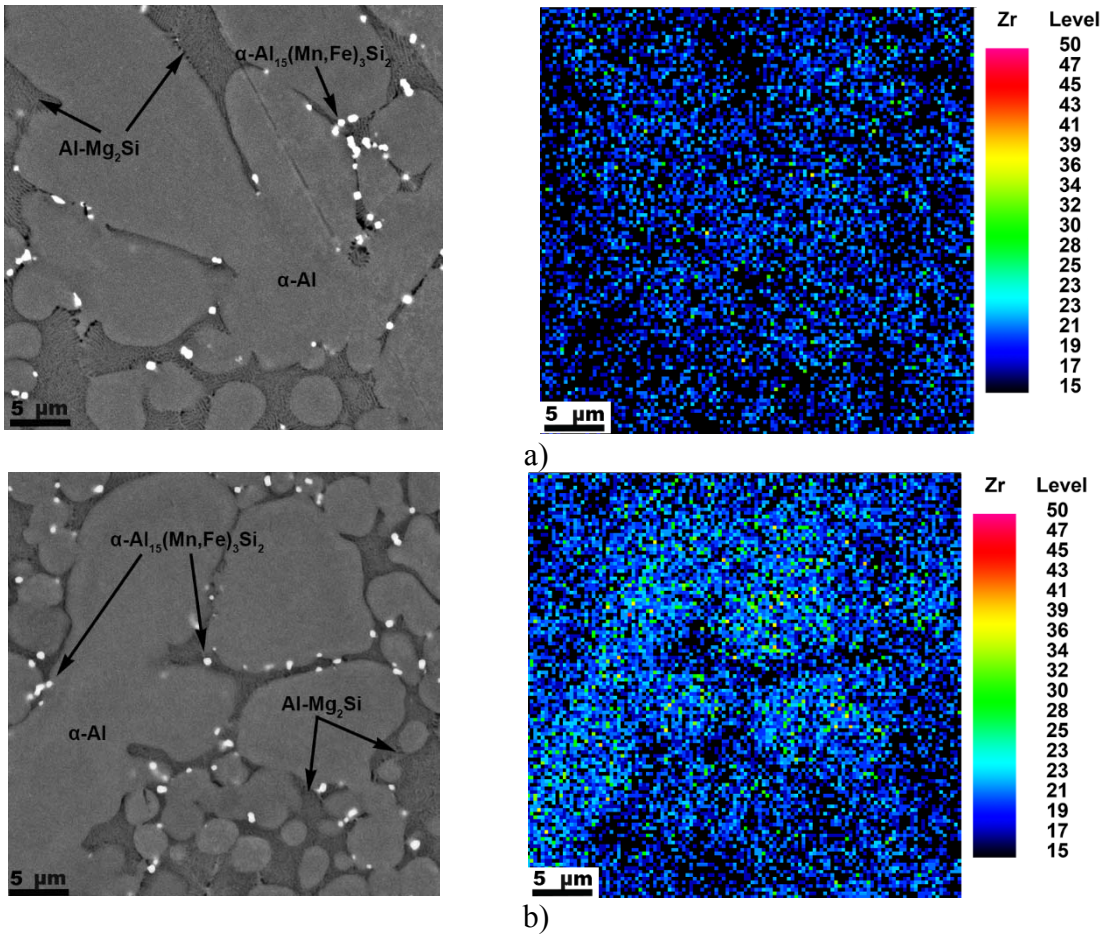

Figure 5.8 EMPA maps of the distribution of the Zr in a)Z1 alloy and b) Z2 alloy

The distribution of Cr and Zr in the CZ11 and CZ12 alloys is given in **Figure 5.9**. Cr (k~2.0) as well as Zr is also enriched at the dendrite core and lean at the interdendritic edge. Moreover, a high amount of Cr in these alloys is presented in the Mn-containing phases (k_{Mn}~1). An increase of Cr and Zr (CZ22 and CZ33 alloys) enriches more intensively the α-Al. The excess of Cr and Zr accumulates, which leads to Al_3Zr and Al_7Cr formation (**Figure 5.14**).

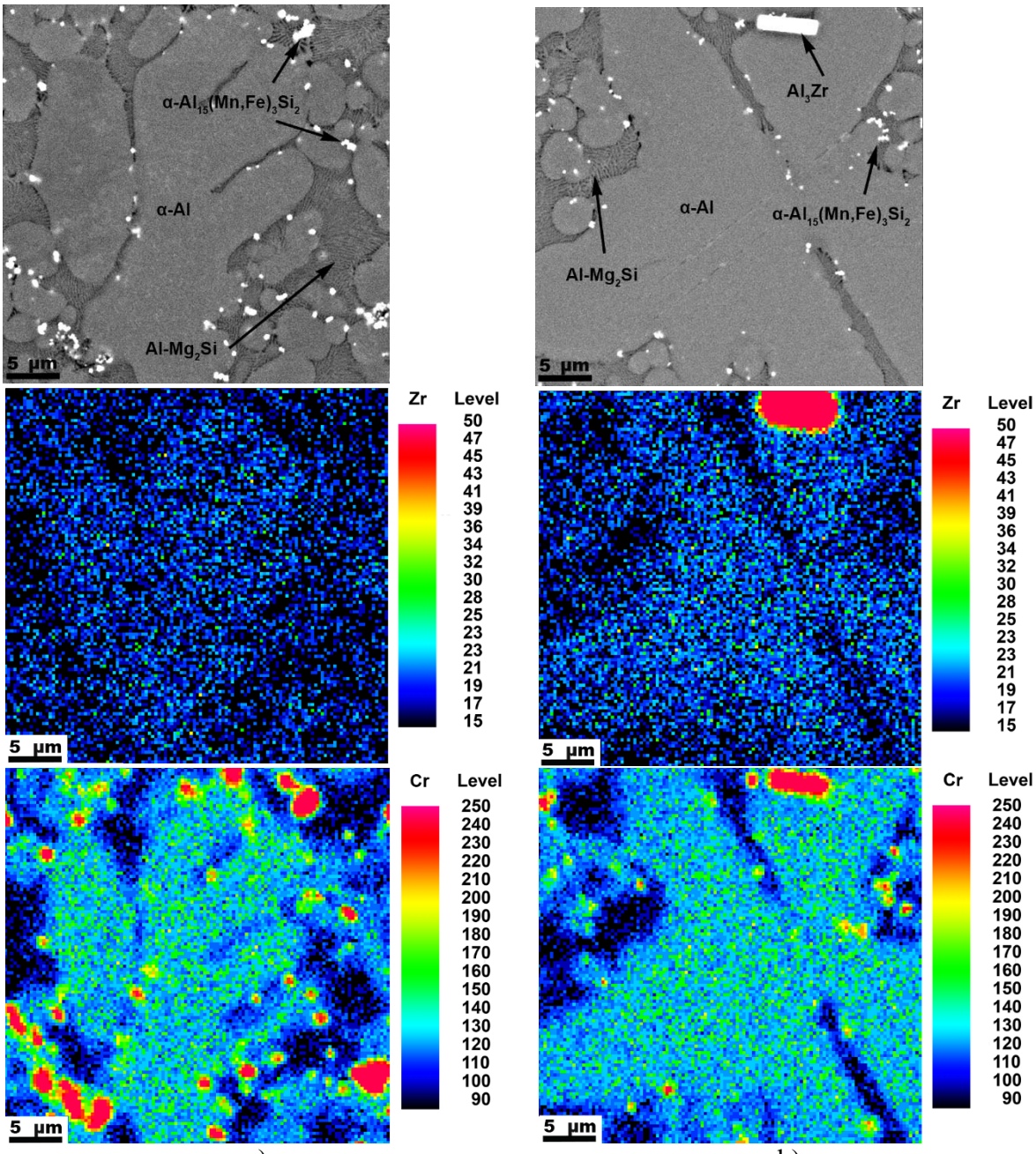

Figure 5.9 EMPA maps of the distribution of the Zr and Cr in a)CZ11 alloy and b) CZ12 alloy

5.2.2 Effect of Sc and (Sc+Zr) addition

The microstructure of the Sc-containing alloys is similar to the base material and consists of the same phases: α-Al solid solution, Al+Mg_2Si eutectic and α-$Al_{15}(Mn,Fe)_3Si_2$ phase (**Figure 5.10**). In the S1 and S2 alloys a small bright phase with an irregular shape was observed. According to the calculated phase diagram (**Figure 3.9**) and EMPA analysis (**Figure 5.11**) this phase can be identified as Al_3Sc. In the SZ11 and SZ21 alloys, apart from Al_3Sc, Al_3Zr phase is also presented (**Figure 5.14**).

The EDX analysis of the solid solution is presented in **Table 5.5**. Such small additions of Sc and Sc+Zr do not bring a reduction in the Mg content in the α-Al. Consequently the mechanical properties in as-cast state can be improved by solid solution strengthening. The Al_3Sc phase is mostly located near the α- $Al_{15}(Mn,Fe)_3Si_2$ phase and has a similar contrast on the SEM images to the α- $Al_{15}(Mn,Fe)_3Si_2$ (**Figure 5.10**), hence its identification becomes more difficult. Zr and Sc do not change the chemical composition or morphology of the Mn-containing phase.

Table 5.5 Average composition of the α-Al solid solution

	Alloy				
Element, wt. %	M59	S1	S2	SZ11	SZ21
Mg	2.86	2.83	2.57	2.85	2.68
Al	96.13	95.94	96.34	95.62	96.17
Si	0.44	0.40	0.41	0.56	0.35
Mn	0.38	0.43	0.29	0.47	0.29
Fe	0.05	0.07	0.04	0.16	0.07
Sc	-	0.15	0.19	0.17	0.18
Cr	-	-	-	-	-
Zr	-	-	-	0.07	0.11
Ti	0.13	0.21	0.16	0.10	0.16

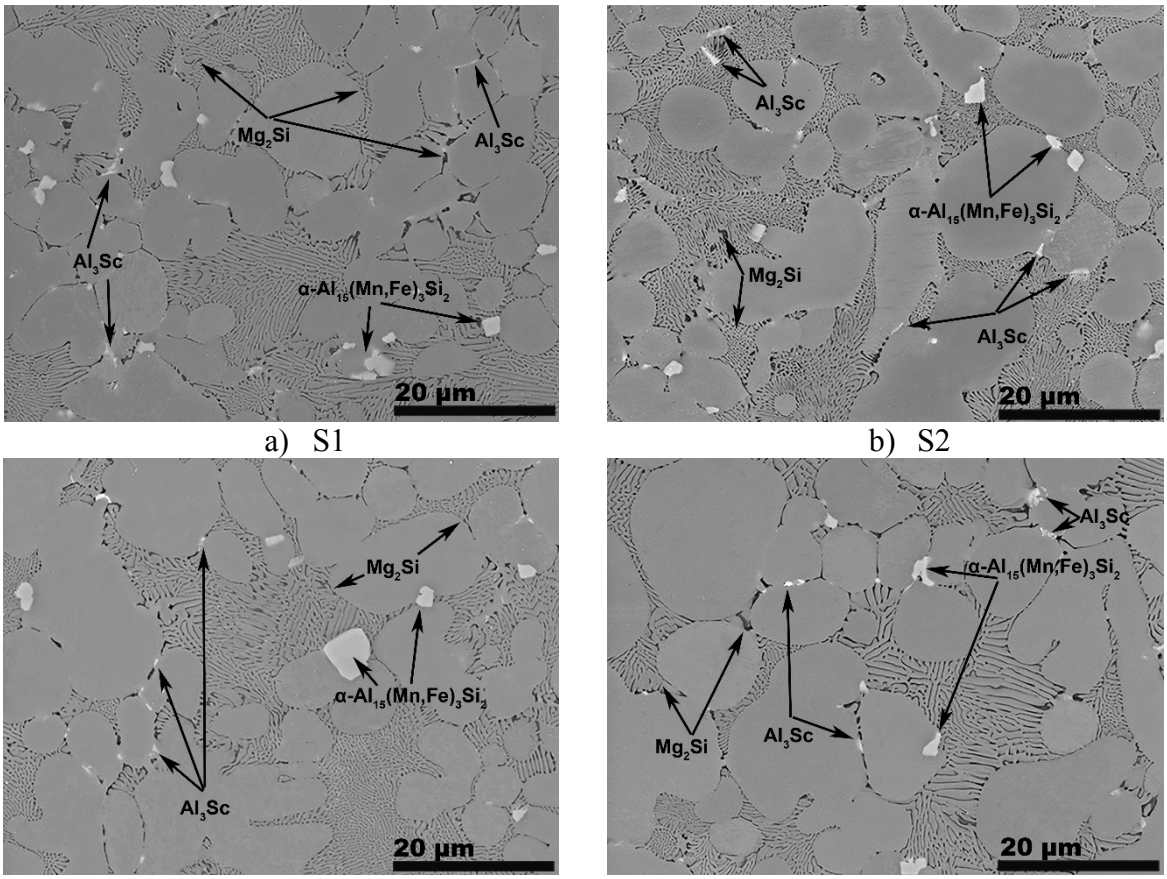

Figure 5.10 SEM micrographs of the Sc-containing alloys

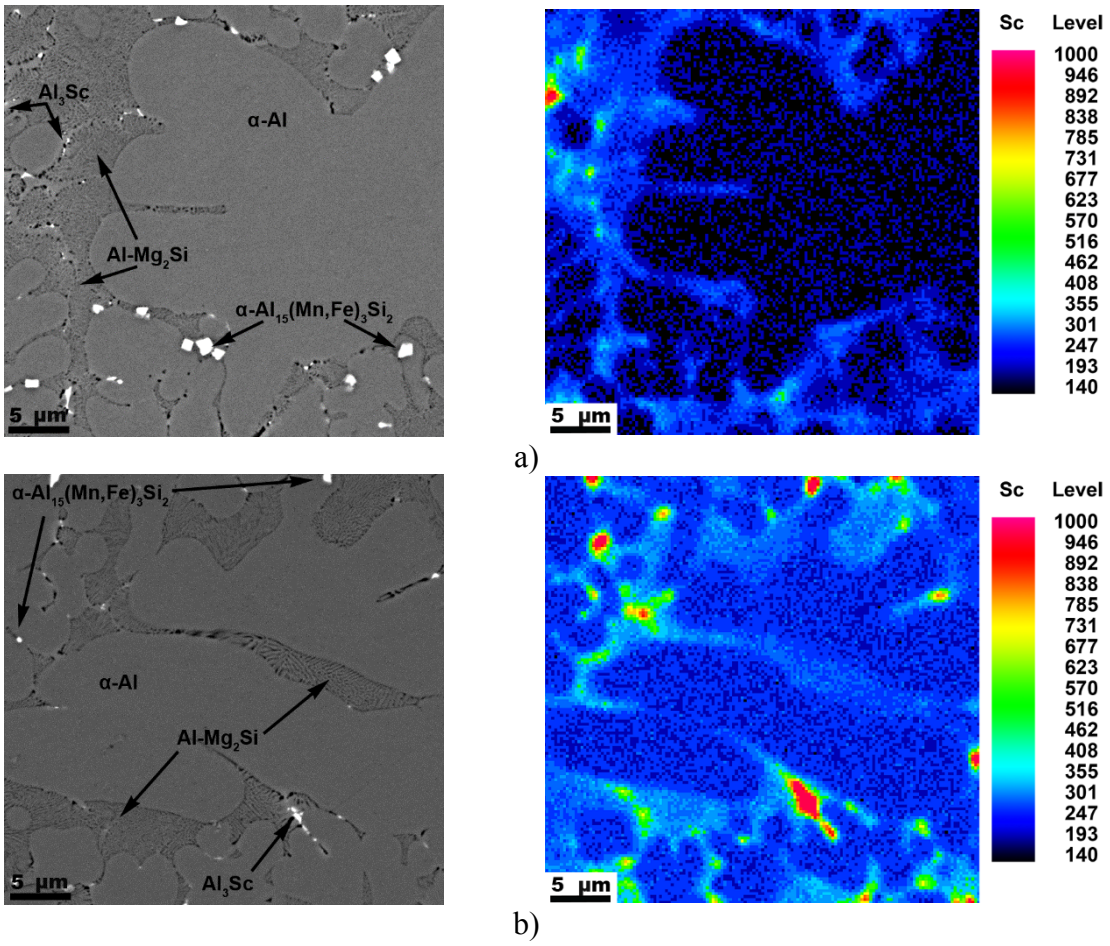

Figure 5.11 SEM images and EMPA maps of the dendritic area of a) S1, b) S2 alloys in as-cast state

The EMPA maps of the alloys with the Sc addition are presented in **Figure 5.11**. In contrast to Zr and Cr, Sc has little tendency for segregation in the Al (k~1.0) and is mainly located in the interdendritic area.

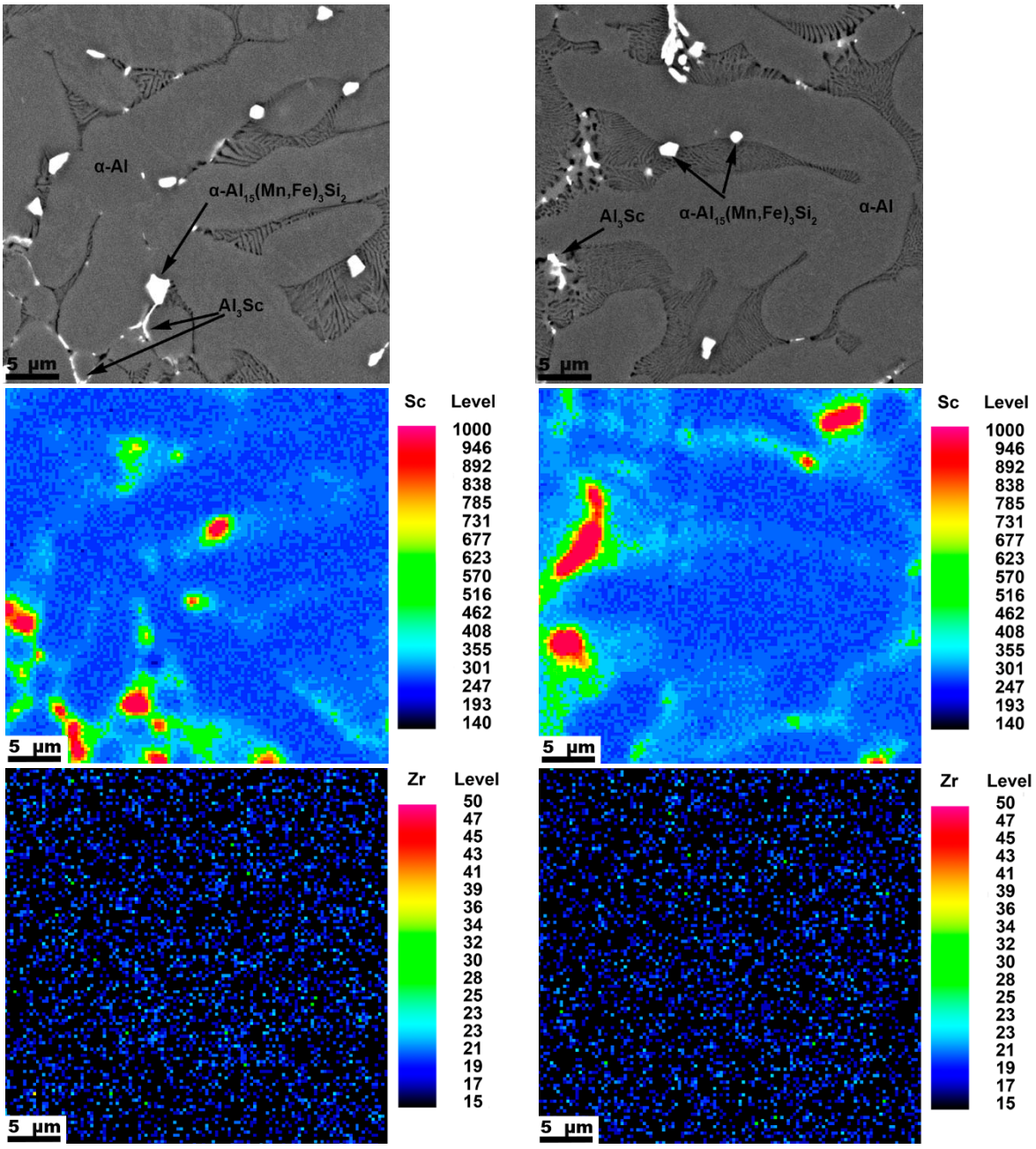

a) b)

Figure 5.12 SEM images and EMPA maps of the dendritic area of a) SZ11, b) SZ21 alloys in as-cast state

The EMPA maps of the alloys with the combination of Sc+Zr additions are presented in **Figure 5.12**. The behaviour of the Zr and Sc was described above in the Section 5.2.1.

5.2.3 (Mn,Fe)- and (Zr)-, (Cr)-containing phases

Mn-containing phases. It is well known that Fe has a low solubility and in Al-Mg-Si alloys bonds together with silicon in acicular-shaped intermetallic inclusions, which leads to reduced strength and ductility in the alloys. In order to neutralize this negative effect such alloys can be additionally alloyed by a low amount of Mn [78–80].

Table 5.6 Average composition of Mn-containing phase in base alloy

Phase name	Chemical composition, at.%					
	Mg	Al	Si	Mn	Fe	Ti
α-$Al_{15}(Mn,Fe)_3Si_2$, (blocky-shaped, stable phases)	3.5	75.9	7.3	10.1	3.0	0.1

E. Georgatis *et.al.* [78] found that in alloys with an excess of Si (Al-7Mg-5Si), in addition to the Al+Mg_2Si eutectic, Al-Si eutectic was formed. However, after addition of Mn to the same composition, the Al-Si eutectic was not detected [81]. The morphology of the Mn-containing phase observed in the base alloys is shown in **Figure 5.13**. Chemical composition and stoichiometry of the base alloy are represented in **Table 5.6**. These phases can be identified as α-$Al_{15}(Mn,Fe)_3Si_2$ and can be present in the alloy in the different forms, such as hexagonal or cubic (**Figure 5.13**) [44].

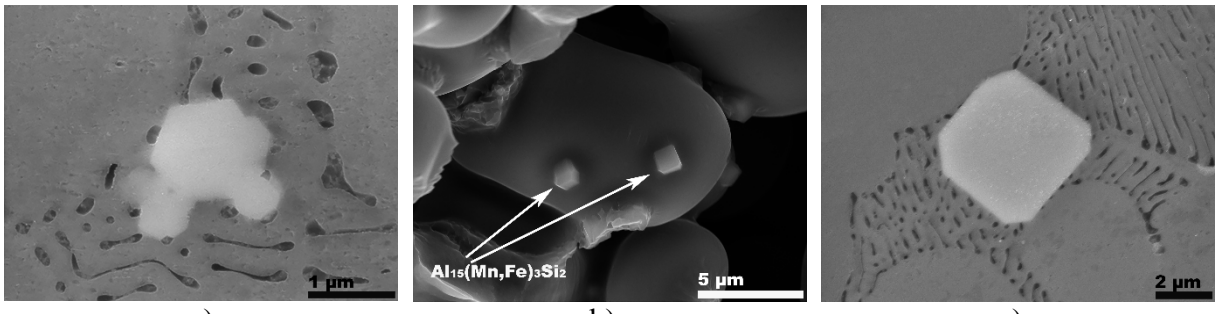

a) b) c)

Figure 5.13 SEM image of the Mn-containing phase in the base alloy. a) polished sample, b) fracture surface and c) Mn-containing phase in Sc-containing alloy.

It was also found, that the optimum Mn content in order to prevent a negative effect of Fe is 0.2% [156]. Nevertheless, with the low concentration of Mn in Al-Mg-Si alloys,

β- AlFeSi particles can be formed [157,158]. **Figure 5.13 (c)** presents a Mn- containing phase in the Sc-containing alloys. The mean size slightly varies compared to the base alloy. For the M59 the average size of the α- $Al_{15}(Mn,Fe)_3Si_2$ is equal to 1.5±0.2 μm, whereas for CZ11 is 1.3±0.3 μm and 1.7±0.3 μm for SZ11 alloy. Chemical composition, as in the base alloy, contains from 10-14 wt. % of Mn and 3- 7 wt. % of Fe. Cr is also presented in the Mn-phase in the alloys of CZ-series, thus forming a stable compact α- $Al_x(Fe,Mn,Cr)_ySi_z$ (and/or $Al_{12}(Cr,Mn)$) intermetallics [115,140,158].

Table 5.7 Chemical composition of the Al_3Zr and Al_7Cr intermetallic phases presented in the investigated alloys

	Phase	
Element, at %	Al_3Zr	Al_7Cr
Mg	0.8	1.5
Al	77.4	85.2
Si	0.3	1.2
Zr	20.7	-
Cr	-	5.0
Ti	0.3	1.2
Mn	0.3	5.5
Fe	0.2	0.4

Figure 5.14 and **Table 5.7** present the shape and composition of the coarse intermetallic phases in the investigated alloys. In the Z2, according to the thermodynamic calculations (**Figure 3.9**) and microstructural analysis, the Al_3Zr intermetallics are found. These have an orthogonal shape with an average size of 13.3±1.5μm. In the alloys with a low amount of the Cr (0.1 wt. %), e.g. CZ11 and CZ12, Cr only enriches the solid solution. With an increase of both elements up to 0.2 and 0.3 wt. % (CZ22 and CZ33 alloys), the solid solution is already enriched by the elements and an excess of Cr and Zr leads to the formation of Al_3Zr and Al_7Cr intermetallic phases (**Figure 3.9** and **Figure 5.14**). The shape of the Al_3Zr phase in the CZ33

alloy changes slightly from orthogonal and becomes longer and more needle-like with a length in the range 23-75μm. The detailed quantitative analysis is given in **Table 5.11**.

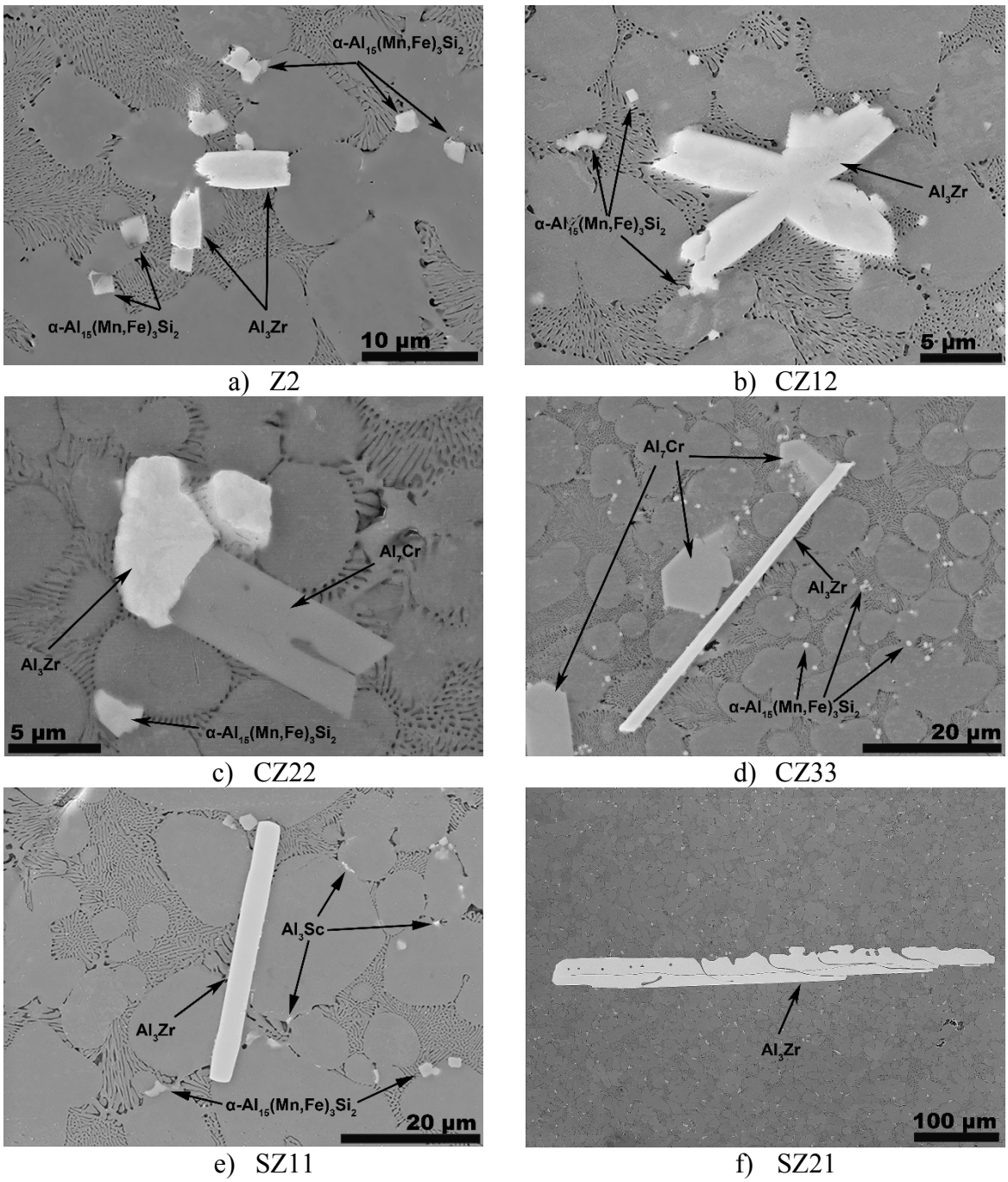

Figure 5.14 SEM images of the alloys with coarse Cr-, Zr- containing phases [159]

The Al_3Zr primary phase in Sc-containing alloys (SZ11 and SZ21) was observed (**Figure 5.14 (e-f)**). The average length and width exceed the dimensions of those in the Sc- free alloys. Length in the SZ11 is equal to 39±12.50μm with a width of 4μm, whereas in the SZ21 alloy it reaches 205±54.70μm with a width of 20μm.

In **Figure 5.15** the difference in shape and composition of Al_3Zr and Al_7Cr intermetallic phases can be clearly seen. It is observed that the Zr containing phase also contains a significant amount of Ti, while the Cr containing phases also contain Mn. The amount of Al in the Cr-rich phase is higher compared to the Zr-rich phase. Cr-rich phases were only formed in CZ22 and CZ33 alloys. These intermetallic phases have a globular shape, therefore the aspect ratio can better represent the size of these phases. Nevertheless, the average length for the longest side of these phases has been measured and presented in **Table 5.11**. For CZ22 alloy the aspect ratio varies from a minimum of 1.4 to a maximum of 3.5, while in alloy CZ33 essentially bigger globular phases with values of aspect ratios varying from 1.2 to 5.8 can be found.

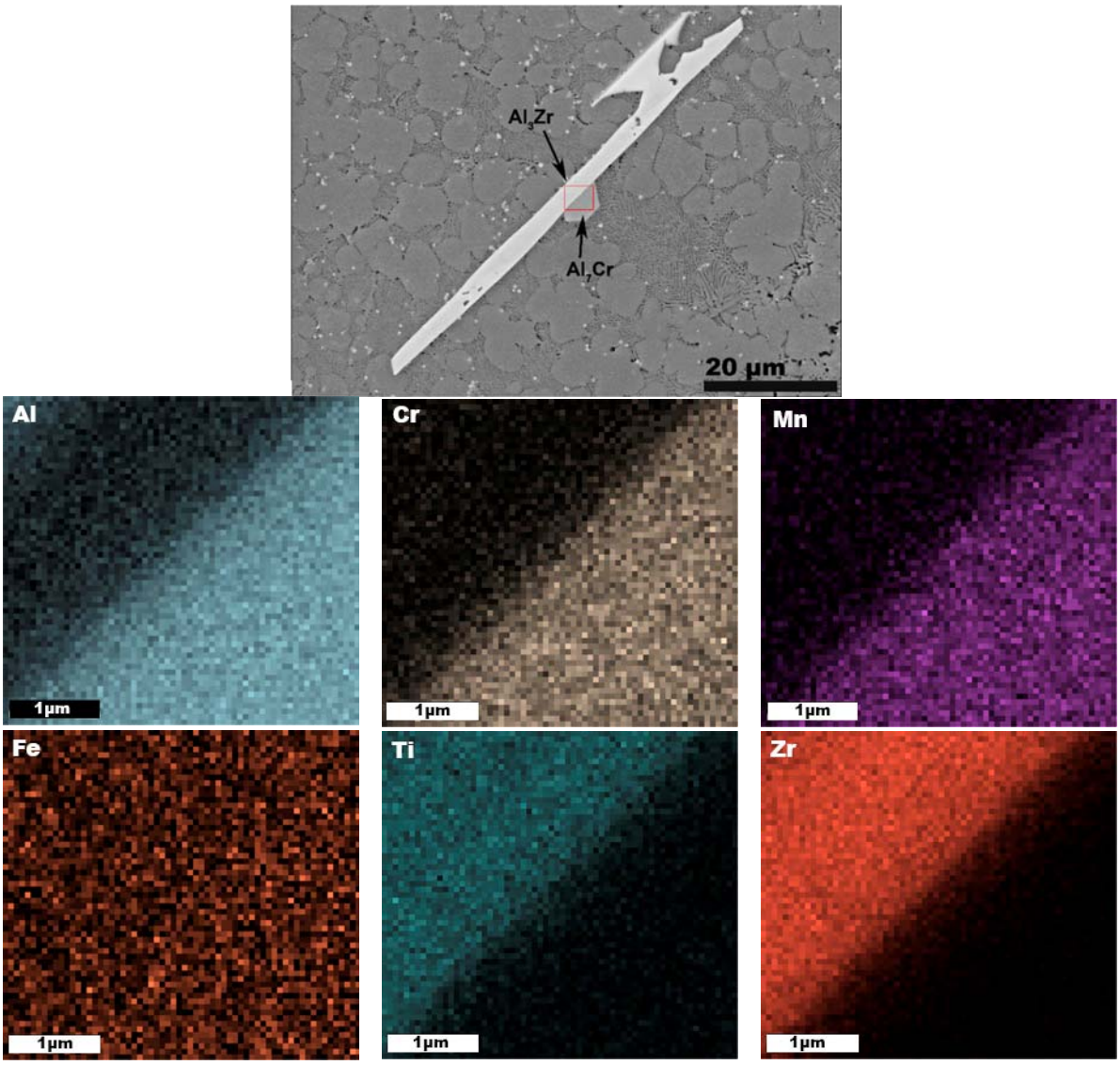

Figure 5.15 SEM micrograph and EDS elemental mapping of the Al_7Cr and Al_3Zr intermetallic phases in the CZ33 alloy [159].

5.2.4 TEM study

Figure 5.16 shows bright-field images of the base alloy. The images are obtained by tilting the sample so that the electron beam is parallel to one of the <100> directions of the Al matrix and the precipitates are aligned along the <100> direction of the α-Al matrix. **Figure 5.16a** presents an overview of the base alloy structure. Two types of precipitates were found in the base alloy in the as-cast state: β' and β-Mg_2Si phases (**Figure 5.16 (b-c)**). The cubic or square platelet-shaped β-Mg_2Si is the stable phase in the Al-Mg-Si system. In the base alloy the side length of the β-Mg_2Si phase ranges from tens of nanometres to 1-2 μm. The β' precipitates have a have rod-like shape with length 50-200 μm and elongated in the $<100>_{Al}$. In the Al-Mg-Si alloys other types of precipitates such as β" or GP-I zones (see Chapter 2 and 3) can be formed. In the investigated alloys, however, they were not observed. Some amount of a cubic shaped α-AlMnFeSi dispersoids with an average size of 10 to 20 nm was found in all investigated samples (as an example **Figure 5.17(a-b)**). All observed precipitates have been determined and distinguished in accordance with their size and morphology.

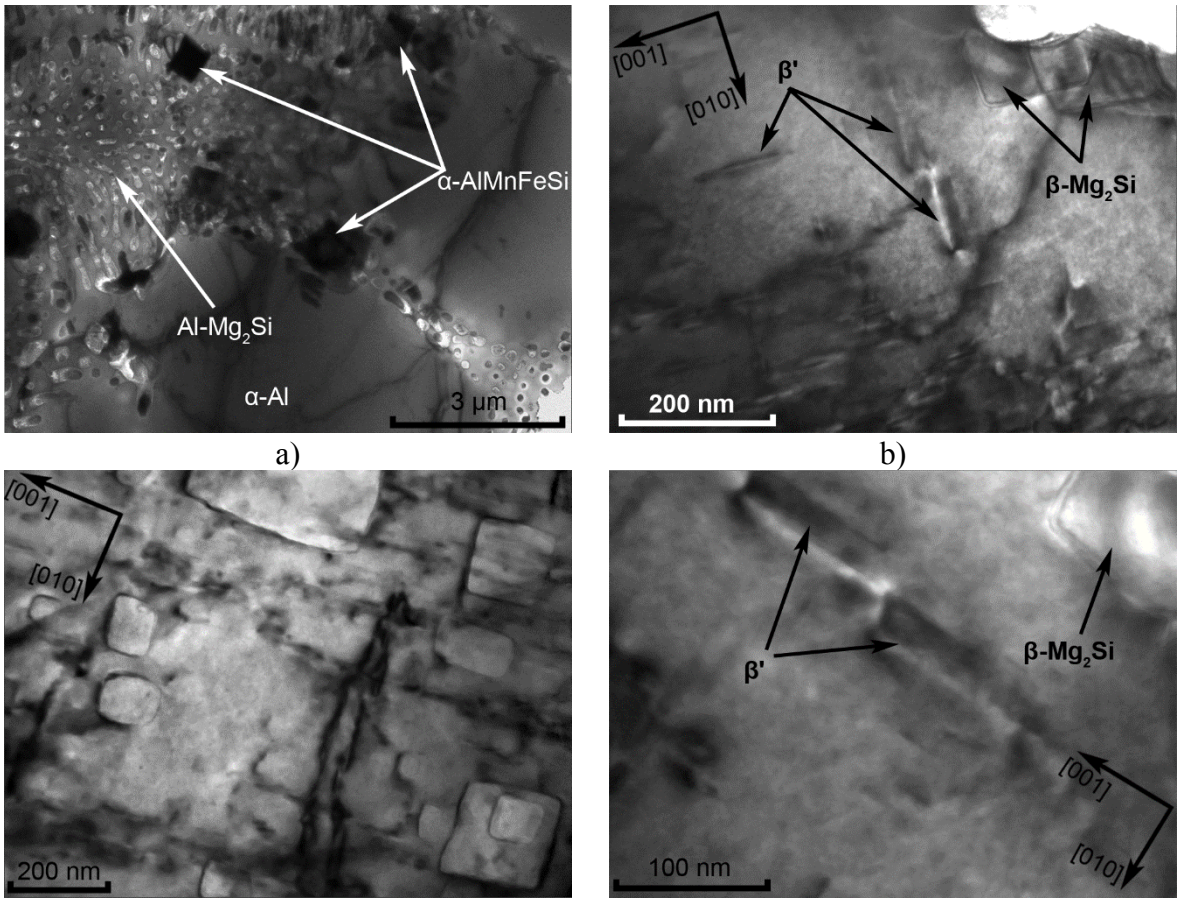

Figure 5.16 TEM bright-field images of the a-c) base alloy with the β and β' precipitates in the base alloy.

The as-cast structure of α-Al dendrites of the Z2 and S2 alloys is similar to the M59 (base alloy) alloy. In the Zr-containing alloys Al_3Zr precipitates have not been observed. In alloys with addition of Sc, a small amount of Al_3Sc precipitates was observed (**Figure 5.17(a-b)**). Al_3Sc precipitates have cubic shape with a mean size ranging from 5 to 15nm.

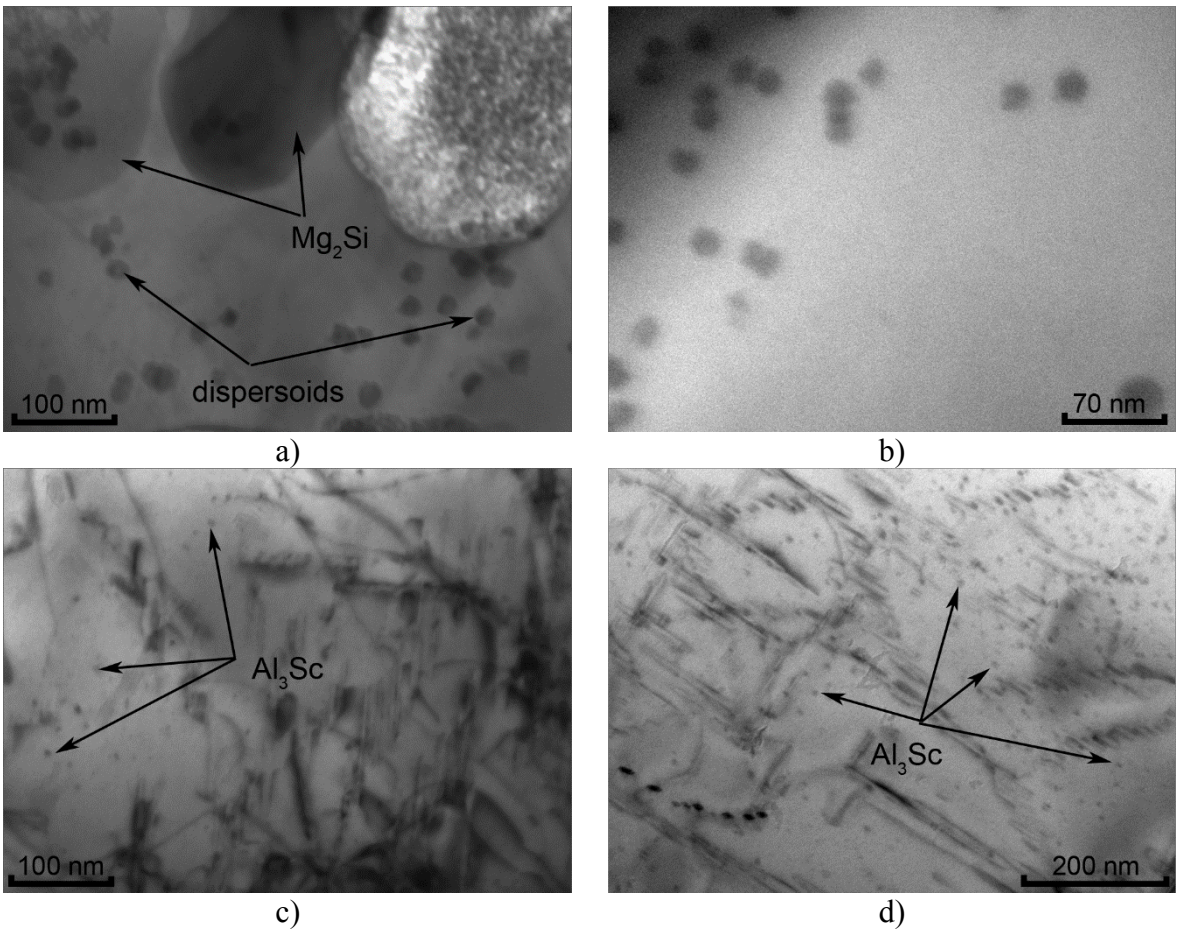

Figure 5.17 TEM bright-field images of the a- b) Mn-containing dispersoids in the base alloy and Al_3Sc precipitates observed in b)S1 and c)S2 alloys

5.3 Quantitative description of microstructure changes

Figure 5.18 shows a cross-section together with the volume fraction of the α-Al and eutectic close to the edge region and in the middle section of the plate (area between two red lines in **Figure 5.18a**). In close proximity to the edge region (skin), which is around 1.2 mm, the primary α-Al grain size is small and a higher amount of Al+Mg_2Si eutectic was observed. But in the mid-central region the situation is vice versa.

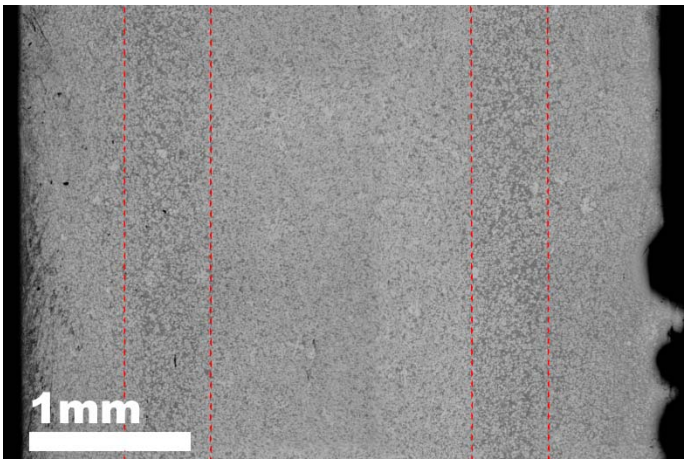

a)

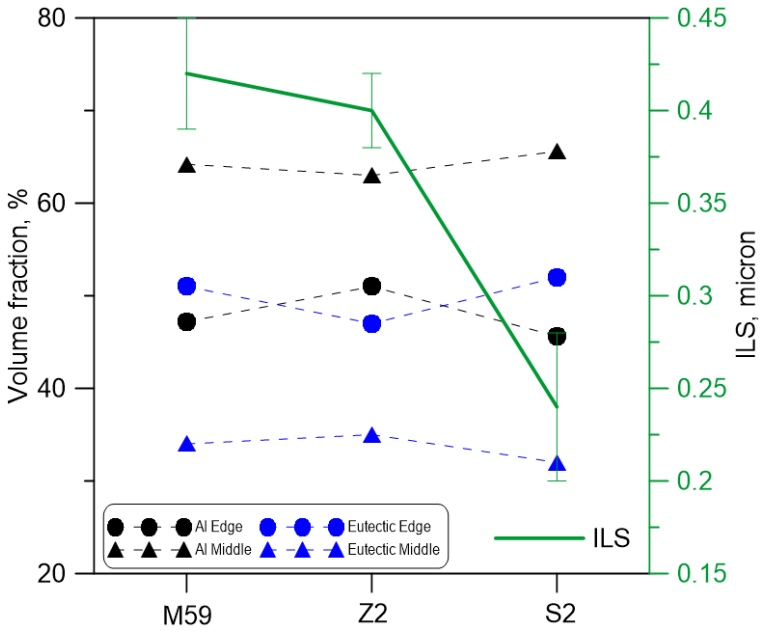

b)

Figure 5.18 a) Cross section of the plate and b) volume fraction of the α-Al and eutectic close to the edge region and in the middle part of the plate, ILS for the middle region plotted for M59, Z2 and S2 alloys.

The mean DAS and ILS values of the investigated alloys are given in **Table 5.8**. The mean DAS is near the same for the all investigated alloys. The ILS of the Al-Mg_2Si eutectic structure in the base alloy is equal to 0.42μm. The addition of Zr does not appear to have a significant effect on the morphology and the mean value of ILS remains in the same range similar to M59 alloy (**Figure 5.18**, **Table 5.8**). A combination of the Cr and Zr leads to a stronger effect on the ILS (reducing from 0.37μm in alloy CZ11 to 0.2μm in alloy CZ22 and CZ33). The addition of Sc in an amount of 0.2 wt. % decreases ILS down to 0.24 μm. The combination of Zr+Sc (SZ11 and SZ21alloys) leads a more pronounced decrease in the ILS (0.09 μm and 0.07 μm respectively).

Table 5.8 DAS of the α-Al and ILS of the eutectic calculated for the investigated alloys.

Alloy	DAS, μm	ILS, μm
M59	12.3±7.3	0.42±0.03
Z1	11.2±4.2	0.41±0.02
Z2	11.4±4.9	0.40±0.02
CZ11	10.9±3.6	0.37±0.02
CZ12	11.2±4.1	0.25±0.02
CZ22	10.8±3.7	0.20±0.02
CZ33	11.0±3.7	0.20±0.05
S1	11.1±3.9	0.26±0.04
S2	11.2±4.5	0.24±0.04
SZ11	10.4±3.5	0.09±0.02
SZ21	10.7±5.2	0.07±0.02
SCZ	11.7±5.3	0.30±0.02

Table 5.9 and **Table 5. 10** present the volume fraction (V_{meas} and V_{calc}) and mean size of the Mn-, Zr- and Cr-phases. These results were compared with those obtained from the thermodynamic calculations, by means of Thermo-Calc. The coarse Al_3Zr primary phase was observed in the Z2, CZ11, CZ12, CZ22, CZ33 of Sc-free alloys and in the SZ11, SZ21 of Sc-

containing alloys. The average length of the Al_3Zr phase (orthogonal-like shaped) in Z2 alloy is 13.3±1.5μm whereas the width amounts to 3.4±0.8μm. The average length and width of Al_3Zr phases, which were found in the CZ11, CZ12 and CZ22, are close to the Al_3Zr phase sizes, which were found in Z2 alloy respectively. In the CZ33 alloy, with the maximum amount of Zr and Cr (0.3 wt. %), Al_3Zr phase has a wide range of sizes with a minimum of 22.75 μm and maximum of 74.25 μm in the Sc-containing alloys SZ11 and SZ21 Al_3Zr phase is also presented. The average size of the Al_3Zr phase is close to the average size for the particles found in the CZ33 alloy. Some huge particles with a length of 535 μm and width of 37.52 μm were discovered. In the SZ21 alloy, Al_3Zr phase has a higher amount of huge phases, whose average width also exceeds roughly in 5 times the width of phases from SZ11 alloy.

According to the calculated phase diagrams (**Figure 3.9**) the Al_7Cr phases should be present in the alloys with Cr+Zr additions. During the microstructure analysis, however, Al_7Cr phase was observed only in the CZ22 and CZ33 alloys. This phase has an irregular block-like shape and a wide size range, therefore the aspect ratio has been measured. For CZ22 alloy the aspect ratio varies from a minimum of 1.4 to a maximum of 3.5, while in alloy CZ33 one can find bigger globular phases with values of aspect ratios varying from 1.2 to 5.8 (the average size with the standard deviation are given in Table 5. 10).

Table 5.9 Volume fraction and mean size of the intermetallic phases in the investigated alloys. Base alloys and alloys with the single addition of Zr and Sc.

Alloy	Mn-containing phase			Zr, Cr-containing phase		
	Size, μm	V_{meas},%	V_{calc},%	Size, μm	V_{meas},%	V_{calc},%
M59	1.5±0.2	1.8±0.20	1.97	-	-	-
				Zr-containing phase		
Z1	1.3±0.4	1.8±0.37	1.97	*	*	0.12
Z2	1.1±0.4	1.8±0.35	1.97	13.3±1.5	0.2±1.0	0.24
				Sc-containing phase		
S1	1.8±0.3	1.8±0.16	1.97	*	*	0.24
S2	1.7±0.3	1.8±0.15	1.97	*	0.5±0.06	0.48

*could not be measured due to the small size and inhomogeneous distribution across the sample.
V_{meas} – results of image analysis; V_{calc} – calculated with ThermoCalc software

The Al_3Sc phase, which was observed in all Sc-containing alloys (S1, S2, SZ11, SZ21), has an irregular shape and located in the interdendritic space. This phase is mostly located close to the α-$Al15(Mn,Fe)_3Si_2$ and has a similar contrast on the SEM images to the Mn-phase, thus, its identification become more complicated. Therefore, we have to rely on the results obtained from the Thermo-Calc software and use these values for the calculation of the volume fraction of α-Al and Mg_2Si eutectic.

Table 5. 10 Volume fraction and mean size of the intermetallic phases in the investigated alloys. Alloys with the combine addition of Cr+Zr and Sc+Zr.

Alloy	Intermetallic phase					
	Size, μm	V_{meas},%	V_{calc},%	Size, μm	V_{meas},%	V_{calc},%
	Zr-containing phase			Cr- containing phase		
CZ11	12.2±11	*	0.12	*	*	0.38
CZ12	15±0.30	0.24±0.05	0.24	*	*	0.38
CZ22	7.1±2.80	0.24±0.01	0.24	17.5±5	0.75±0.08	0.77
CZ33	40.7±20.40	0.38±0.05	0.36	9.6±3.4	1.16±0.08	1.15
	Zr-containing phase			Sc-containing phase		
SZ11	39.2±12.50	0.10±0.05	0.12	*	*	0.24
SZ21	205±54.70	0.12±0.08	0.12	*	*	0.48

*could not be measured due to the small size and inhomogeneous distribution across the sample.
V_{meas} – results of image analysis; V_{calc} – calculated with ThermoCalc software

5.4 Mechanical properties

5.4.1 Micro and macro hardness

The mechanical properties of the base alloy and after addition of Zr, (Zr+Cr), Sc and (Sc+Zr) were measured by microhardness ($HV_{0.1}$) testing and Brinell hardness (HB). The contact zone from the Brinell testing is large enough to cover several dendrites, including secondary phases and existing porosity. Microhardness testing was required for the α-Al. The results are summarized (macro/microhardness vs amount of alloying element) and shown in **Figure 5.19a** and **b**. The strongest effect on macrohardness was observed for the alloys with Sc and Sc+Zr additions. The SZ21 and SCZ alloys are 15 % harder than the M59. The alloy S2 with 0.2 wt. % Sc is 14 % harder than M59, but only 1% harder than the S1 alloy and has the same hardness as SZ11 alloy. The average hardness increase for alloys with 0.1 wt. % of Zr is around 7% as compared to M59. Z2 alloy shows the same hardness value as Z1 alloy. CZ11 has a small increase of hardness compared to the Zr-containing alloys, whereas after increasing the amount of Zr in CZ12 alloy a drop in a hardness value was observed. CZ22 and CZ33 alloys have a comparatively high hardness value, similar to that for alloys S1. The average hardness values for the Sc-free alloy, however, are much lower compared to those of the Sc-containing alloys.

In contrast to macrohardness, the microhardness is more affected by the amount of the alloying. Thus, the Zr-containing alloys (Z1 with 0.1 wt. % of Zr and Z2 0.2 wt. % of Zr) show a nearly constant increase when compared to the base alloy. Different combinations of the Cr+Zr consistently increase the hardness values. Alloy CZ11 with a total of 0.2 wt. % of the alloying elements (0.1 wt. % Cr and 0.1 wt. % Zr) shows an increase in HB up to 10%, whereas the increase in microhardness is only 4%. Along with the increase in the alloying elements, reaching a maximum of the 0.6 wt. % (alloy CZ33), hardness was found to rise by up to 13% compared to the base Al-Mg-Si alloy. The drop in HB for the CZ12 can be caused by the high amount of porosity in the sample. This statement can be confirmed by the microhardness measurements, where a continuous hardness increase was observed. For the Sc-containing alloys, the minimum increase shows alloy S1 (0.1 wt. % of Sc), HV=100.1 MPa, and to be 6% harder than the base alloy and 3% softer than S2 alloy. The strengthening effect of the 0.1 wt. % Sc is close to the combination of the Cr+Zr with the combined 0.4 wt. % of both elements (alloy CZ22, HV=101.94 MPa). These two alloys show close HB and HV values. Combination of the Sc+Zr shows comparable values to the results of S1 alloy. However, $HV_{0.1}$ of SZ11 and SZ21 are slightly lower in comparison with S2 alloy. S2 and SZ11 are 9.6% and 8.5% harder

as compared to base alloy. The maximum hardness values shows SCZ alloy, where HB=91.44 MPa and $HV_{0.1}$=106.2 MPa.

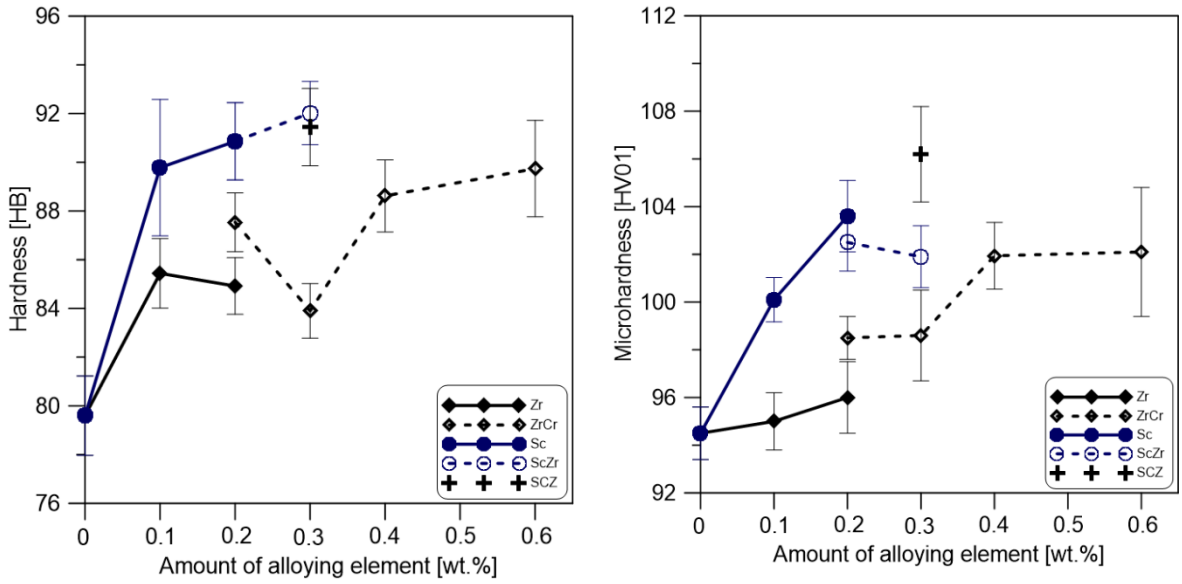

a) b)

Figure 5.19 a) Macro- and b) micro-hardness of the Sc-free alloys and Sc-containing alloys in as-cast state

5.4.3 Nanohardness measurements

Using nanoindentaion the local mechanical properties of the α-Al matrix and Al-Mg_2Si eutectic region were measured for the investigated alloys. As shown in **Figure 5.20a-b**, the hardness values of the α-Al matrix as well as eutectic region are higher in comparison to the base alloy. Similarly, in **Figure 5.20c**, the hardness values of the dendrites as well as the eutectic of the alloys with Zr, Sc and Zr+Sc additions are higher in comparison to the M59 alloy.

Figure 5.20a-b shows typical residual impressions in the α-Al dendrites and Al-Mg_2Si eutectic area. The results from the nanohardness measurements show no correlation with the amount of alloying elements within the same series of alloys (Z1 and Z2, S1 and S2, SZ11 and SZ12) but rather indicate an equal hardness range for the alloys with the same alloying element. The smallest increase of the α-Al hardness, up to 15%, corresponds to the alloys Z1 (0.1 wt. % Zr) and Z2 (0.2 wt. % Zr). Alloys with Sc addition present increases up to 22%. The combination of Zr+Sc results in a similar increase in hardness to a single addition of Sc. The same trend can be observed in the eutectic, where the highest hardness increase corresponds to the alloys with the Sc and Zr+Sc addition.

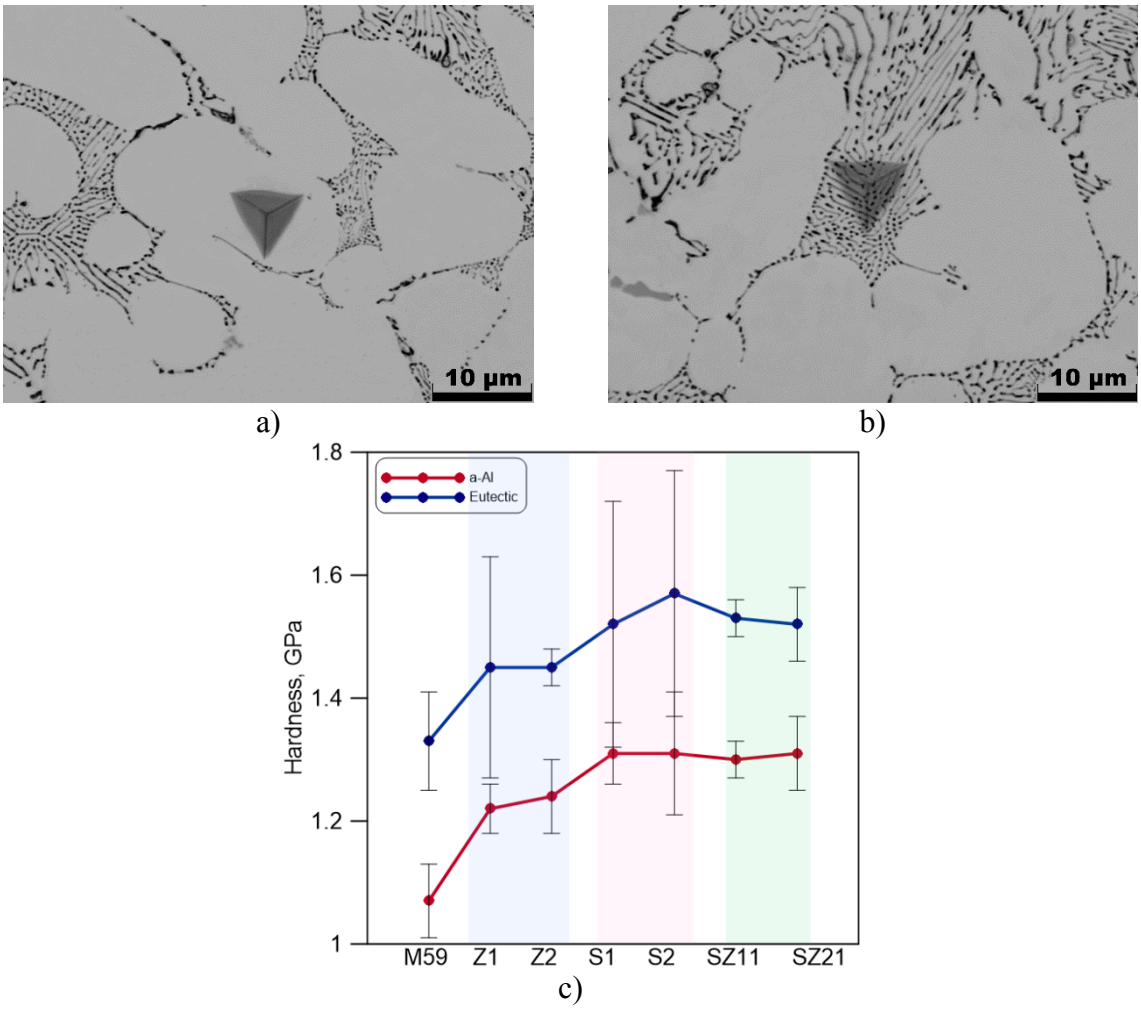

Figure 5.20 Microstructure of investigated alloy with indent in a) α-Al matrix and b) eutectic as an example, nanohardness measurements of the c) α-Al matrix and eutectic.

The indentation behaviour of the α-$Al_{15}(Mn,Fe)_3Si_2$, Al_3Zr and Al_7Cr intermetallic phases was also investigated (**Figure 5.21-Figure 5.22**). Due to their small size, not all phases present in the investigated alloys can be measured by means of nanoindentation. As an example, two indents on the α-$Al_{15}(Mn,Fe)_3Si_2$ intermetallic phase with the corresponding load-displacement curves are shown in **Figure 5.21**. It is obviously that such intermetallic phases are tiny and we cannot predict an exact thickness. Therefore a hardness evaluation should be done individually for each indent at a specific depth level. However, for most indents a hardness plateau was observed between 100-200 nm. Indent 1 shows a H=15.38 GPa at a depth range of 80-135 nm. For this specific indent (indent1) it can be seen from the image that the indent was not located directly in the centre of the phase, but closer to the edge. Clearly, at a depth of 135 nm the imprint was already too large and exceeded the phase size. Thus, with further indenter penetration, a continuous hardness reduction was observed. Indent 2, unlike indent1, is located

completely in the phase area of the α-$Al_{15}(Mn,Fe)_3Si_2$ primary phase. Hence, the maximum load reaches 40mN in contrast to 25mN for the indent 1. At the depth of 200 nm the hardness value is equal to 13.49 GPa. However, the first hardness plateau was observed earlier with the mean hardness value close to the 15 GPa.

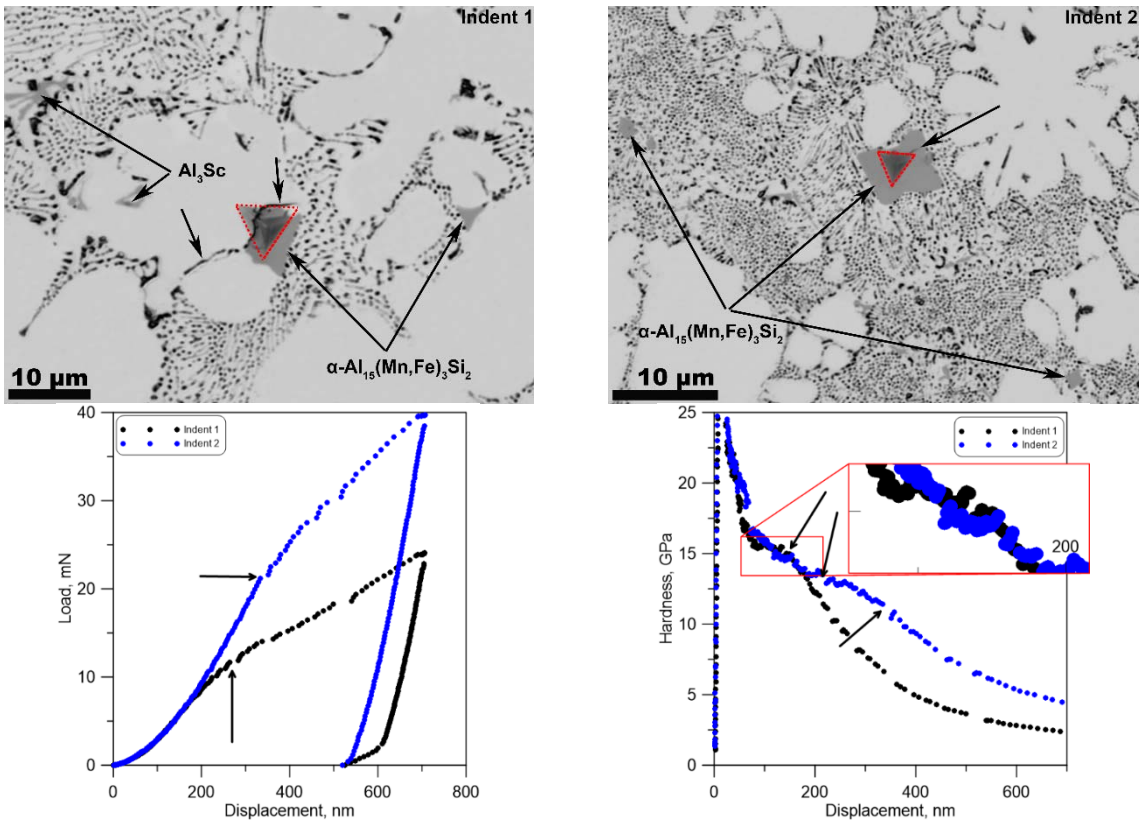

Figure 5.21 Images of the α-$Al_{15}(Mn,Fe)_3Si_2$ intermetallic phase with the corresponding load-displacement and hardness-displacement curves.

In **Figure 5.22**, the Al_7Cr phase, which was found in the Sc-free alloys with the Cr amount ≥ 0.2 wt. %, along with the corresponding load and hardness-displacements curves is shown. The size of these intermetallic phases essentially exceeds the sizes of the α-$Al_{15}(Mn,Fe)_3Si_2$ phase, thus, all indents, are located in the centre of the phase, and one typical imprint with the corresponding load-displacement and hardness displacement curves only are shown. Al_7Cr, as well as other observed intermetallics, is intrinsically brittle with a possibility of cracking. Some cracks were observed around the imprint (**Figure 5.22a**). On the corresponding hardness-displacement curve the hardness drops marked with arrows, apparently to indicate the appearance of crack. The average hardness value at 200 nm is 9.01 GPa.

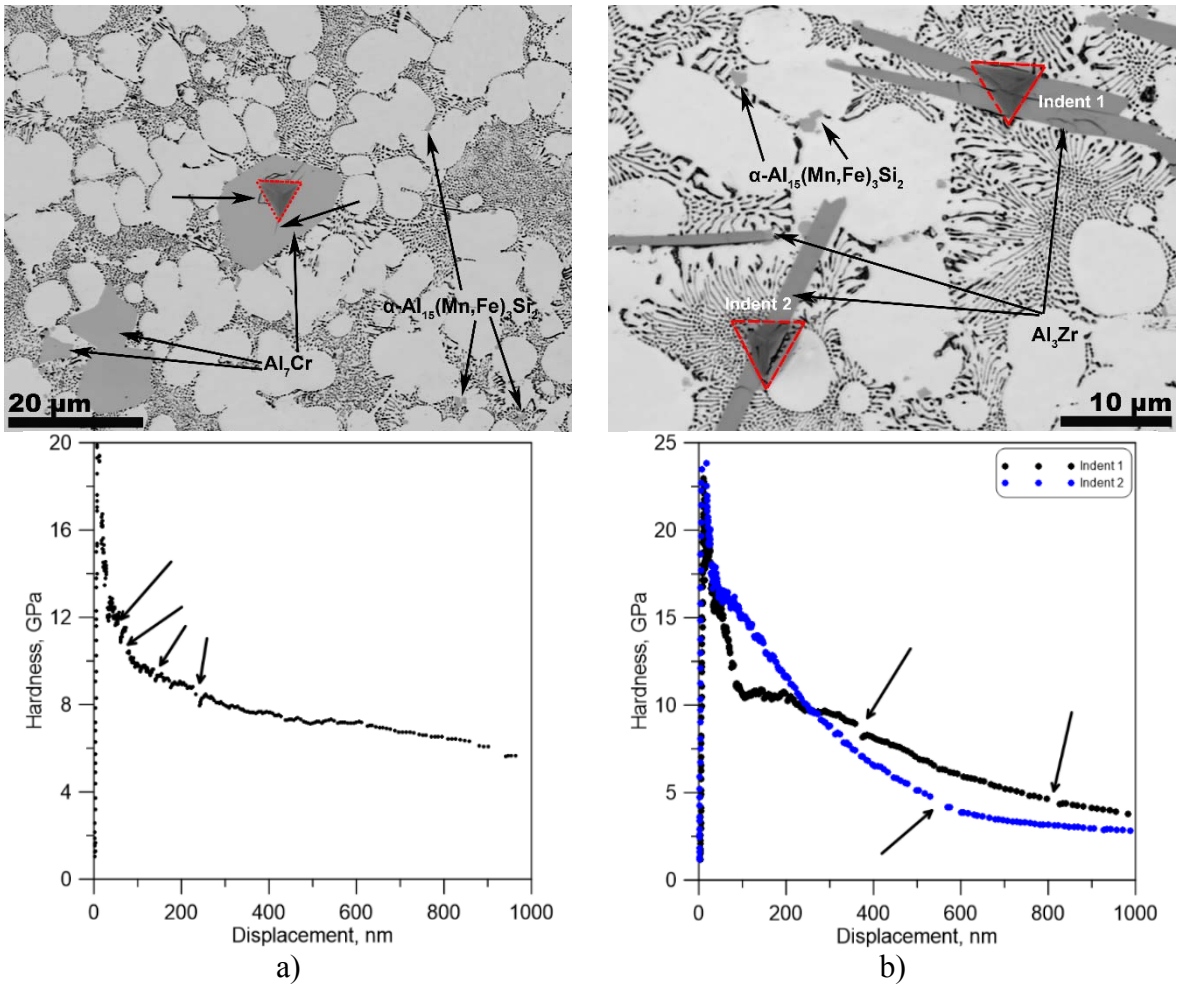

Figure 5.22 Images of the a) Al_7Cr and b) Al_3Zr intermetallic phases with the corresponding hardness-displacement curves.

The Al_3Zr intermetallic phases were observed in both Sc-free and Sc-containing sets of alloys (**Figure 5.14**). The comparative hardness-displacement curves are shown in **Figure 5.22b**. In contrast to the α- $Al_{15}(Mn,Fe)_3Si_2$ and Al_7Cr, Al_3Zr has a long needle shape, thus making the nanoindentation measurements more difficult. Several small hardness plateaus, which are followed by hardness decreases are apparent in the depth range of 100-200 nm with average hardness values of 10.5 GPa and 10.4 GPa observed. The significant hardness drops of 1.0 GPa, can be either an indication of crack initiation or an indication of exceeding the sizes of the phase by the tip contact area. The size of the Al_3Zr intermetallic phases, found in the SZ11 and SZ21 alloys, exceeds those found in Sc-free alloys, hence all indents are assumed to have reached the desired particle. Nevertheless, mean hardness values are slightly lower and equal to 9.1 GPa.

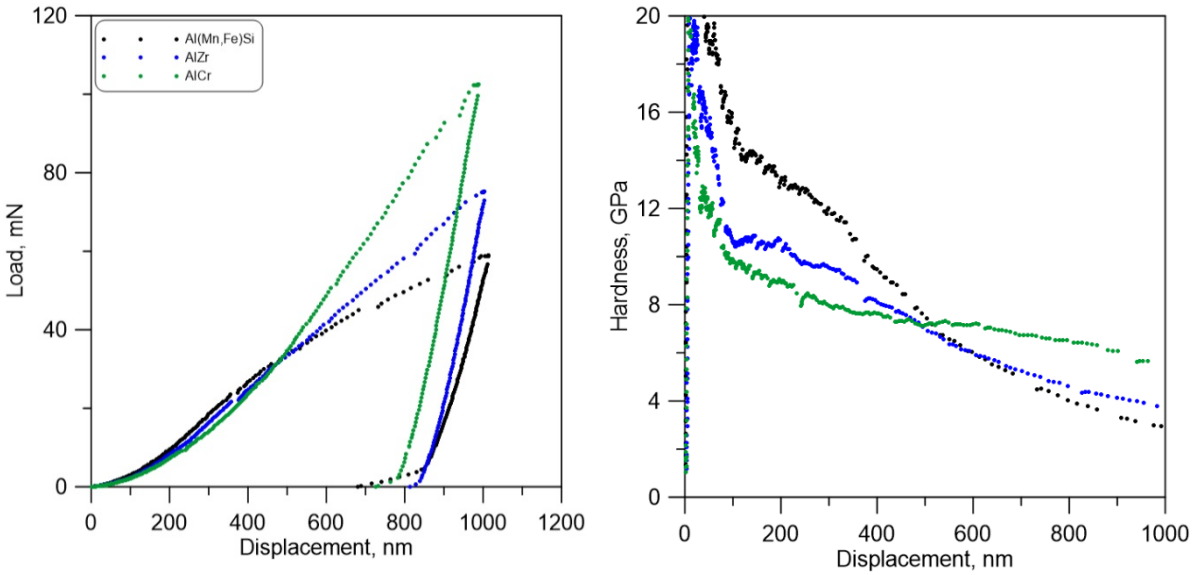

Figure 5.23 Load–displacement and hardness-displacement curves for the α- $Al_{15}(Mn,Fe)_3Si_2$, Al_3Zr and Al_7Cr primary phases.

Figure 5.23 shows the typical load-displacement and hardness-displacement curves for the α- $Al_{15}(Mn,Fe)_3Si_2$, Al_3Zr and Al_7Cr intermetallic phases, found in the investigated alloys. Hardness values of these phases are shown in Table 5.11. Since the size of the intermetallic particle is limited, the average hardness value for each intermetallic phase was evaluated at the first hardness plateau at the depth range 100-200 nm. The hardness values obtained are believed to be reliable. Nevertheless, the average hardness values were also evaluated at 200nm indentation depth. Among the investigated intermetallic phases Al_7Cr has the lowest hardness value of 9.57±0.31GPa, whereas α-$Al_{15}(Mn,Fe)_3Si_2$ has the highest hardness value of 14.55±0.9 GPa (according to Chen *et. al* [160,161] hardness of the AlFeMnSi phase in Al-Si alloy is equal to 10.82±0.29 GPa) and hardness of Al_3Zr is equal to 10.55±0.1GPa.

Table 5.11 Hardness values of the intermetallic phases, in GPa

	1st plateau	at 200 nm depth
α-$Al_{15}(Mn,Fe)_3Si_2$	14.55±0.9	12.81±0.6
Al_3Zr	10.55±0.1	8.87±0.3
Al_7Cr	9.57±0.31	9.03±0.31

5.4.2 Tensile test

The results of tensile tests plotted as a function of wt. % of alloying elements are presented in **Figure 5.24 a-c**. The yield strength in Sc-free alloys after addition of Zr and Zr+Cr is nearly constant (negligible increase up to 172 MPa for the CZ33 alloy with 0.6 wt. % of alloying elements), whilst for the base alloy this value is equal to 163 MPa. Thus, the improvement in the yield strength is only 5%. The UTS shows a small increase up to 10% for CZ11 and CZ12 alloys (0.2wt. % and 0.3wt. % of alloying elements), and a small decrease down to 5% with the further addition of Cr and Zr (CZ22 and CZ33 alloys). For Z1 and Z2 alloys the UTS has almost the same values as the base alloy. An addition of Zr does not bring any significant effect on the elongation to failure. As observed in Figure 5.24, both alloys with the Zr addition (Z1-0.1 wt. % Zr and Z2-0.2 wt. % Zr) have nearly the same elongation. Nevertheless, with the further addition of Cr (CZ11-0.2wt. %, CZ33-0.6 wt. % of alloying elements) elongation showed a 7% increase compared to base alloy. Alloys CZ12 and CZ22 showed a drop in elongation, demonstrating the same values as the base alloy.

The largest improvement in tensile properties was obtained through the addition of Sc and Sc+Zr. Alloy S1 (with only 0.1 wt. % Sc) shows an improvement in strength (332 MPa) and elongation by 11% and yield strength up to 16% (190 MPa). An increase of the Sc content up to 0.2 wt. % (S2 alloy) shows an increase in the elongation by 9%, in the yield strength (196 MPa) as well as in the tensile strength (342 MPa) up 3% in comparison with the S1 alloy. A comparison of the M59 alloy to the S2 alloy shows an improvement in the tensile strength up to 15%, in the yield strength as well as in the elongation by 21%. Dual additions of Zr and Sc (Alloys SZ11-0.2wt. % and SZ21-0.3wt. %) have close to the same values of elongation and tensile strength as S2 alloy, while yield stress shows more prominent changes (200 and 206

MPa respectively). Alloy SCZ with the 0.3wt. % of additions does not show any significant changes in the tensile properties. Yield and tensile strength remain on the same level as in S2 alloy, whereas the elongation to failure is closer to results obtained from S1 alloy.

Figure 5.25a shows the macroscopic fracture surface of the as-cast alloy tensile bar processed by HPDC for the base alloy. The fracture surface shows no significant defect or porosity. However in same samples, which have showed a very low values elongation to failure large pores were found. The enlarged fracture surface, exhibits gas porosity, which was attributed to the entrapment of air under the high speed shot of HPDC is shown in **Figure 5.25b**. **Figure 5.25c** shows the fracture morphology in a non-defect area with high magnification. No shrinkage porosity was observed on the fracture surface and the fracture occurred in ductile manner in both cases (**Figure 5.25b-c**). **Figure 5.25d-e** shows the fracture surface for the alloys with the Al_3Zr and Al_7Cr intermetallics. On both of the Al_3Zr and Al_7Cr intermetallics cracks can be seen.

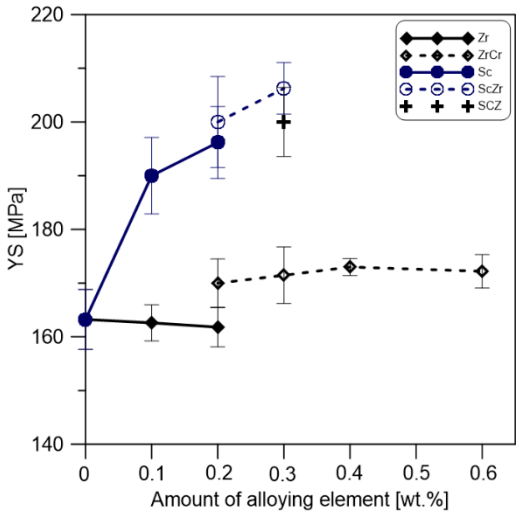

a)

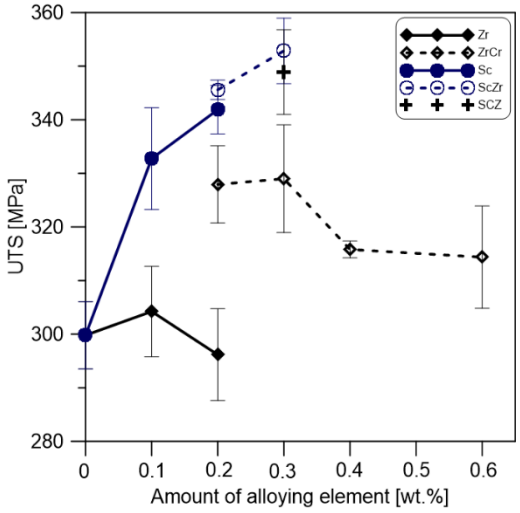

b)

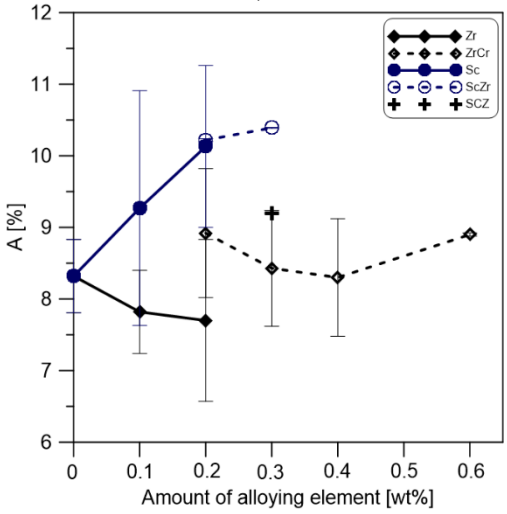

c)

Figure 5.24 Tensile properties of the investigated alloys a) yield strength b) ultimate tensile stress and c) elongation to failure in as-cast state.

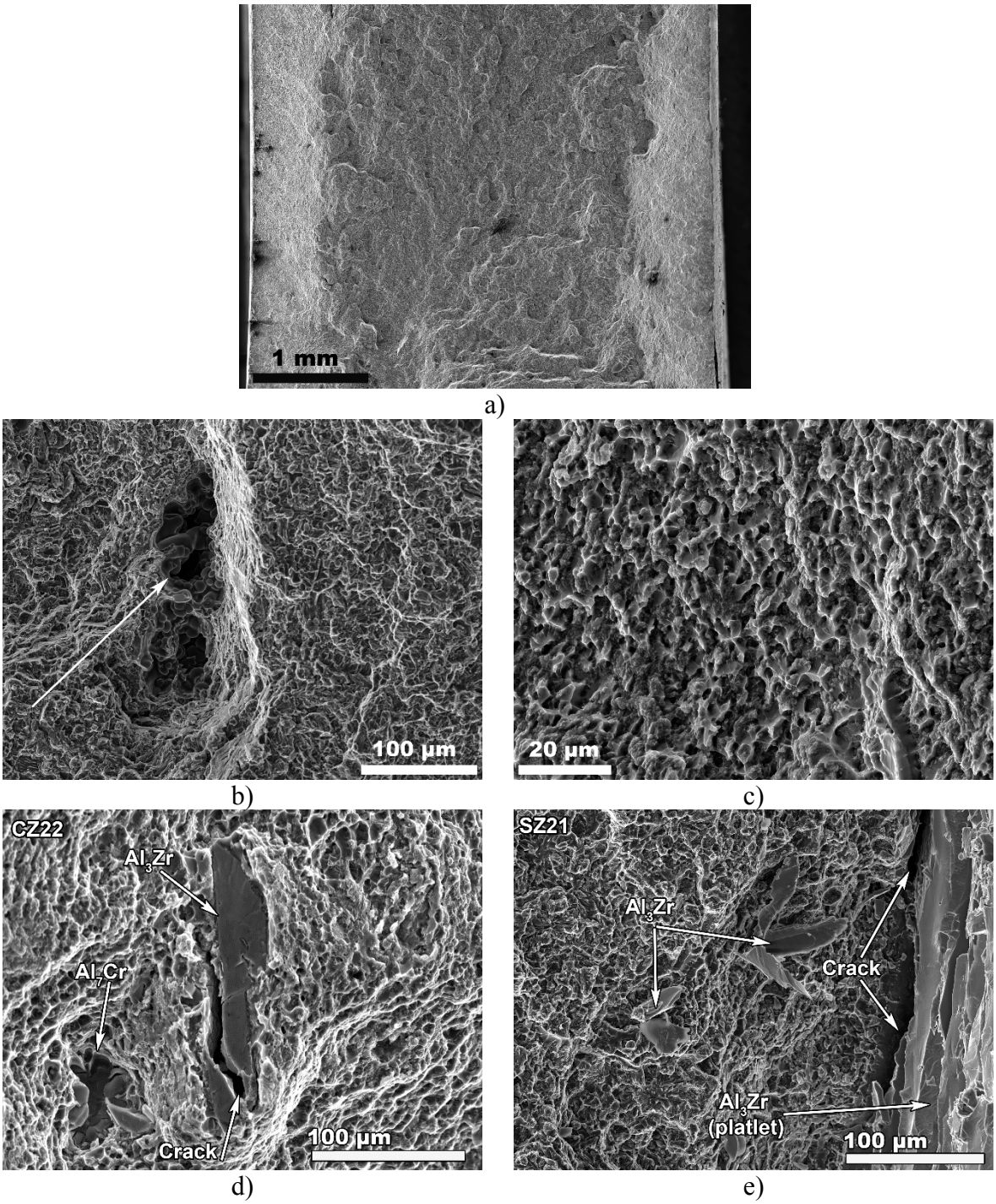

Figure 5.25 Typical SEM morphology of the fracture surface of the as-cast alloys processed by HPDC, a) macroscopic fracture of the tensile bar for the base alloy, b) pores on the fracture surface for the base alloy, c) the enlarged fracture surface of the Sc-free alloy Al_3Zr and Al_7Cr intermetallics in the d) CZ22 and e) SZ12 alloys.

5.5 Discussion of experimental results in the as-cast state

Microstructure

Changes in the cooling rate (increase or decrease depends on the casting technology) and the heat treatment at high temperatures (homogenization) [162] can affect the amount of solute in the α-Al solid solution and change the morphology of Mg_2Si particles from globular to plate-like [154,163]. Since all of the investigated alloys have been cast under the same conditions and the initial analysis was performed in the as-received state, these possibilities are excluded.

The structure of the investigated alloys consists of the α-Al solid solution, Al+Mg_2Si eutectic and the α-$Al_{15}(Mn,Fe)_3Si_2$ phase. Alloys with the addition of Zr, Cr+Zr, Sc and Sc+Zr can also have Al_3Zr, $Al_{45}Cr_7$ and Al_3Sc intermetallic phases. The presence of these intermetallics fully depends on the amount of the additions and will be discussed later. All of the investigated alloys exhibit a casting skin of around 900 -1200 μm thickness containing a region with a high volume fraction of Al+Mg_2Si eutectic and small grains of α-Al were observed (**Figure 5.18 a**). The same skin effect in HPDC samples was observed by other authors [34,164,165].

Intermetallic phases can act as obstacles to dislocation motion, leading to a strengthening of the alloy. If, however, intermetallic particles have a needle shape and/or large size (e.g. Al_xSi silicide in Al-Si alloys, Al_xFe binary or $Al_xFe_ySi_z$ ternary phases), they act as stress concentrators and can initiate cracking [81,84,115,166]. The risk of this harmful effect can be reduced by the substitution of Mn and Cr for Fe, in order to stabilize Fe- and Si-bearing phases and promote the formation of a fine and compact α- $Al_x(FeMnCr)_ySi_z$ intermetallic phase.

A substantial amount of a silicon is needed for a formation of the Mg_2Si lamellas, consequently only a relatively small amount of Si can be found in the solid solution. From the literature it is known, that the α-Al phase contains around 0.2 wt. % Si and around 2.7 wt. % of Mg at the eutectic temperature (~594°C) [88]. These values are close to those obtained from our analysis at RT (**Table 5.3-5.5**). The addition of Zr, Cr and Sc does not have a significant effect on the distribution of the main elements in the dendrite core (**Table 5.3-5.5**). The Mg_2Si phase contains 63.2% Mg and 36.8% Si, and has a cubic structure with a lattice parameter a=0.635- 0.640 nm [44]. Thus, the mass ratio of Mg to Si is 1.73:1 in Mg_2Si (corresponding to the 2:1 stoichiometry for Mg_2Si). In other words, if the ratio Mg to Si is less than 2.0, then the

alloy is designated as having an “excess of Si”. It has been discussed in the literature [81] that increased Si content can lead to the formation of less stable phases and degradation of the mechanical properties in the as-cast state.

Despite the fact, that the HPDC is considered as a casting process with a high solidification rate, in the range 10^2 to 10^3 s^{-1} [34], uneven distribution of solute (microsegregation) occurs within dendrite branches as a result of non-equilibrium solidification [41]. As was mentioned in Chapter 3, microsegregation depends on the partition coefficients. When k is close to 1, the element has little tendency for segregation in the Al (such as Mn, see **Figure 5.6**). Thus, Mg and Si, which have segregation coefficient in Al of less than 1 (~0.5 and ~0.1 respectively) [42,46], enrich the dendritic edge and mainly accumulate in the eutectic regions (**Figure 5.6**).

Due to the low solubility of Zr in Al [44], even a small addition leads to the formation of Al_3Zr intermetallic phases. These phases with an orthogonal like shape were found in the Z2 alloy, but no Al_3Zr intermetallic phase was observed in the Z1 alloy. According to the Thermo-Calc prediction (**Figure 3.9 b**), the Al_3Zr phase should also be present in the CZ11, CZ12, CZ22, CZ33 and two Sc-containing alloys (SZ11 and SZ21). Only a small amount, however, has been observed in the CZ11 alloy. This can be due to the low volume fraction of these intermetallic phases (only 0.12% according to the Thermo-Calc, see **Figure 3.9 a**) and inhomogeneous distribution across a plate. According to the EPMA maps of the Z2 alloy (**Figure 5.8**), Zr is homogeneously distributed in the α-Al dendritic core, thereby enriching the solid solution. The average size of the Al_3Zr intermetallics in the Sc-containing alloys significantly exceeds those found in the Z2 and Zr+Cr alloys. Comparing the EMPA maps from Z1-Z2 alloys (**Figure 5.8**) to SZ11-SZ21 alloys (**Figure 5.12**), it was noted that the amount of Zr in solid solution in the SZ-series is almost negligible, in contrast to Zr- series. Apparently, Sc is ‘expelling’ the Zr from the solid solution, hence all the Zr is forced to accumulate in the Al_3Zr intermetallic phases (**Figure 5.8** and **Figure 5.12**). In other words, Sc reduces the solubility of Zr in the liquid phase, which leads to an increase in the size and number of Al_3Zr intermetallic phases. On the other hand, these large phases can be a part of the master alloy and may not have time to dissolve. However, micropores should have formed around them, as in this case, they behave as an obstacle for melt during filling the mold. Furthermore, microstructural analysis did not reveal any porosity around these particles, thus it can be assumed they were formed during the crystallization process.

Cr has a peritectic reaction with aluminum (with k=2, [42]) and exhibits a solute rich segregation. Moreover, Cr can be tied up with trace elements, thus forming stable α- $Al_x(Fe,Mn,Cr)_ySi_z$ (and/or $Al_{12}(Cr,Mn)$) intermetallics [115,140]. A small amount of Cr was found in the Mn-containing phase in the Zr+Cr containing alloys (**Figure 5.9**). $Al_{45}Cr_7$ according to the thermodynamic calculations (**Figure 3.9 b**) should present in all alloys containing a Cr addition. The calculated volume fraction of $Al_{45}Cr_7$ is 0.38 for CZ11 and CZ12 alloys, which is higher than the calculated volume fraction of Al_3Zr in CZ12 (0.24) (**Table 5. 10**). However, these intermetallics have been observed only in CZ22 and CZ33 alloys. Perhaps, the amount of these phases is too low and all phases were accumulated in another part of the plate.

According to the EMPA measurements of the Sc-containing alloys (**Figure 5.11** and **Figure 5.12**) and the value of the partition coefficient, Sc is distributed in the α-Al dendritic core as well as in the interdendritic area [167,168]. At concentrations above the point of the peritectic reaction, according to literature data [44,58], a new phase Al_3Sc is formed. This is in full agreement with the calculated phase diagram (**Figure 3.10 a, b**). According to the calculated phase diagram the peritectic reaction occurs at concentration of ~ 0.1%Sc. Both microstructural and EMPA investigation confirm the presence of Al_3Sc in the Sc-containing alloys. The dendritic core is slightly poor with the Sc, hence it is mainly segregates into the interdendtitic regions (**Figure 5.11** and **Figure 5.12**) [167,168].

It was found that the addition of Cr, Zr and Sc together with a combination of Cr+Zr and Sc+Zr to the Al-Mg-Si casting alloy does not affect the DAS (**Table 5.8**). The average size varies from 10.4 μm in SZ11 alloy to 12.3 μm in the base alloy. These data are in close agreement with those found in literature [34], where the reported DAS is equal to 15μm . It is likely that for grain refinement in eutectic casting alloys higher concentrations of these elements are needed[123]. Consequently it can be deduced that the improvement of the mechanical properties in the investigated alloys cannot be attributed to grain refinement. On the other hand, a decrease in the ILS with the addition of the alloying elements has been observed (**Table 5.8**). The ILS of the Al-Mg_2Si eutectic structure in the base alloy is equal to 0.42μm, which is close to values reported by Shimosaka *et al.*[163] for the HPDC Magsimal-59 alloy. It was also discussed that Al-Mg_2Si eutectic morphology is strongly affected by the cooling rate. In the current study the same casting technique, i.e. the same cooling rate was applied. The addition of Zr does not appear to have a significant effect on the morphology and the mean value of ILS remains in the same range (0.40 μm). The addition of Zr+Cr in CZ11 alloy brings a small

decrease of ILS (0.37 μm). Increasing the Zr and Cr amounts in the CZ12, CZ22 and CZ33 alloys gives a more prominent effect. The strongest effects were observed in the Sc-containing alloys, where ILS is equal to 0.09 μm for the SZ11 alloy. Meanwhile, the average amount of Al+Mg2Si in the middle part of the plate slightly degreases and vice versa in the near edge region (**Figure 5.18 b**).

Mechanical properties

As mentioned earlier, the microstructures of the HPDC Al-Mg-Si alloys consist of the primary α-Al phase, Al–Mg_2Si eutectics and intermetallic phases. It is discussed in the literature that similar concentrations of Cr, Zr and Sc additions have a positive effect on tensile properties (UTS and elongation to failure) in Al-Mg-Si wrought alloys and Al-Mg_2Si composites, mainly due to grain refinement effect [110,127,128,169]. According to the data from this investigation (**Table 5.8**), however, it was found that the all additions do not affect the DAS. 0.2 wt. % additions of Sc or Zr for die cast alloys did, however, lead to significant changes in the shape of the eutectic [76]. On the other hand, as discussed above, a decrease in ILS with the addition of the alloying elements has been observed (**Table 5.8**).

The yield strength (σ_Y) is dependent on the state of microstructure and therefore may be expressed as a function of solid solution, i.e. σ_{SSH}, precipitation strengthening from Mg_2Si, Al_3Sc, Al_3Zr and $Al_3(Sc,Zr)$ particles (dispersoids) (σ_{PH}) and strengthening from changes in lamellar structure (σ_l) to an initial pure aluminum strength (σ_i), as shown in Eq. 5.1:

$$\sigma_y = \sigma_i + \sigma_{SSH} + \sigma_{PH} + \sigma_l \quad (5.1)$$

The greatest effect for solute solution strengthening arises from elements with high solubility in the aluminum. For our system these elements are Mg and Si [170]. Notwithstanding with the small solid solubility of Zr (only 0.28 % at melting point) and Sc (0.31%), it is believed that the contribution to overall strength from these elements is entirely from Al_3Zr and Al_3Sc particles (dispersoids) [13,149]. However, in the Zr- containing alloys no Al_3Zr dispersoids were found. Taking into account that the amount of the main alloying elements (Mg, Si, Mn) is constant, the Eq. 5.1 can be expressed as:

$$\sigma_y = \sigma_{base} + \sigma_{PH} + \sigma_l \quad (5.2)$$

where σ_{base} is the strength of the base alloy.

The strength and ductility in the as-cast state have been compared (**Figure 5.24a-b**). Sc-free alloys (**Figure 5.24a**) show a small increase in yield strength and a much greater increase in tensile stress compared to the base alloy. Furthermore, **Figure 5.24b** shows that the addition of a combination of the elements Zr and Sc to the base Al-Mg-Si-Mn alloy gave both higher strength and an improved ductility. It must be emphasized that the strength increase is obtained simply by adding Sc. Further, it can be seen that the Sc-Zr alloy has a slightly higher yield strength and tensile strength but the same ductility when compared to the Sc containing alloys (**Figure 5.24b**). These alloys with the combine addition of Zr+Sc were designed in order to substitute part of the Sc from Sc-contacting alloys, but retain mechanical properties on the same level or even higher. With regard to the SZ11 and S2 alloys (**Figure 5.24b**), it can be seen that they have almost the same increase in UTS (~15%) and elongation (~22%) when compared to the base alloy. Yield Strengths were increased to 200 MPa and 196 MPa for the SZ11 and S2 alloys respectively. Furthermore, these alloys can form simple $Al_3(Sc,Zr)$ and complex $Al_3(Sc_{1-x},Zr_x)$ precipitates, which can also lead to greater improvements in mechanical properties compared to Al_3Sc particles [135]. The combination of Sc+Zr+Cr (alloy SCZ) does not show significant improvement in tensile properties as compared to the SZ11 and SZ21 alloys.

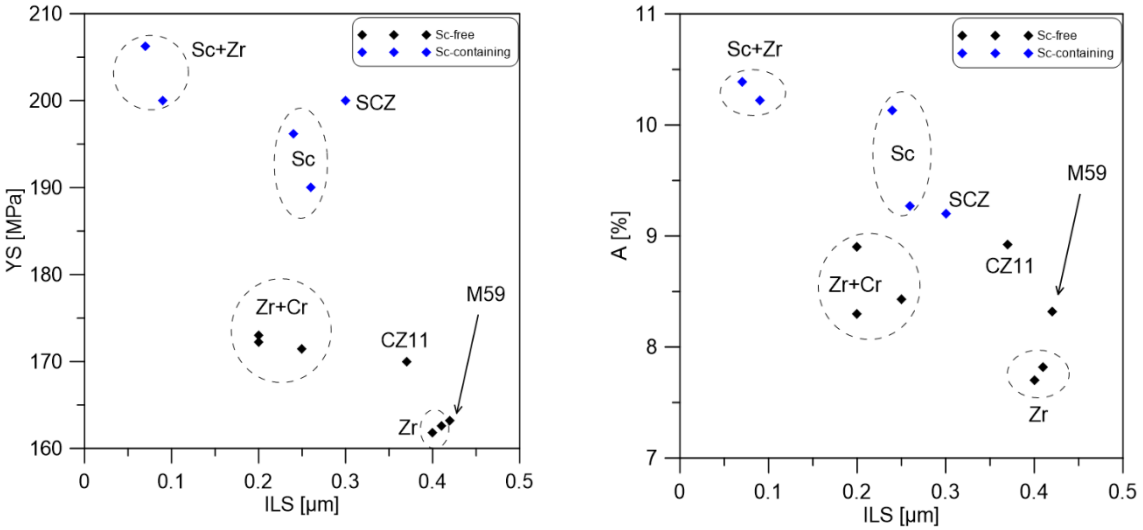

Figure 5.26 Effect of the change in the interlamellar space on the a) yield strength and b) elongation.

In **Figure 5.26a-b** the effect of the ILS on yield strength and elongation to failure is plotted. There is no apparent linear correlation between the ILS and tensile properties. S1 (0.1 wt. % Sc) and S2 (0.2 wt. % Sc) alloys have almost the same ILS as CZ12, CZ22 and CZ33, although the properties of the Sc-containing alloy are significantly higher as compared to the CZ-alloys. As mentioned previously the Al_3Zr and Al_7Cr intermetallic phases can act as a stress concentrators, reducing the yield stress and elongation to fracture. Thus, the total positive effect from the reduction in ILS is less powerful compared to the harmful effect from the intermetallics. The exception is Al_3Sc phase, which interacts with the Al+Mg_2Si eutectic, seemingly, without introducing any additional stress concentration in the alloys. The main contribution to the improvement in tensile properties is through the addition of Sc (**Figure 5.26**) giving rise to precipitation strengthening from Al_3Sc precipitates observed in Sc-containing alloys (**Figure 5.17**). Moreover, Lee *et. al* reported that the ductility of the alloys was determined by the size and volume fraction of defects inside the tensile bar [171]. Thus we can surmise that gas porosity effected the % elongation values for the investigated alloys.

According to the results from the nanohardness measurements the most significant factor affecting the hardness of eutectic cells is a saturation in the concentration of Sc. Thus, the highest values of the hardness of the eutectic cells were observed in the Sc-containing alloys (**Figure 5.20a**). Due to the fact, that the distribution of Sc cannot be absolutely homogenous and Al_3Sc phase was found in the interlamellar space of the S2-alloy (0.2 wt. % Sc), eutectic cells with a higher content of scandium have higher values of hardness and contrariwise. At the same time, Zr and Sc on the nanohardness of a-Al dendrites are also comparable. Within alloys with the same alloying element, the mean nanohardness values of the α-Al dendrites as well as Al+Mg_2Si eutectic are nearly the same. It means, that the lower amount (0.1 wt. %) of alloying elements is sufficient to enrich the solid solution. The excess of alloying elements, which is not solved in the α-Al, leads to the formation of the Al_3Zr and Al_3Sc phases.

The Brinell hardness measurements of the Sc-free alloys show a small deviation, thought to come from the porosity in these alloys caused by non-ideal casting settings. While the microhardness is less affected by the porosity level and showed a continuous increase of hardness with increasing amount of alloying elements. Brinell hardness for the Sc-containing alloys is effectively constant, whereas the microhardness varies slightly. This may be due to the inhomogeneous microsegregation across the α-Al. Nanohardness has no correlation to the amount of alloying element within the same group of alloys but rather indicates an equal hardness range for the alloys with the same alloying additions.

Chapter 6

Mechanical and structural study of the heat-treated state

In the following chapter the results obtained after heat treatment are presented. As was discussed in the Chapter 3, the main challenge was to find the optimal heat treatment modes to promote formation of both Al_3Sc and Mg_2Si precipitates in the investigated alloys. In order to reach this goal, artificial aging from the as-cast state under low and high temperatures, which leads to precipitation formation was performed. In the sub-chapter 6.2, results, obtained after T6 regime, which is used for Al-Mg-Si wrought alloys due to a good response on the mechanical properties, will be used for the investigated Sc-free and Sc-containing HPDC alloys.

6.1 Aging from the as-cast state, T5 regime

Hardness measurements

The artificial ageing behaviour at temperatures between 125-325°C was studied by HVtesting. **Figure 6.1a-d** shows the hardness after artificial aging (AA) of the Sc-free and Sc-containing alloys for the various times in order to find the optimal regime for further HT of the TT samples.

All of the alloys studied show approximately similar values of hardness after aging at temperatures in the range 125-225ºC (**Figure 6.1a-c and A.1**). The maximum hardness value of 105 $HV_{0.05}$ was reached after 3 hours of AA at 225ºC. For low temperature aging the average hardness was around 100 $HV_{0.05}$ for all investigated alloys. The most noticeable changes were recorded at the aging temperature of 325ºC and over the period of 1-3 hours (**Figure 6.1d**). In the range of 2-6 hours a hardness plateau was observed. With long term AA (12 hours) a small decrease in hardness values was detected. The maximum increase in hardness for the Sc-free alloys is only 6-7% (in Z2 alloy), whereas for the Sc-containing alloys an increase in hardness of 30% was achieved for S2 alloy, after 2 hours of AA. The hardness values of the S2 alloy (with 0.2 wt. % of Sc) reach around 120 $HV_{0.05}$. The overall increase in hardness for the Sc-containing alloys are in the region of 16% for the S1 alloy and 25% for the rest of alloys.

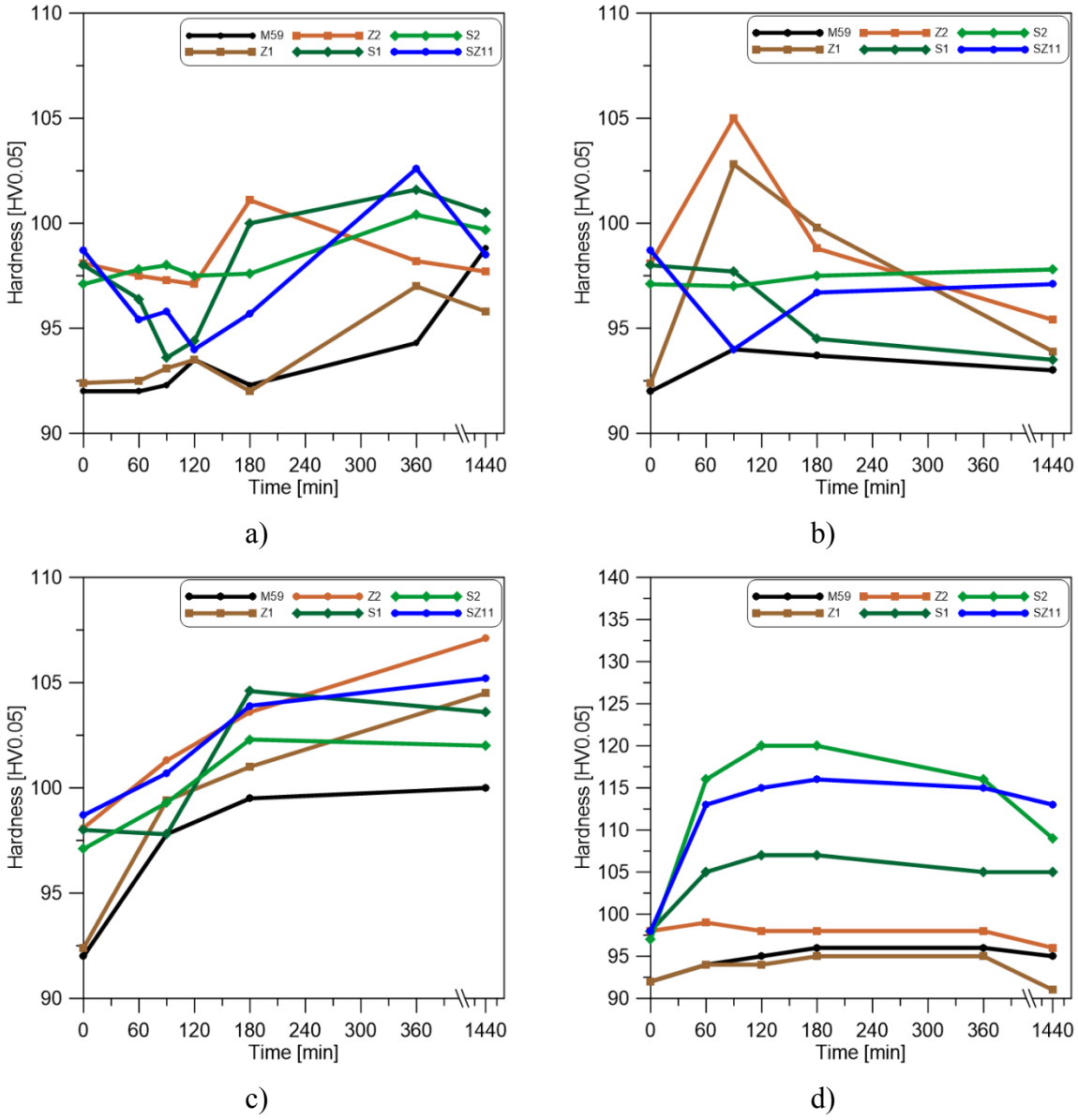

Figure 6.1 Microhardness as a function of a time at a) 125, b) 175, c) 225 and d) 325°C.

Tensile test, T5 regime at 225 and 325 °C

Figure 6.2 a-b represents the results of tensile tests of M59 (base alloy), Z2 and S2 alloys for different aging temperatures. The duration for artificial aging was chosen from **Figure 6.1**, giving a time of hours for peak hardness values (3 h). The base alloy as well as Z2 alloy show similar trends during the artificial aging treatment. The maximum values of both strength (ultimate tensile stress and yield stress) were achieved the aging temperature of 175 ºC, which also produced the lowest values of elongation to failure for those alloys. While increases of artificial aging temperature have little effect on UTS, YS and ductility tend to decrease. At the maximum aging temperature, elongation values for the M59 and Z2 alloys are similar to those in as-cast state. The S2 alloy (0.2 wt. % Sc) shows the highest values of the tensile and yield strength at 325ºC. Within the temperature range 125- 225ºC both tensile and yield strength are more or less constant. At the same time elongation decrease with increasing artificial aging temperature (starting at 175 ºC). The artificial aging at temperatures up to 325ºC does not lead to any structural changes (**A.1**). The morphology of the existing phases remains the same [SC3[1]].

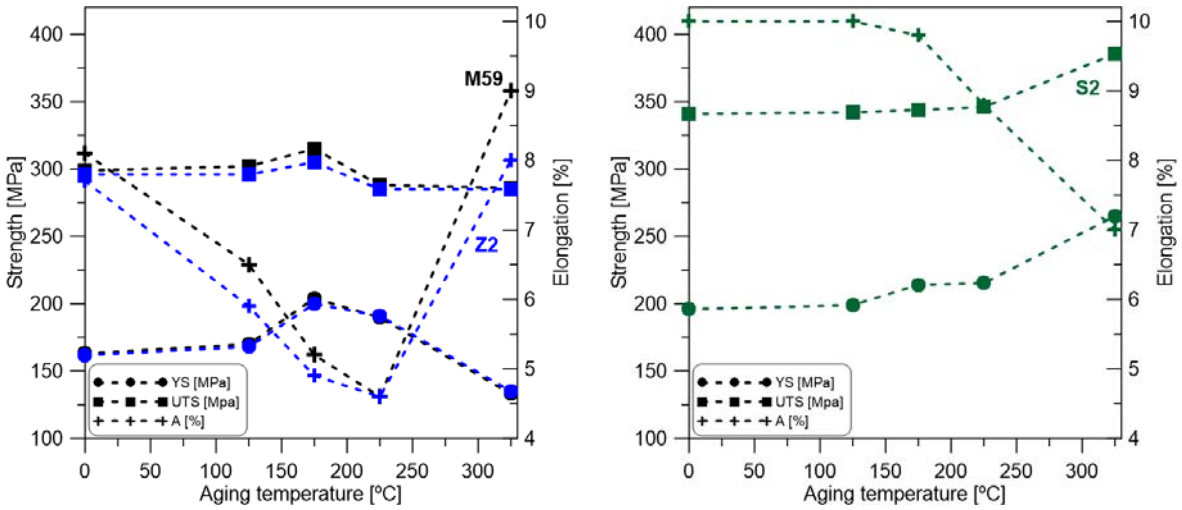

Figure 6.2 Tensile properties of the a) base alloy (black line) and Z2 (blue line), b) S2 (green line) as a function of aging temperature for 3hours.

[1] O. Trudonoshyn, O. Prach, P. Randelzhofer, K. Durst, C. Körner „ Heat treatment of the new high-strength high-ductility Al-Mg-Si-Mn alloys with addition of Scandium, Zirconium and Chromium “. Paper is going to be submitted

The tensile properties, as a function of aging time, after AA at 325°C are shown in **Figure 6.3.** The temperature of 325°C, at which the highest hardness values were obtained, was chosen (**Figure 6.1)** and as S2 alloy shows the highest values of the both tensile and yield strength, whereas M59 and Z2 show the highest values of elongation. The maximum values of strength (UTS and YS) for all investigated alloys were obtained after three hours of artificial aging. However, this peak in strength is more prominent for the Sc-containing and the CZ22 alloy. For the rest of the Sc-free alloys these values are independent from the artificial aging time. Alloys with the 0.1wt. % of Sc (S1 and SZ11) show similar values of tensile and yield strength. The same trend was observed for the alloys with the 0.2wt. % of Sc (S2 and SZ21). The yield strength of the Sc-free alloys is in the range of 133MPa (M59) and 148MPa (Z-series and CZ-series alloys). With regard to tensile strength the values are not so grouped and the difference between CZ11 and S1 alloy is small with corresponding curves close to each other. The values of elongation to failure do not follow the same trend as tensile or yield strength. However, for all investigated alloys the maximum values were found at the longest artificial aging time of 15 hours.

The tensile properties (yield stress, ultimate tensile stress and elongation to failure) with different temperatures and the aging time to peak hardness (3 h) are plotted as a function of alloying element and are presented in **Figure 6.4**. The results show that yield stress is not affected by the aging temperature at 225°C, as the maximum increase for the Sc-containing alloys is only around 10%, compared to the base alloy (**Figure 6.4 a)**. The yield strength values for the Sc-free alloys are in the same range as for the base alloy. The tensile strength for the Sc-free alloys increases by 3%. Alloys with the single addition of Sc (S1 and S2) together with those having a combined addition of Sc+Zr (SZ11 and SZ21) show a more pronounced increase in strength. With an increase of 91% the tensile strength of the S2 alloy was almost doubled, while the lowest increase of 62% was recorded for the SZ11 alloy. Along with strength, ductility was also increased, with amounts varying from 4.6% (M59 alloy) to around 8.1% (S2 alloy). The Sc-free alloys did not show the same spectacular results. The Z1 and Z2 alloys have the same results like the base alloy. CZ11 and CZ12 showed an improvement by 28% and 48% respectively. However, after an increase of the number of alloying elements (CZ22 and CZ33 alloys), the obtained results are the same, likewise to the base alloy.

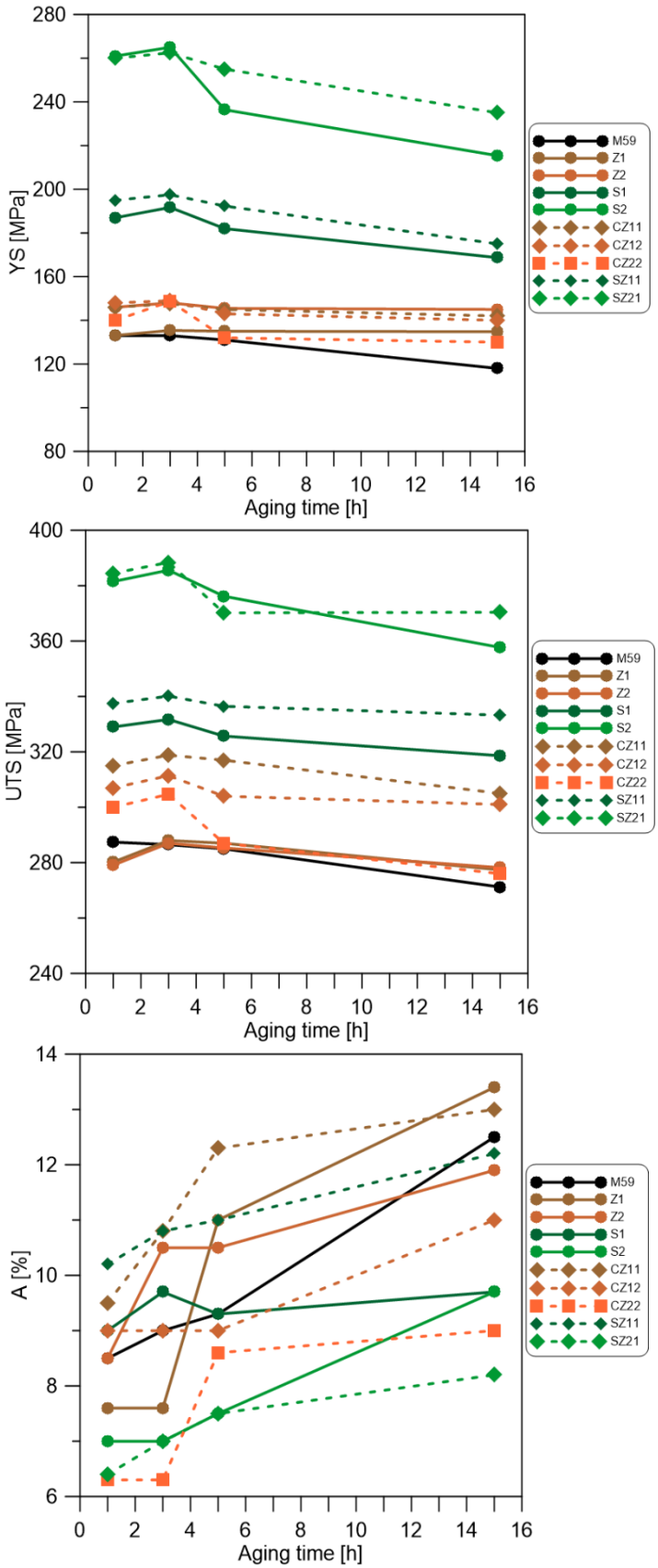

Figure 6.3 Tensile properties as a function of aging time after AA at 325°C.

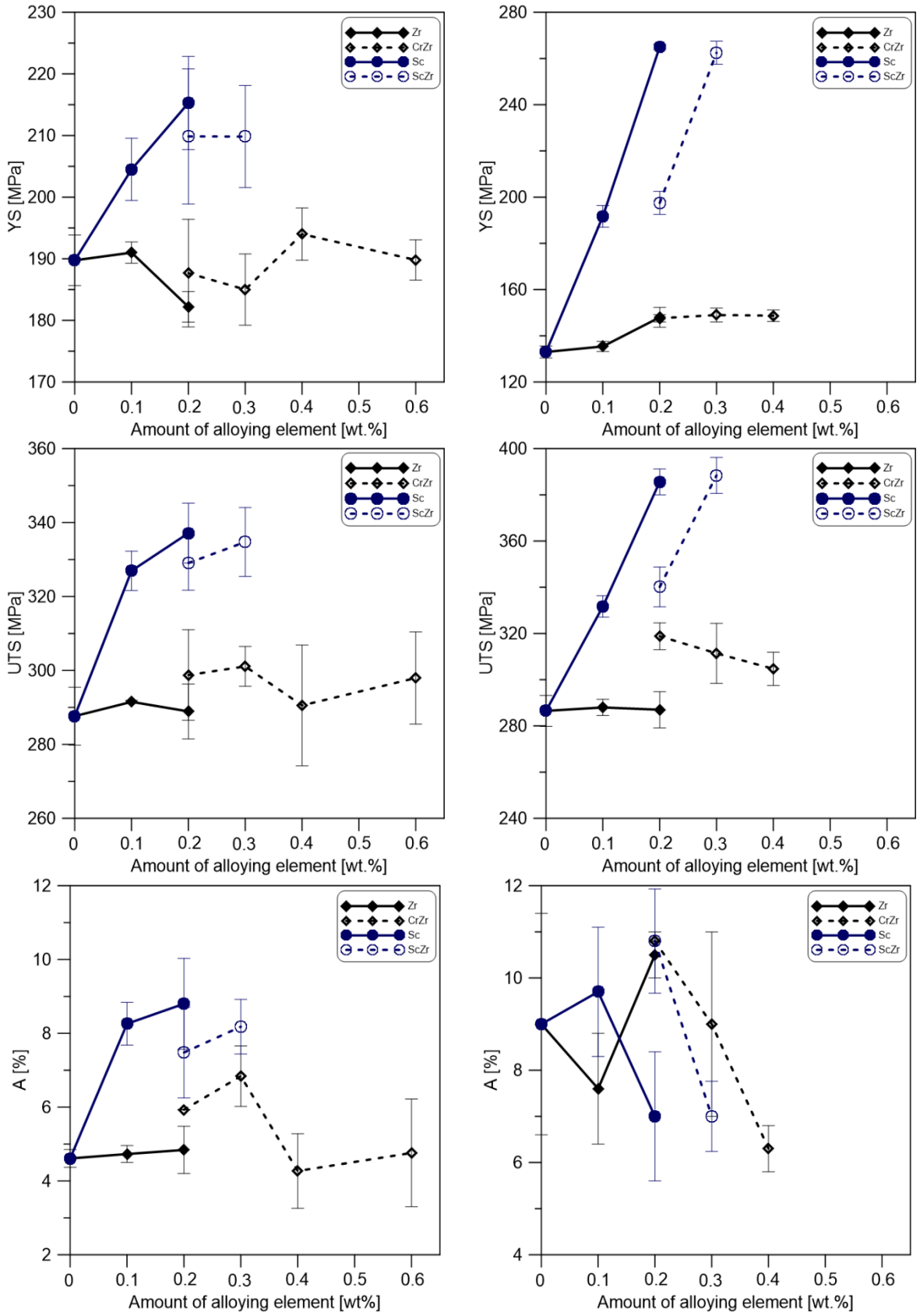

Figure 6.4 Tensile properties as a function of chemical composition after 3 hours of AA

Artificial aging at a high temperature (325°C) led to more prominent changes in both yield and ultimate tensile strength (**Figure 6.4 b)**. All Sc-free alloys (except Z1) showed a 10% increase in yield strength. The tensile test results for S1 and SZ11 alloys are similar and show improvements in yield strength of 45% while S2 and SZ21 doubled their initial values. The same trend is observed in the results for the tensile strength. Z1 and Z2 alloys, however, showed the same values of UTS as the base alloy. The CZ11 alloy showed an 11% increase in UTS. Increasing the number of alloying element has an apparent tendency to result in a reduction in tensile strength after heat treatment. It should be mentioned that values obtained from the CZ22 alloys are still higher compared to the base and Zr-containing alloys. The most ambiguous results were obtained from the elongation to failure data. Alloys with a single addition showed contradictory results to each other, while those with a combined addition generally showed a tendency for reductions in % elongation with increasing wt. % of the alloying elements.

Figure 6.5 represents results of tensile tests of alloys with the single addition of Zr and Sc as well as alloys with combined additions as a function of artificial aging temperature (3hours of AA). Comparing these results it should be mentioned that all investigated alloys have a similar response to the temperature change of AA. The most significant response was observed for the alloys with 0.2 wt. % Sc (S2 and SZ21) with yield strength and ultimate tensile strength increasing by 132 MPa for both alloys (**Figure 6.5 a-b**). However, elongation to failure has an opposite tendency (**Figure 6.5 e-f**) and a small decrease was observed for the S2 and SZ21 alloy after the heat treatment at 325°C. Any response of the S1 and SZ11 alloys to the temperature increase was negligible. The yield and ultimate tensile strengths did not change for these alloy (**Figure 6.5 a-b**) although values of elongation to failure increased sligtly with increasing AA temperature (**Figure 6.5 e-f**). The base alloy and Sc-free alloys showed a different trend; with yield strength markedly decreasing as AA temperature was increased. The UTS of the base alloy and for Z1, Z2 alloys did not change, whereas alloys from the CZ-series showed slight increases in UTS with the temperature increase. For all Sc-free alloys an increase in elongation with increasing AA temperature was observed (**Figure 6.5 e-f**).

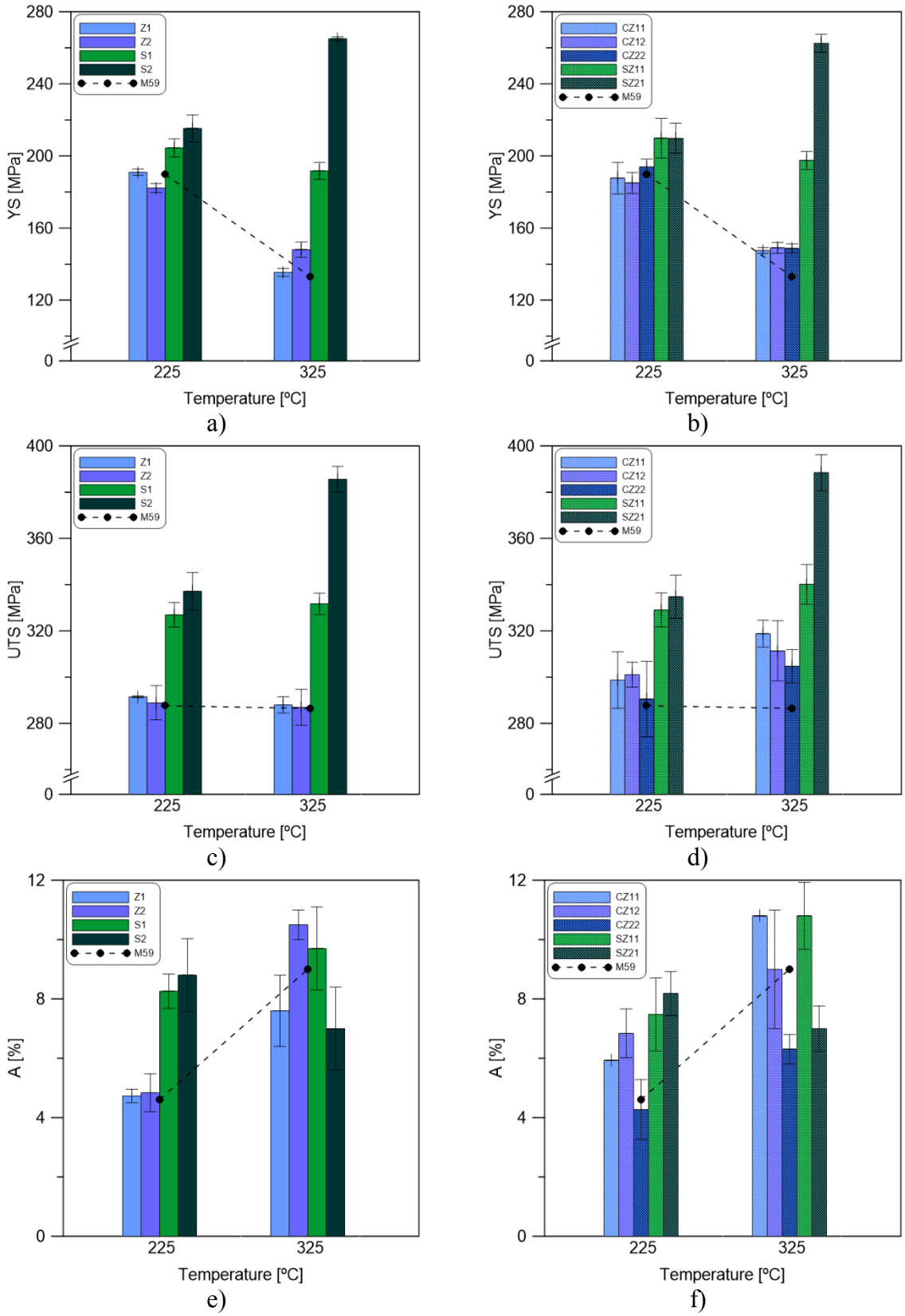

Figure 6.5 Tensile properties as a function of artificial aging for 3 hours at 225°C and 325°C a-b) yield stress, c-d) ultimate tensile stress and e-f) elongation to failure.

In **Figure 6.6** TEM images, taken along the ⟨001⟩$_{Al}$ axis, are shown [SC3[21]]. The structure of the α-Al dendrites aged at 175 ºC and 325 ºC is the same as in the as-cast state and consists of β'and stable β phases.

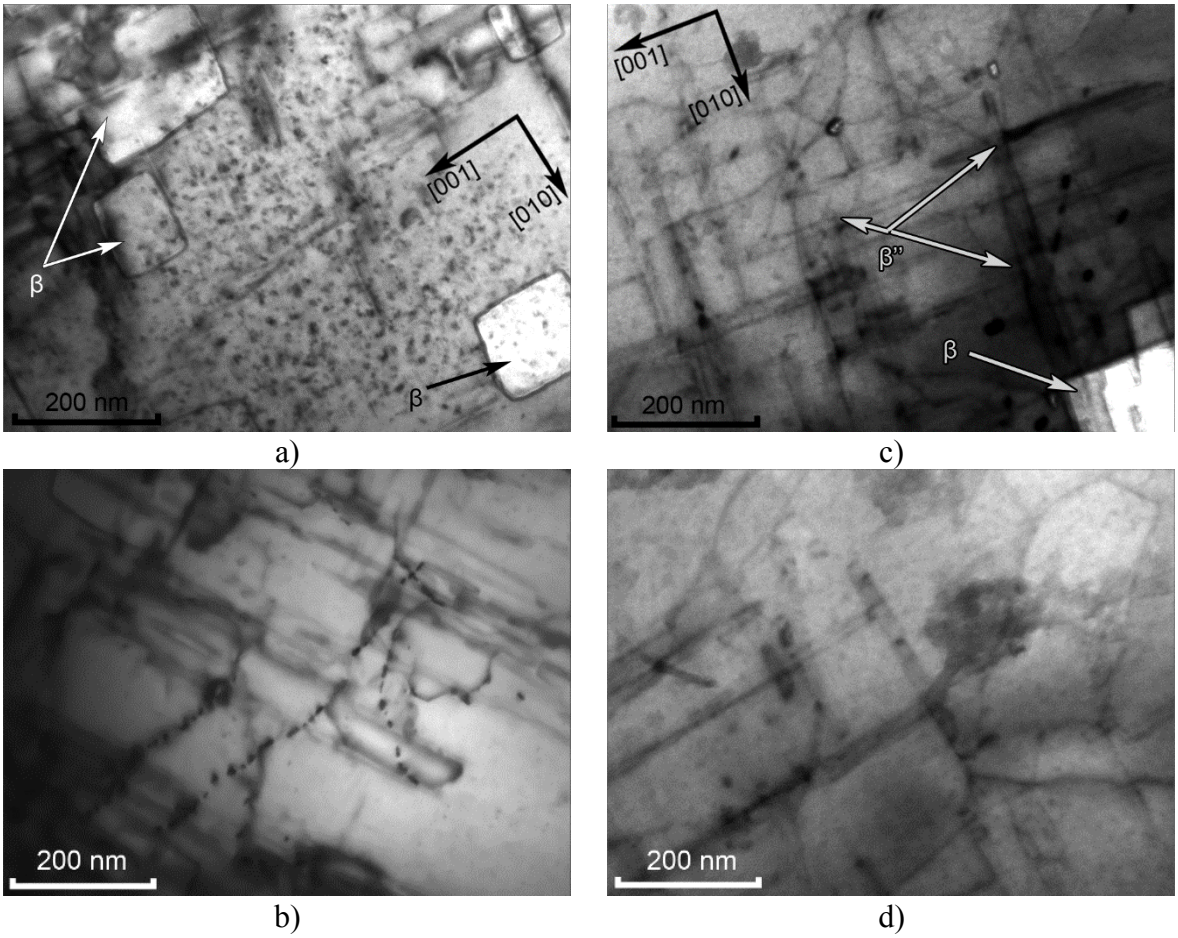

Figure 6.6 TEM bright-field images of the M59 alloy after artificial aging a-b) at 175ºC; c-d) at 325ºC

[1] O. Trudonoshyn, O. Prach, P. Randelzhofer, K. Durst, C. Körner „ Heat treatment of the new high-strength high-ductility Al-Mg-Si-Mn alloys with addition of Scandium, Zirconium and Chromium ". Paper is under review. Available online [172].

Figure 6.7 represents the TEM images of the S1 and S2 alloys after artificial aging [SC3[31]]. In these alloys, after aging at 225ºC, approximately spheroidal and/or coffee-bean shaped Al_3Sc precipitates, uniformly distributed throughout the matrix were observed (**Figure 6.7 a** and **c**). With the aging temperature increased up to 325ºC (**Figure 6.7 c** and **d**), Al_3Sc precipitates in S1 and S2 alloys appear in greater numbers and density. The average precipitate radius is larger for the S2 alloy at 325ºC than for the S1 alloy.

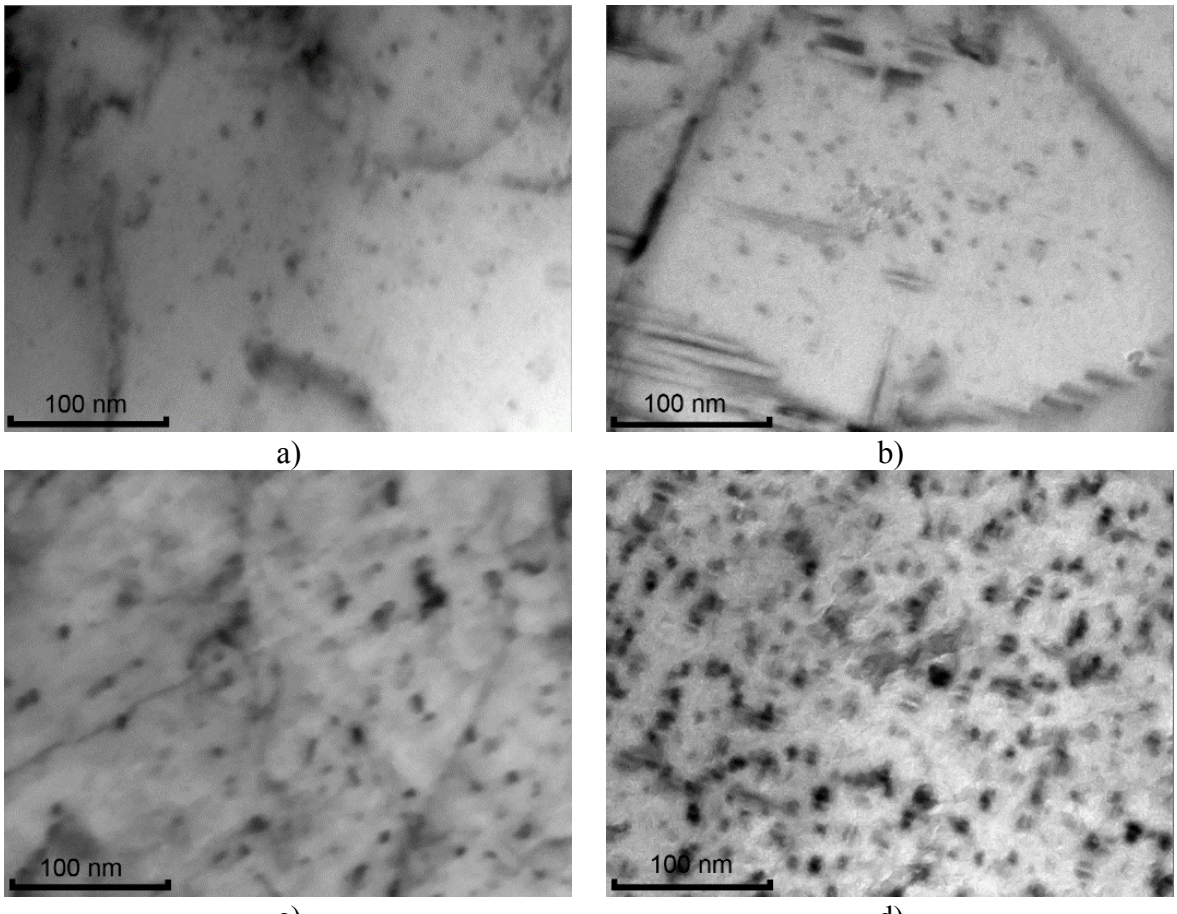

Figure 6.7 TEM bright-field images of the Sc-containing alloys after artificial aging: a) S1 after 225ºC, b) S1 325ºC, c) S2 225ºC, d) S2 325ºC

[1] O. Trudonoshyn, O. Prach, P. Randelzhofer, K. Durst, C. Körner „ Heat treatment of the new high-strength high-ductility Al-Mg-Si-Mn alloys with addition of Scandium, Zirconium and Chromium “. Paper is under review. Available online [172].

6.2 T6 regime and outgassing

Outgasing

Figure 6.8 a shows the results of hardness measurements across the plate after T6 heat treatment at different temperatures of the ST for the base alloy and after artificial aging only. The maximum hardness of 120HV was observed in the sample after T6 regime (ST at 570°C+AA at 175°C). The hardness values of the samples treated at lower temperatures of ST, however, were lower than those measured in the as-cast state. The sample after artificial aging (T5 regime, dark blue dots) shows hardness values comparable to the alloy after T6 regime with the maximum hardness.

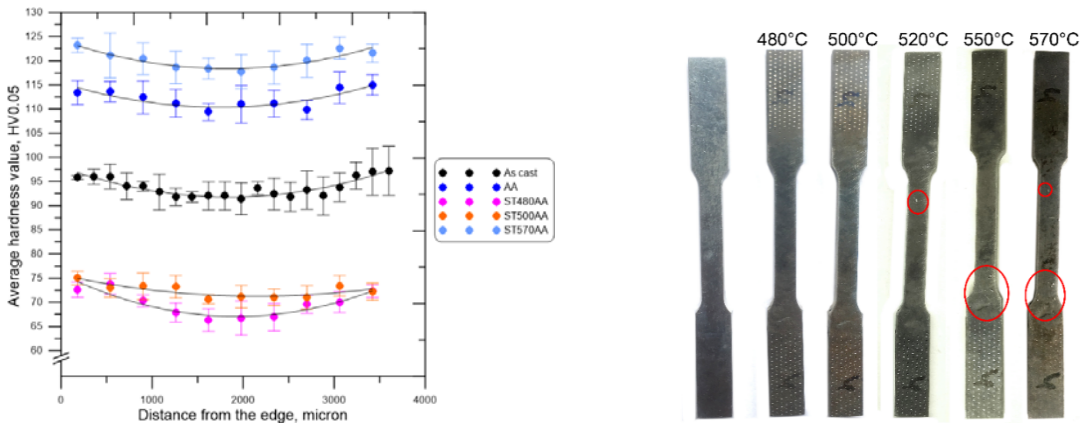

a) b)

Figure 6.8 a) Hardness across the plate after the heat treatment and as-cast state. AA at 175°C (24 hours) and b) surface tensile samples of the base alloy and after different solution-treatment schedules.

In **Figure 6.8 b** a comparison for the base alloy between an as-cast specimen and specimens after HT is shown. The sample was heat treated step by step using conventional solution treatment cycles, the starting temperature of ST was 480°C and the maximum temperature was 570°C. Up to 500°C the sample had not shown any visible surface changes, whereas after rising the temperature of the solution treatment to 520°C and higher, surface defects (marked with red circles) were observed. This treatment resulted in severe surface blistering together with noticeable distortion in the transverse direction.

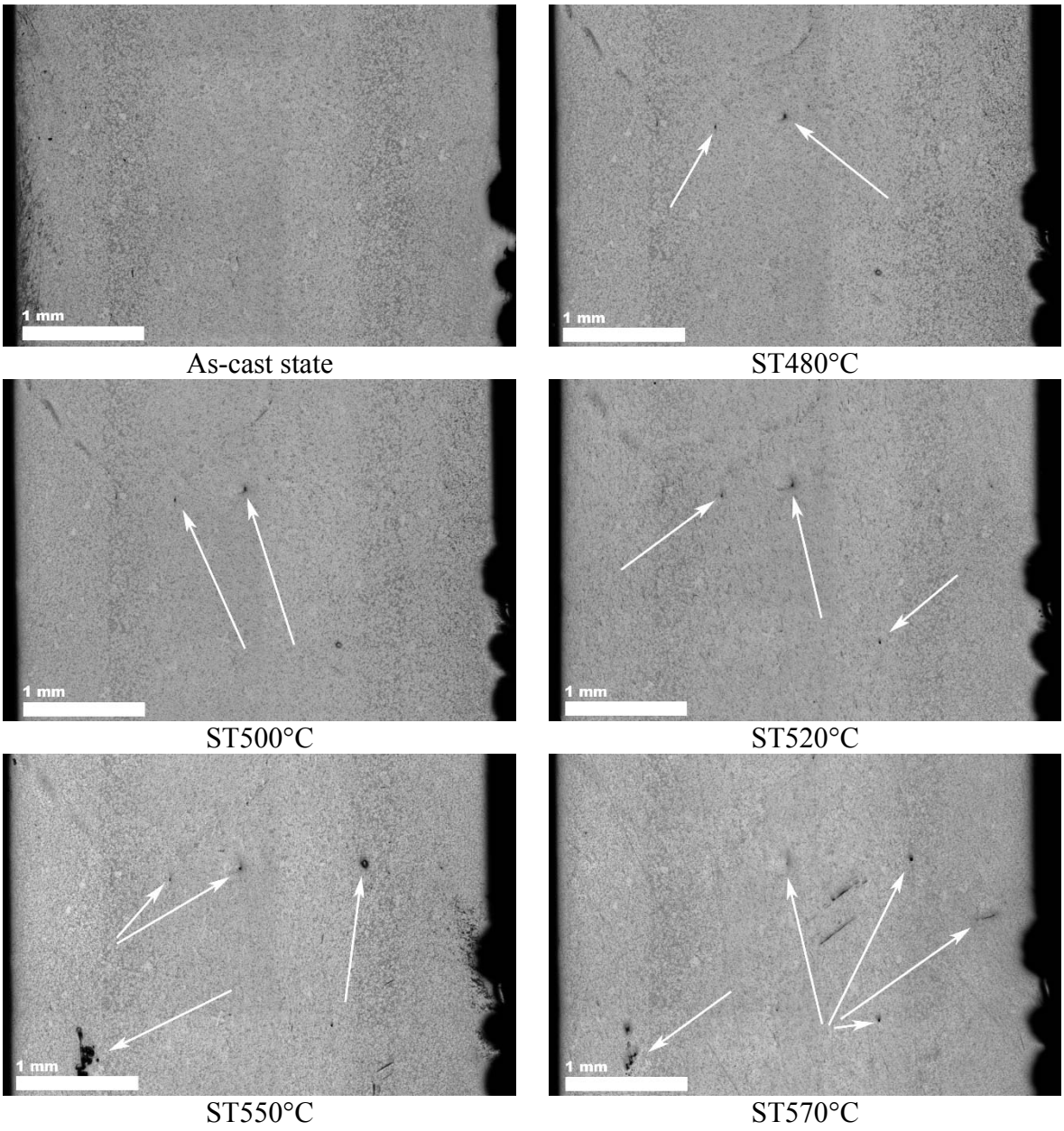

Figure 6.9 Structure after solution treatment at different temperatures during 1h [172].

Figure 6.9 shows the microstructures corresponding to the conditions shown in **Figure 6.8 b**. It is obvious, that the presence of pores corresponds closely to the surface appearance of the samples. An examination of ST temperatures at the same time shows that blisters could be observed at 520°C. Nevertheless, it appears the most crucial point for the material may be due to holding at temperatures close to ST550°C and higher. During the artificial aging no blistering occurs.

T6 regime

The samples of the base alloy were heated to temperatures of 480°C and 570°C over various periods, before being quenched in cold water, and subsequently aged at 175°C. The hardness measurements were used to monitor responses to time and solution treatment temperatures as well as aging. As shown in **Figure 6.10 a-b**, it was found that the levels of hardening after quenching and aging were all relatively high, compared to the low temperature solution treatment. After a conventional T6 solution treatment schedule during various times of ST and AA no significant changes in the hardness were observed. In all cases the hardness significantly increased following a drop in hardness after single ST and stayed more or less constant with increasing AA time. An opposite effect was observed after the low temperature solution treatment (**Figure 6.10 b)**, following which hardness values barely reached those found in the as-cast state.

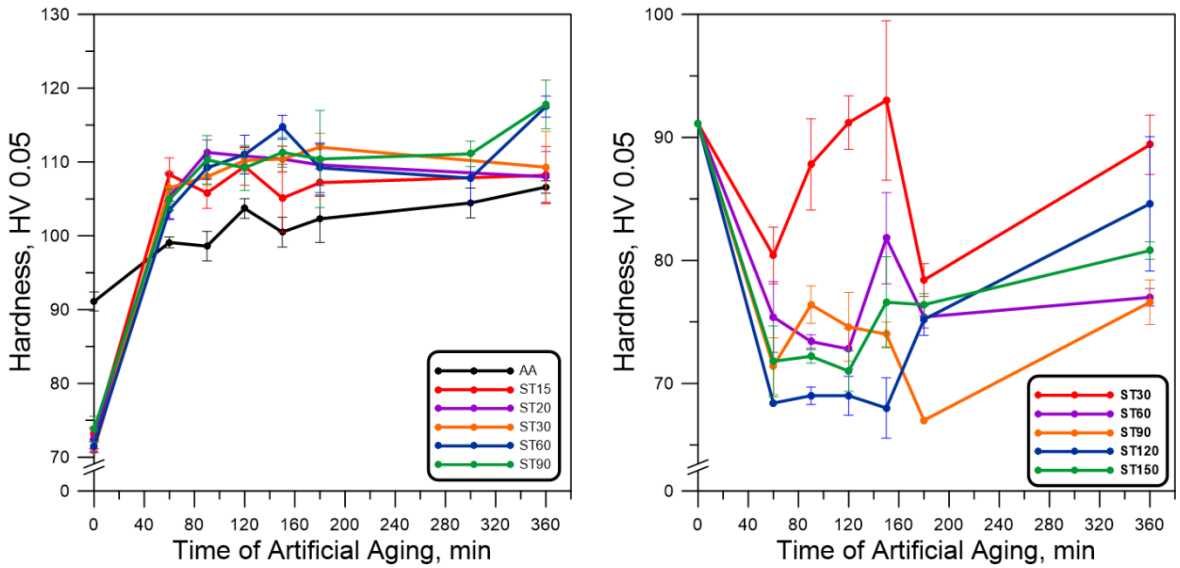

a) ST570+175AA b) ST480+175AA

Figure 6.10 Hardness-time curves for the base alloy aged at 175°C following the solution treatment procedures at 570 and 480°C. The black curve represents results after AA directly from as-cast state.

A significant reduction in hardness after ST is caused by the changes of the structure of Al-Mg-Si-Mn alloys during the heat treatment. At a such a high temperature spheroidization of eutectic took place (**Figure 6.11a-d**). High ST temperatures lead to the decomposition of the needle-shaped eutectic cells into separate Mg_2Si particles. A structural changes in the temperature range of 480-570°C have not been detected. Thus, at this point, the investigated

alloy does not have any strengthening effect from the Al–Mg_2Si eutectic and none of nanosize precipitates have been formed yet. In **Figure 6.10a** a strong reduction in hardness values (down to 70HV) after ST at various times is shown. However, at such a high ST temperature the Al_3Zr, Al_3Sc and Al_7Cr intermetallic phases are not affected (**Figure 6.12**). These intermetallics are not dissolved in the α-Al and do not change shape.

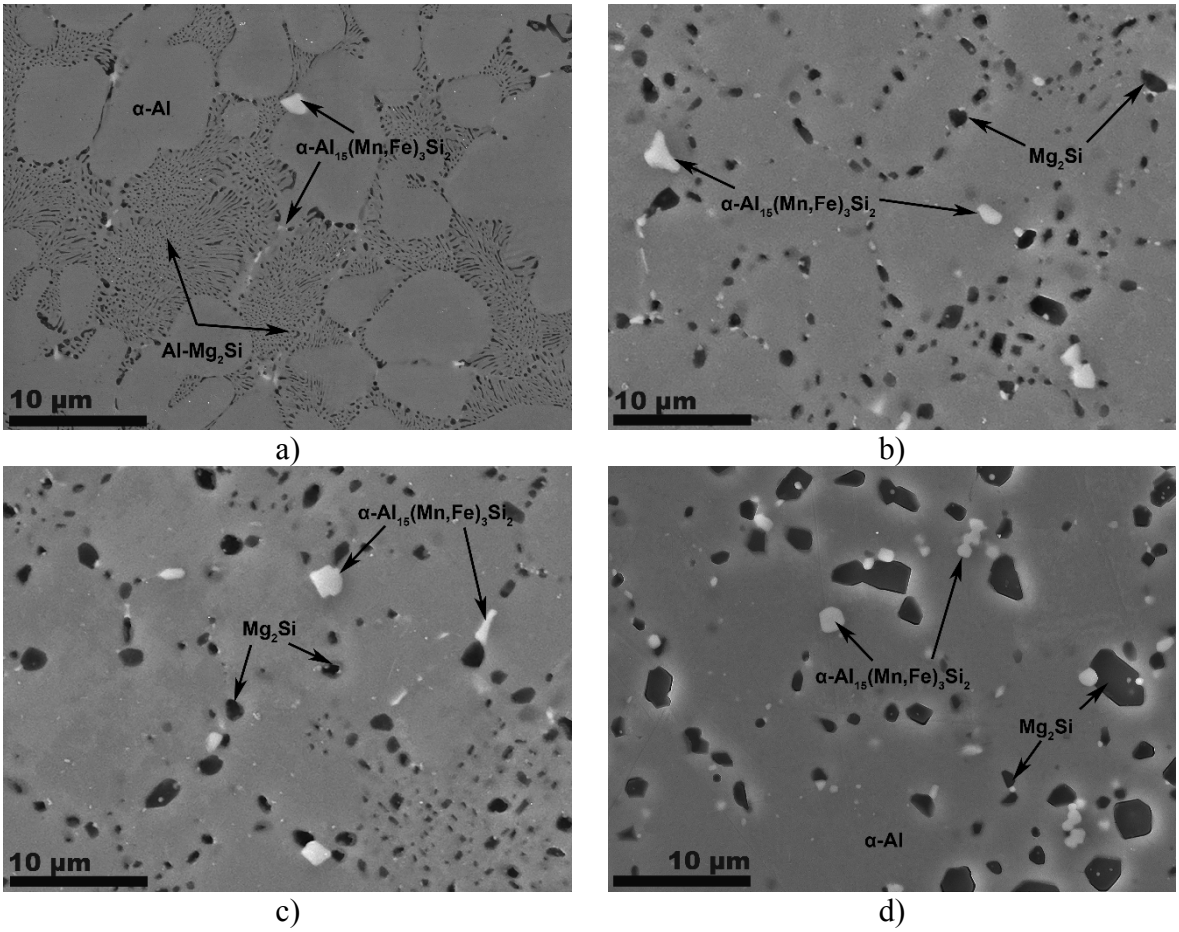

Figure 6.11 Microstructure of the M59 alloy in a) as-cast state and after solution treatment at b) 480°C, c) 520°C, d) 570°C.

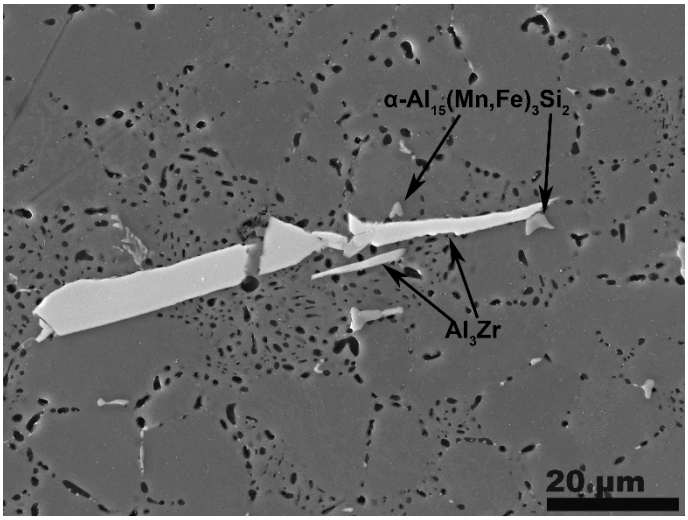

a)

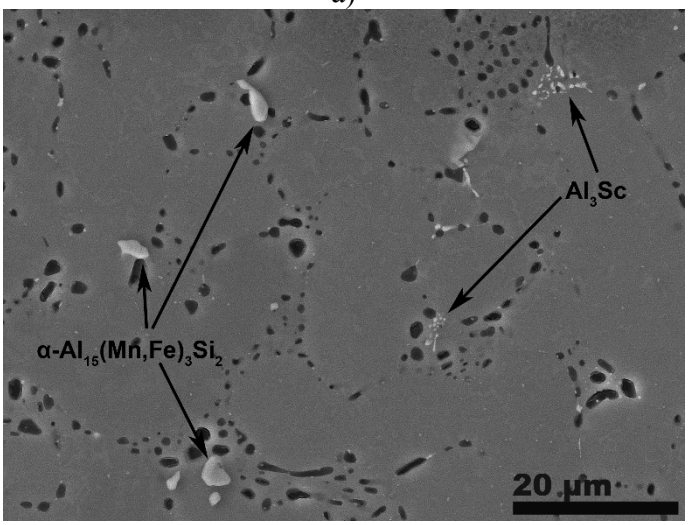

b)

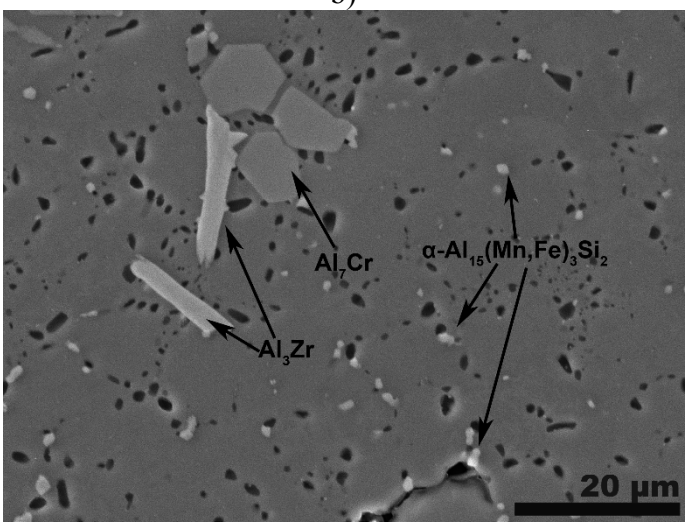

c)

Figure 6.12 SEM images of the a) Z2, b) S2 and c) CZ33 alloys after ST at 520°C during 3h [172].

The comparative tensile curves for the base alloy (M59) and S2 (0.2 wt. % Sc) alloy after T6 (ST570°C+AA175°C) condition are given in **Figure 6.13**. The T6 regime affects mainly the proof stress. The average value is equal to 200 MPa for the M59 alloy and 220 MPa for the S2 alloy.

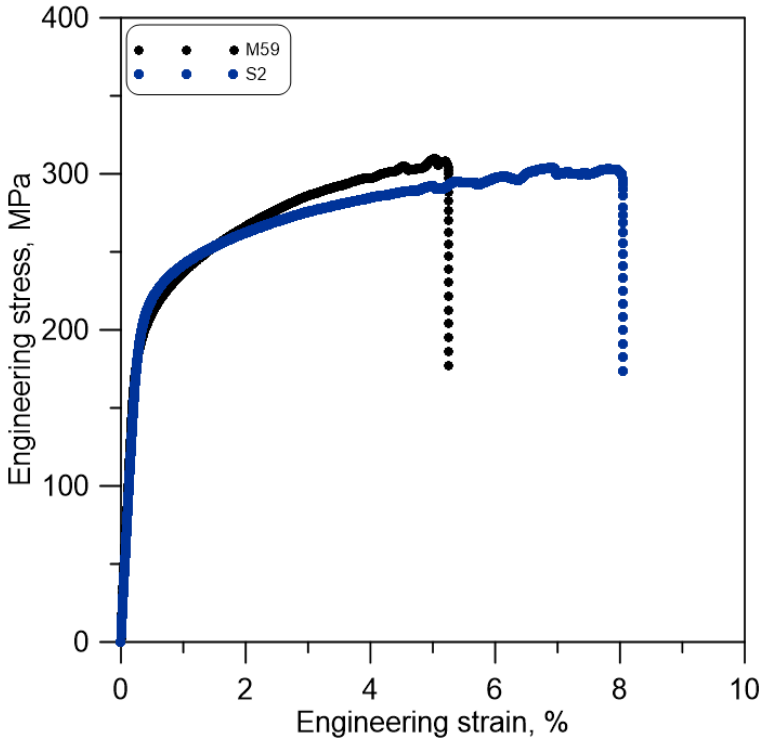

Figure 6.13 Stress-strain curves for the base and S2 alloys after high temperature T6 regime (ST570°C+AA175°C).

The results from the tensile tests after solution treatment at 520°C and artificial aging at 225°C and 325°C are given in **Figure 6.14**. The alloys with the single addition of Sc and Zr showed more prominent results after the artificial aging at 225°C. Moreover, the Zr-alloys gave a better response to the low aging temperatures than the Sc-alloys. The yield strength of the M59 alloy is 130MPa, whereas after 325°C this was reduced significantly, to 100MPa. In the alloys with the maximum single additions of the Zr and Sc (Z2 and S2 alloys) the yield strength is equal to the 155.8±5.2 MPa and 138.5±4MPa respectively. The yield strength of the Zr- and Sc-alloys did not show any significant changes. The yield strength of the Z2 alloy has reached a similar level to that of S2 alloy after 325°C.

An addition of Zr and Zr+Cr resulted in a negligible increase up to 172 MPa for the CZ33 alloy (0.6 wt. % of alloying elements), compared to the base alloy yield strength of 163 MPa.

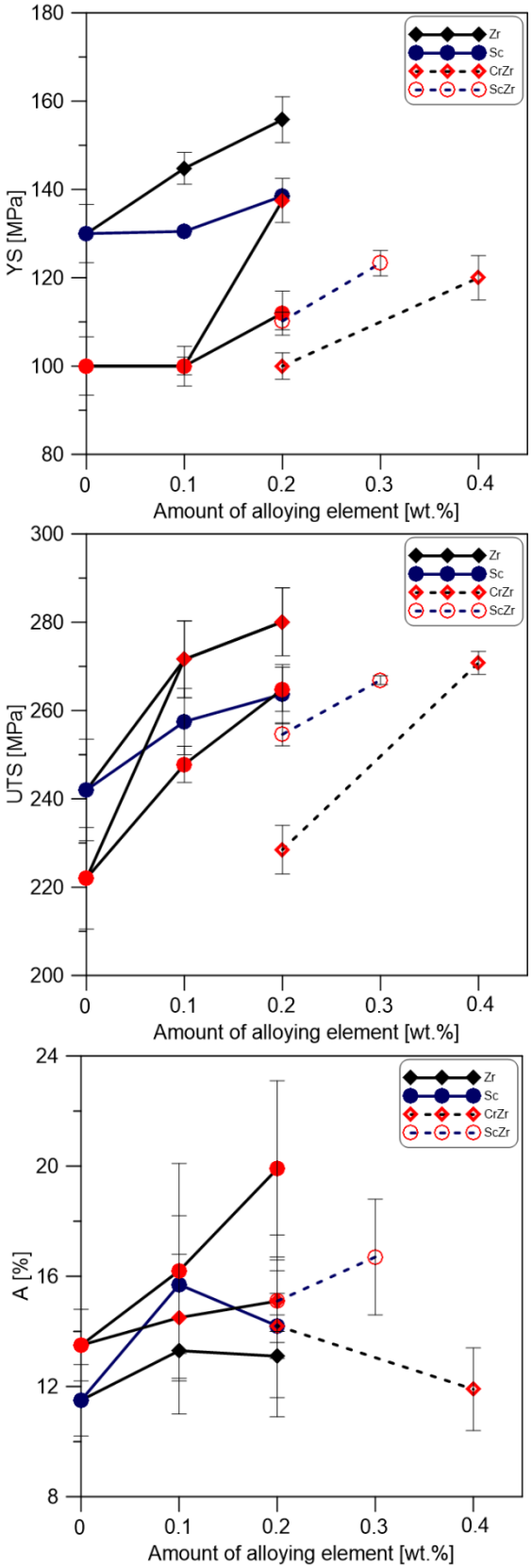

Figure 6.14 Tensile properties as a function of chemical composition after ST520+AA225 and ST520+AA325 (marked with red symbols).

TEM investigation

The solution treatment leads to the dissolving of the strengthening GP-zones, β' precipitates [SC3[41]]. Only an equilibrium β-Mg_2Si phase was observed in the α-Al matrix (**Figure 6.13 a-b**). Along with the dissolving of the strengthening phases, Mn-containing dispersoids are generated. In **Figure 6.13 b-d** Mn-containing dispersoids, which were formed during ST, are shown. It should be noted that these dispersoids, surrounding the Mg_2Si particles, which have a spherical shape after the ST are an equilibrium β-Mg_2Si phase.

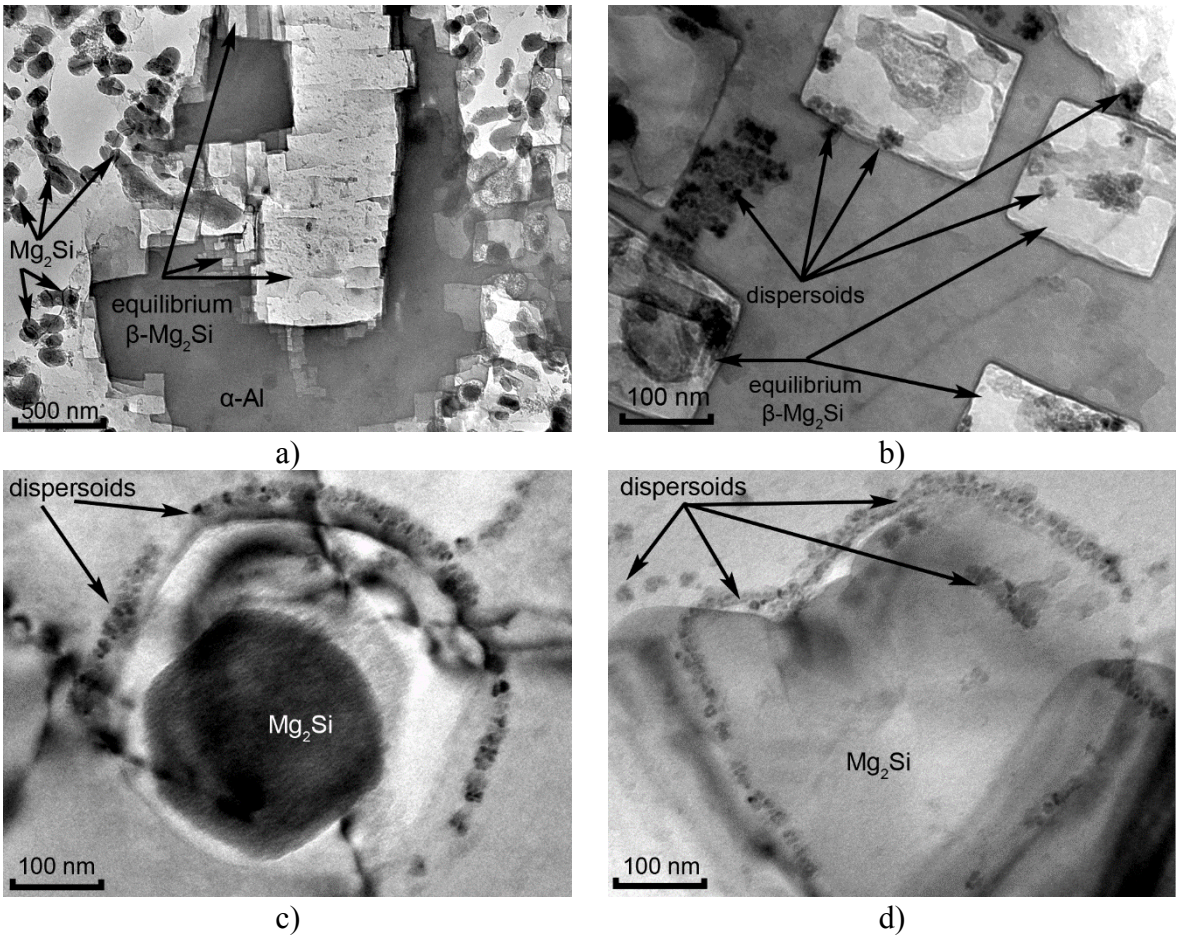

Figure 6.15 TEM bright-field images taken along $\langle 001 \rangle_{Al}$ axis of the M59 alloy after the solution treatment without aging at a-b) 520 ºC and c-d) 570ºC*.

[1] O. Trudonoshyn, O. Prach, P. Randelzhofer, K. Durst, C. Körner „ Heat treatment of the new high-strength high-ductility Al-Mg-Si-Mn alloys with addition of Scandium, Zirconium and Chromium ". Paper is under review. Available online [172].

* TEM have been performed at the Friedrich-Alexander-Universität Erlangen-Nürnberg (FAU), Material Science Department (WTM), Erlangen Germany

Figure 6.16 represents the bright field TEM micrographs, taken along the $\langle 001 \rangle_{Al}$ axis, showing the Al_3Zr dispersoids in the Z2 (0.2 wt. % Zr), processed by the HPDC, after ST 520ºC for 1.5h.

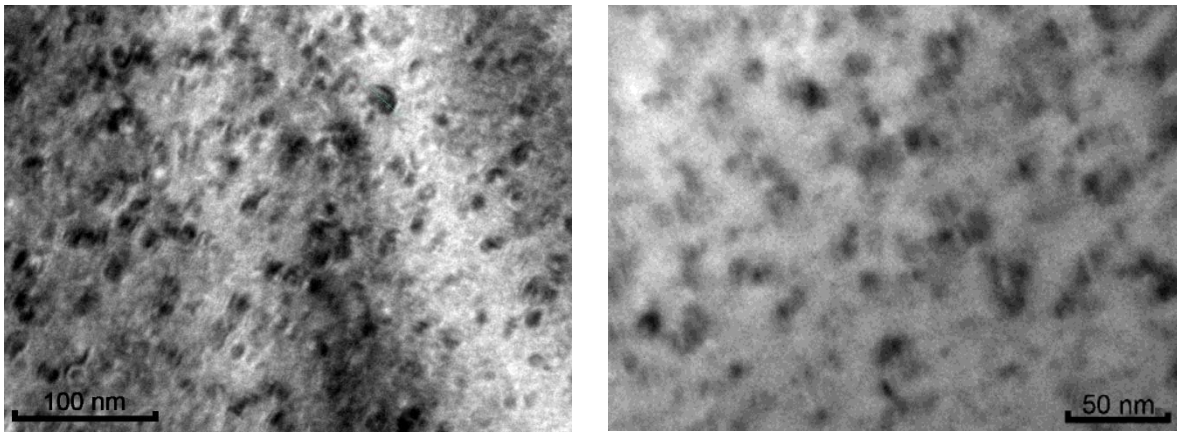

Figure 6.16 TEM bright-field images taken along $\langle 001 \rangle_{Al}$ axis showing the Al_3Zr dispersoids in Z2 alloy after solution treatment Z2 alloy at 520ºC during 1.5h

6.3 Discussion of experimental results after heat treatment

Microstructure

The only one expected change in the microstructure was observed for samples after solution treatment (**Figure 6.11**) where high temperatures lead to eutectic spheroidization. The same trend has been observed by Lee *et al.* for the AlMg5Si2Mn HPDC alloy [171]. **Figure 6.17** shows the changes in the microstructure along with the 3D modelling of the Mg_2Si disintegration in the interior of the same alloy volume. It was also found that total volume fraction of the Mg_2Si particles within the same volume decreases during the homogenization process. Thus, the process of the disintegration of the main strengthening phase in the Al-Mg-Si alloys clearly leads to the decreases in hardness, tensile strength and, consequently the increase in elongation to failure [81,171]. Furthermore, artificial aging leads to the formation of the strengthening Mg_2Si precipitates and as a resulting increase in strength. Further effects of the T6 regime will be discussed later.

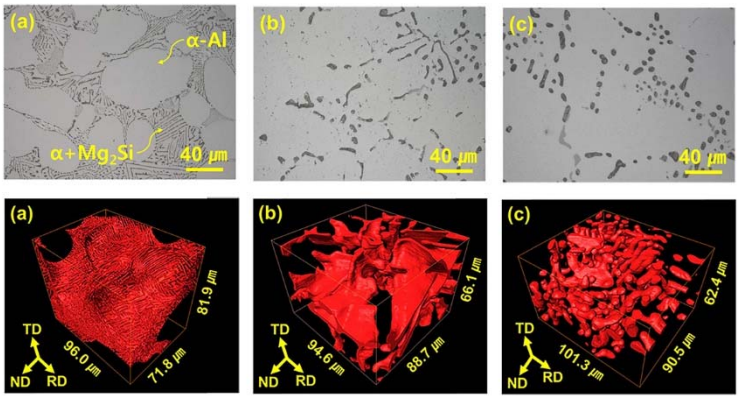

Figure 6.17 Microstructure of the AlMg5Si2Mn HPDC alloy and 3D modelling of theMg_2Si eutectic in the a)as-cast and b,c) heat-treated state. From [171]

Artificial aging from the as-cast state

It was found [68,173] that the optimal temperature for AA of Al-Mg-Si alloys is around 175°C±10°C with the peak hardness after 3h. Further treatment even at those low temperatures can lead to the overaging of the material and consequently the reduction in hardness. In **Figure 6.1** (and **A.4**) hardness values for all investigated alloys are shown. In the case of a low temperature treatment (125°C) no difference either for Sc-free or the Sc-containing alloys can be established. For the most of the alloys the peak hardness occurs between 3 and 6 hours of the AA treatment followed by the reduction in hardness. However, for the base alloy (M59) the maximum is shifted up to 12 hours of treatment. As anticipated, the Sc-free alloys showed a good response to AA up to a temperature of 225°C, whereas Sc-containing alloys had a better response to the temperature of 325°C (**Figure 6.1**). However, Sc-free and Sc-containing alloys had a relatively good response to the treatment at 225°C.

The tensile properties of the Sc-free alloys are almost unaffected by the AA treatment at 225°C (**Figure 6.4a**). Results, obtained from alloys with the Zr and Zr+Cr additions show much the same values as the base alloy. The Sc-containing alloys attained their maximum tensile and yield strengths after 3h of AA at 325°C (**Figure 6.3**). The elongation to failure values increased along with increases in treatment time. The effect of overaging on tensile properties can be clearly seen in **Figure 6.5**. The tensile and yield strengths of the base alloy and Sc-alloys remain within the same range or even decrease range with increasing AA temperature, although for Sc-containing alloys, of course the values are much higher. Obviously, this effect can attribute to the formation of Al_3Sc nanoscale particles (**Figure 6.7**)

[58,150]. Due to the fast cooling rate of the HPDC process, supersaturated solid solution can be presented in these alloys. Thus, HPDC alloys have a good response either on the NA or AA, which lead to the hardening of the alloys.

T6 regime and outgassing

As briefly mentioned in Chapter 3, Al-Mg-Si wrought alloys have a good response to the T6 regime with an increase of mechanical properties, due to formation of nanoscale Mg_2Si precipitates in the α-Al matrix. However, Lumley *et al*[35] reported that HT of the Al-Si HPDC alloys with high temperatures of the ST (over 500°C) can lead to blistering, due to the presence of gases inside the cast, which is caused by technological features. Similar results were observed in the current research (**Figure 6.9**). During the high temperature treatment of the HPDC parts these gases expand, resulting in surface defects (e.g. blistering, bubbles), thus, material can be deformed during heat treatment. Therefore, except a high temperature of homogenization, which is usually applied for the wrought alloys was chosen, a lower temperature of the ST followed by AA (T6 regime) was employed for the experiments. These experiments proved, that for the high temperature ST (more than 520°C) leads to a significant reduction in elongation to failure, while yield strength can be significantly increased.

However, different solution treatment temperatures lead to a difference in final mechanical properties. The results of the hardness measurements, presented in **Figure 6.8 a** and **Figure 6.10 a-b** show low temperature ST does not affect the hardness of the base alloy, in contrast to high temperature ST. This effect can be caused by the formation of the large number of quench-in vacancies, nanoscale precipitates and GP zones [174,175]. On the other hand, as mentioned earlier, such treatment can negatively affect the tensile strength and elongation to failure. Moreover, even high temperature heat treatment does not lead to the dissolution of the Al_3Zr and Al_3Sc phases in Zr- and Sc- containing alloys respectively. This also was predicted by Thermo-Calc software (**Figure 3.9** and **Figure 3.10**). The Al_7Cr phase in Cr-containing alloys can be dissolved at rather high temperatures, however, the chosen temperatures of the solution treatment do not reach the melting temperature of the Al_7Cr phase, and some have been observed in CZ33 alloy (**Figure 6.12**). The dissolution of the needle-shaped Al_3Zr and a large cubic Al_7Cr intermetallics could lead to improvement of mechanical properties. Samuel *et. al.* [176] reported that sludge phases remained stable after solution treatment for 8 h at 515ºC.

Examples of the comparative tensile curves for the as-cast (dashed lines) and T6 (ST570°C+AA175°C) condition for the base alloy and alloy with 0.2 wt. % Sc (S2) are given in **Figure 6.18** and **Figure 6.13**. The T6 regime mainly affects the yield stress and the average value is 164 MPa for the base alloy in the as-cast state, whereas after HT, the average value increased up to 200 MPa. In the case of the S2 alloy, this effect is not so significant, the value increases from 194 MPa in as-cast state up to 220 MPa after HT. It should be mentioned, that due to a considerable amount of defects in these alloys after the heat treatment, mean values could not be compared to the as-cast state due to a high error level. Hence, the data only shows the general behaviour of the material only. Values for the ultimate tensile strength in the as-cast state and after HT are close to each other. Owing to the blistering in samples at high temperatures, the elongation to failure, especially for the base alloy, is lower in comparison to the as-cast state.

The samples which were homogenized in the temperature range of 480-520°C, have approximately the same amount of defects (porosity) caused by the high temperature treatment (**Figure 6.9**). It is worth mentioning, that for the studied system such low solution temperature does not lead to a maximum hardness (**Figure 6.10**). In combination with the further overaging treatment, however, it does lead to a significant improvement in ductility with an accompanying decrease in strength (in comparison to the as-cast properties) [177]. Therefore, for the further experiments the temperature of 520°C has been chosen. According to Royset *et al.* [13,14] the optimal temperature for the formation of the Al_3Sc precipitates lays between 250 and 350°C. The Sc-free alloys show a good response to the AA at 225°C, whereas Sc-containing alloys – to the 325°C. Hence, for the T6 regime, two different temperatures of the artificial aging were used (**Figure 6.14)**.

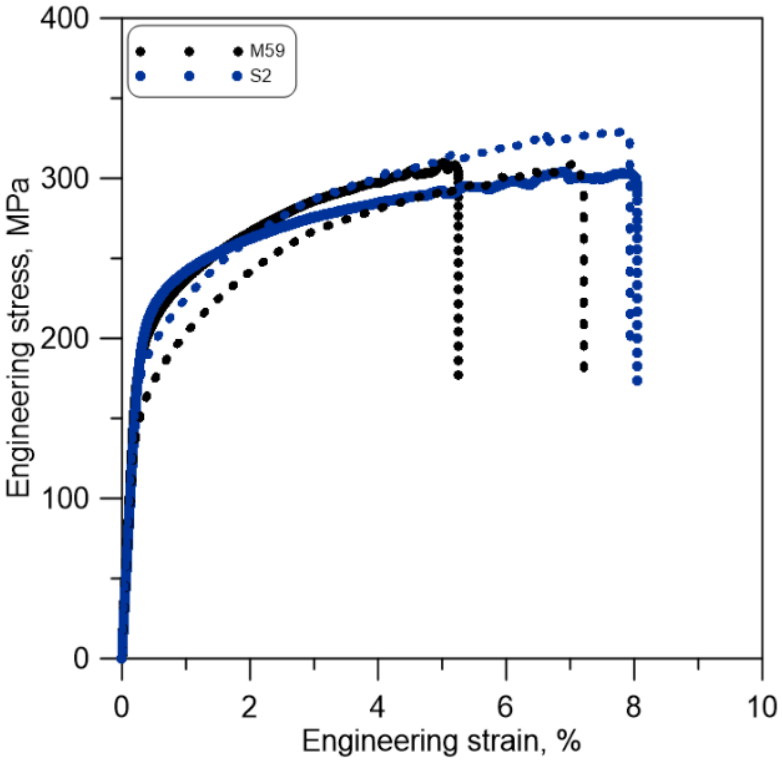

Figure 6.18 Comparative stress strain curves for the base alloy and S2 alloy after T6 regime and in as-cast state (dashed lines).

Despite the fact, that the artificial aging temperature is only slightly (25°C) higher, than the temperature necessary for the formation of the Mg_2Si precipitates (see **Figure 3.11a**), it must be high enough to cause the coarsening of the β'' and β'-Mg_2Si phases to the β-Mg_2Si (**Figure 5.16b,c** and **Figure 6.15a-b**). Moreover, only a small amount of the Al_3Zr precipitates were observed in the Zr containing alloys. Apparently a higher temperature of the AA is needed for the precipitation of Al_3Zr (L12) [149]. Consequently, the T6 regime is not so promising, as compared to the T5 at the same AA temperatures.

6.4 *Comparison of the results from the as-cast and heat treatment states*

The hardness values, in the as-cast state, across the plate change slightly, showing 92HV in the centre of the plate and increase up to 96HV closer to the plate edges (**Figure 6.8a**). The same trend for the HPDC was observed by Yang *et at* [164]. This effect is related to the different solidification speed of the inner and outer part of the cast. Hence, a higher volume fraction of Al+Mg_2Si is observed closer to the edge, thus, producing higher mean hardness values in those locations (see also **Figure 5.18**). The same trend is observed after ST (**Figure 6.8a**). However, the samples, which have been homogenized at temperatures of 480 and 500°C, do not even reach the hardness values at the as-cast state.

As was discussed earlier, the base alloy and the Z2 (Sc-free alloys) have a good response to the T5 regime at 225°C (**Figure 6.19**) and at 325°C in terms of the yield strength and ductility, whereas the S2 alloy (Sc-containing) has a peak value of the yield strength and tensile strength after T5 at 325°C. Such behaviour can be explained by the different temperature of the nanoscale precipitates formation. Regardless of fact that T6 regime is normally used for the Al-Mg-Si wrought alloys and is not recommended for the Al-Si HPDC casting alloys [35], tested alloys (M59, Z2, S2) resulted in maximum of ductility (due to the eutectic spheroidization), exceeding even as-cast state. But for all of that, the tensile strength and yield strength could barely reach values in the as-cast state (for the Sc-free alloys) and they are twice lower as compared to the as-cast state for the Sc-containing alloys.

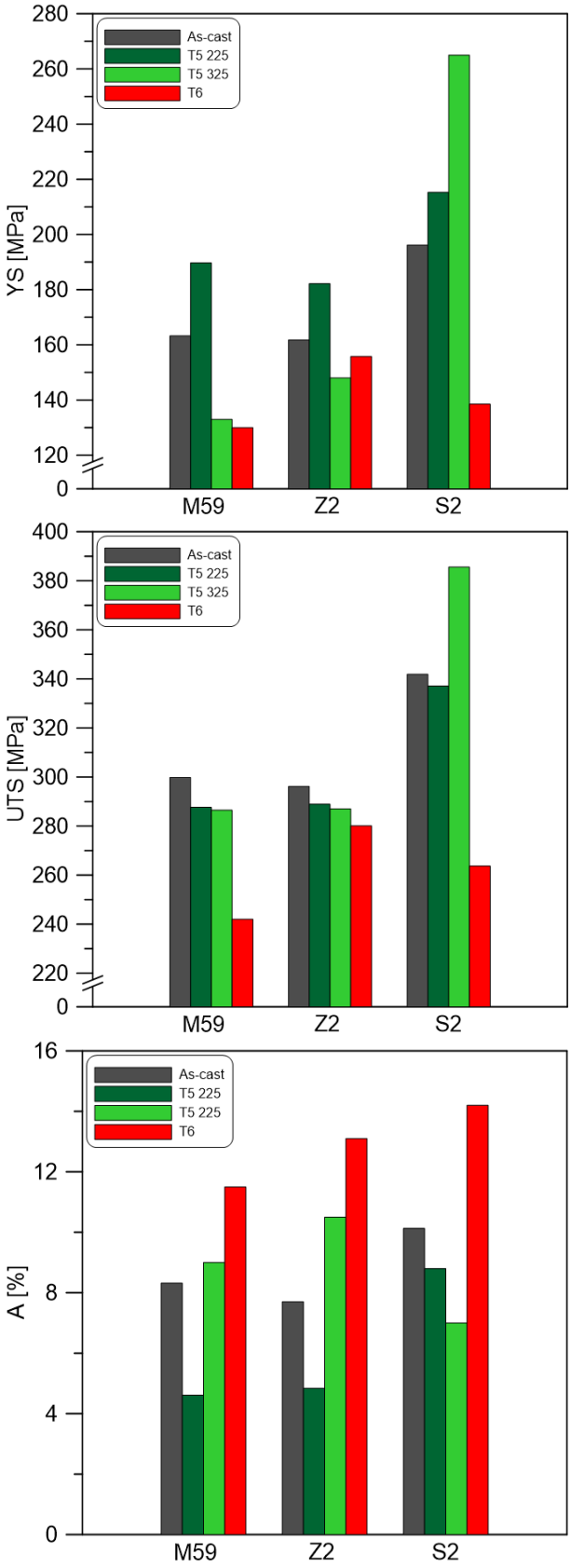

Figure 6.19 Tensile properties of the M59, Z2 and S2 alloys after different heat treatment regimes.

Chapter 7

Summary and conclusions

Concluding remarks

In the present work, new Al-Mg-Si-Mn casting alloys with the addition of Sc, Cr and Zr were developed and mechanical properties along with the microstructure were studied. The main findings are listed below:

1. As-cast state:

- Differential Scanning Calorimetry studies of the Al-Mg-Si-Mn alloys were carried out to determine the eutectic melting temperature of 595°C. The data obtained are very close to those from the established ternary phase diagram. The addition of Cr, Zr, and Sc as a single or as a dual addition to the hypoeutectic Al-Mg-Si-Mn alloys does not change the alloy solidification behaviour.

- Minor addition of the Cr, Zr and Sc does not change the microstructure essentially. These additives produced a slight modification of the interlamellar spacing. The main phases remain the same as in the base alloy and can be identified as the α-Al with an equiaxed, globular-rosette morphology with the average dendrite arm spacing (DAS) of about 15-35 μm and α-$Al_{15}(Mn,Fe)_3Si_2$ phase. In the Sc-free alloys Al_3Zr and Al_7Cr intermetallic phases were observed. Alloys with the single addition of Sc, according to the thermodynamic calculations and structure analysis, exhibit a new Al_3Sc phase with the irregular shape in the S2 (0.2 wt. %Sc) alloy only. In the Sc-containing alloy with the addition of Zr, Al_3Zr phase was observed.
- Zr, Cr and Sc mainly enriches solid solution. Mn and Cr were partly present in primary constituent particles and partly in solid solution.
- Within alloys with the same alloying element (e.g. Z1-Z2, S1-S2) or alloys with the small difference in the chemical composition (e.g. CZ11-CZ12, CZ22-33 and SZ11-21), the mean microhardness and nanohardness measurements gave nearly the same value. The hardness values of the Sc-free alloys show the same trend. In case of Sc-containing alloys mean hardness values for the full set are consistent (91HB±0.83).

- Additions of Zr or Zr+Cr do not lead to an increase in yield and tensile strength. Alloying with Zr maintains tensile properties on the same level as the base alloy. When a combination of Zr+Cr shows an increase of 10% of ultimate tensile strength compared to the base alloy. Alloying with Sc brings about a significant increase of tensile properties. 0.1 wt. % Sc is sufficient for solid solution enrichment and increasing additions of Sc do not lead to any further strengthening effect. With Sc addition new Al_3Sc intermetallics are formed in the as-cast structure. The SZ11 alloy, which was developed to substitute, to some extent for Sc shows comparable results to those for the S2 alloy.

2. Heat treated state:

- Artificial aging from as-cast state (T5) of the base alloy does not lead to precipitation strengthening, and in the studied temperature range did not affect the microstructure of the chosen alloys.
- Sc-free alloys show a good response to the T5 regime at 225°C, whereas the greatest benefit for those containing Sc was obtained at 325°C. Nano-dispersed precipitates Al_3Sc were found in Sc-series after artificial aging.
- The first step of T6 regime, high temperature solution treatment, leads to the spheroidization of fibrous eutectic which causes strong degradation of the tensile and yield strengths along with increases in ductility. Artificial aging at temperatures in the rage 125-325ºC did not lead to any significant precipitation strengthening, and in particular the full T6 treatment of the base alloy gave no improvement to the mechanical properties.
- Unexpected, HPDC alloys showed a positive response to the T6 regime in terms of ductility.

Perspective for further work

The present work is concerned with several topics and this thesis contributes to the understanding of the features formed by the alloying of an Al-Mg-Si-Mn alloy with Zr, Cr, and Sc and, further, can be used as the basis for future alloy development. Thus, based on the results obtained and presented in this thesis, a number of subjects believed to have the highest potential for further development are given below:

- In order to understand features such as size, distribution, volume fraction across the plate, coarsening and mechanical properties of the Al_3Sc and Al_3Zr precipitates, formed in HPDC alloys, in both as-cast and heat treated states a wider and more precise investigation should be carried out.
- In this work a good response to the heat treatment of the HPDC alloys has been demonstrated. The findings, therefore, can be used as a starting point for further/future research to determine the optimal heat treatment mode for HPDC alloys.

References

[1] Constellium, Going Full Circle: The Life-Cycle of Aluminium, n.d. https://www.constellium.com/sites/default/files/constellium_-_life_cycle_of_aluminium.pdf.

[2] Hydro, Aluminium – about Hydro and resource efficiency, 2012. https://www.hydro.com/en-DE/products-and-services/services/remelting-and-recycling/.

[3] Hydro, Aluminum, environment and society, 2012. www.hydro.com.

[4] O.M. Barabash, T.N. Legkaya, N.P. Korzhova, O. V. Sulzhenko, Thermodynamic analysis and experimental study of composite structure formation: In eutectic alloys α-Al + Mg2Si, Powder Metall. Met. Ceram. 39 (2000) 458–461. doi:10.1023/A:1011314406064.

[5] L. Pedersen, L. Arnberg, The Effect of Solution Heat Treatment and Quenching Rates.pdf, Metall. Mater. Trans. A. 32A (2001) 525. doi:10.1007/s11661-001-0069-y.

[6] M. Zhu, Z. Jian, G. Yang, Y. Zhou, Effects of T6 heat treatment on the microstructure, tensile properties, and fracture behavior of the modified A356 alloys, Mater. Des. 36 (2012) 243–249. doi:10.1016/j.matdes.2011.11.018.

[7] R.B.C. Cayless, Alloy and Temper Designation Systems for Aluminum and Aluminum Alloys, (n.d.). doi:10.1361/asmhba0001058.

[8] V.S. Zolotorevsky, N.A. Belov, M.V. Glazoff, Casting Aluminum Alloys, Elsevier, Oxford, 2007.

[9] H. Koch, R. Klos, Ductile casting alloys for automotive applications without heat treatment, in: Lean Weight Veh. Conf., 2003.

[10] M.C. Wuth, H. Koch, A.J. Franke, P. Ag, Producing steering wheel frames with an AlMg5Si2Mn-type alloy, Miner. (2000) 99–110.

[11] P. Krug, H. Koch, R. Klos, Magsimal-25 - A new High-Ductility Die Casting Alloy for Structural Parts in Automotive Industry, 59 (n.d.) 1–8.

[12] J.L. Jorstad, Excellent Die Casting Alloy System Made Better by Rheocasting, Die Cast. Eng. (2008) 18–20.

[13] J. Røyset, Scandium in Aluminium alloys overview: Physical Metallurgy, Properties and applications, Metall. Sci. AndTechnology. 25 (2007) 11–21.

[14] J. Røyset, U. Tundal, S.R. Skjervold, G. Waterloo, C. Braathen, O. Reiso, An investigation of Sc addition on the extrudability, recrystallisation resistance and mechanical properties of a 6082- and a 7108-alloy, Mater. Forum. 28 (2004) 246–251.

[15] M.S. Kaiser, A.S.W. Kurny, Effect of scandium on the grain refining and ageing behaviour of cast Al-Si-Mg alloy, Iran. J. Mater. Sci. Eng. 8 (2011) 1–8. doi:10.1016/j.matchar.2008.03.006.

[16] U. Patakham, J. Kajornchaiyakul, C. Limmaneevichitr, Grain refinement mechanism in an Al-Si-Mg alloy with scandium, J. Alloys Compd. 542 (2012) 177–186. doi:10.1016/j.jallcom.2012.07.018.

[17] J. Røyset, N. Ryum, Scandium in aluminium alloys, Int. Mater. Rev. 50 (2005) 19–44. doi:10.1179/174328005X14311.

[18] G.B. Scott, H. Brock, 2016 Annual Report Chairman & President ' S Message : Charting a Sustainable Course, 2016. www.aluminium.org.

[19] Z. Ahmad, Aluminium Alloys - New Trends in Fabrication and Applications, (2012) 368. doi:10.5772/3354.

[20] U. Sustainable, V. Chains, Activity report 2016: The Aluminium effect, 2016. https://european-aluminium.eu/media/1861/activity-report-2016_web.pdf.

[21] European Aluminium Association, Market Overview, (2018). https://www.european-aluminium.eu/activity-report-2017/market-overview/.
[22] Ducker Worldwide, Aluminum Content in Cars, 2016. www.ducker.com.
[23] The Aluminum Association, EDAG Silverado Body Lightweighting Final LCA Report, 2018. https://www.drivealuminum.org/research-resources/lca-report-edag-silverado-body-lightweighting-august-2018/.
[24] European Aluminmium Association, Aluminium in Cars, 2011. https://www.european-aluminium.eu/media/1326/aluminium-in-cars-unlocking-the-lightweighting-potential.pdf.
[25] Aluminium vs. steel in electric vehicles – the battle goes on – Aluminium Insider : Aluminium Insider, (n.d.). https://aluminiuminsider.com/aluminium-vs-steel-in-electric-vehicles-the-battle-goes-on/ (accessed November 7, 2018).
[26] Ducker Worldwide Report, Aluminum Content in North American Light Vehicles 2016 To 2028, (2017) 1–46. http://www.ducker.com/sites/default/files/protected-files/Aluminum Content in North American Light Vehicles 2016 to 2028 - Summary Report (1) (1).pdf.
[27] J. Hirsch, Automotive Trends in Aluminium - The European Perspective, Mater. Forum. 28 (2004) 15–23. doi:CCFBAADAA8178B7B1961FB26067826E1.
[28] T. Nottingham, Aluminum: Beneffits in transport, (2017). http://www.world-aluminium.org.
[29] J. Grandfield, Light Metals 2014, 2014. doi:10.1002/9781118888438.
[30] A. Morita, Aluminum alloys for automobile applications, in: ICAA-6, 1998: pp. 25–32.
[31] J.G. Kaufman, E.L. Rooy, Aluminum Alloy Castings: Properties , Processes , and Applications., ASM Int. (2004) 340. doi:10.1017/CBO9781107415324.004.
[32] E.J. Vinarcik, High Integrity Die Casting Processes, John Wiley & Sons, Inc., Hoboken, New Jersey, 2002.
[33] R.N. Lumley, R.G.O. Donnell, D.R. Gunasegaram, M. Gershenzon, a C. Yob, I.J. Polmear, The role of alloy composition in the heat treatment of aluminium high pressure die castings, Sci. Technol. 26 (2008) 0–9.
[34] S. Otarawanna, C.M. Gourlay, H.I. Laukli, A.K. Dahle, Microstructure formation in AlSi4MgMn and AlMg5Si2Mn high-pressure die castings, Metall. Mater. Trans. A Phys. Metall. Mater. Sci. 40 (2009) 1645–1659. doi:10.1007/s11661-009-9841-1.
[35] R.N. Lumley, R.G. Odonnell, D.R. Gunasegaram, M. Givord, Heat treatment of high-pressure die castings, Metall. Mater. Trans. A Phys. Metall. Mater. Sci. 38 (2007) 2564–2574. doi:10.1007/s11661-007-9285-4.
[36] W. Kurz, J.C. Fisher, Fundamentals of solidification, 3rd ed., Trans Tech Publications Ltd., 1989.
[37] P. Rambabu, N.E. Prasad, V. V Kutumbarao, Aerospace Materials and Material Technologies, (2017). doi:10.1007/978-981-10-2143-5.
[38] J.R. Davis, Alloying. Understanding the basics: Aluminum and Aluminum Alloys, ASM International, 2001. doi:10.1361/autb2001p351.
[39] A.M.A. Mohamed, F.H. Samuel, A Review on the Heat Treatment of Al-Si-Cu/Mg Casting Alloys, in: Conv. Nov. Appl., 2012: pp. 55–72. doi:10.5772/2798.
[40] E.L. Huskins, B. Cao, K.T. Ramesh, Strengthening mechanisms in an Al-Mg alloy, Mater. Sci. Eng. A. 527 (2010) 1292–1298. doi:10.1016/j.msea.2009.11.056.
[41] H. Fredriksson, U. Åkerlind, Solidification and Crystallization Processing in Metals and Alloys, 2012. doi:10.1002/9781119975540.
[42] R. Nadella, D.G. Eskin, Q. Du, L. Katgerman, Macrosegregation in direct-chill casting of aluminium alloys, Prog. Mater. Sci. 53 (2008) 421–480. doi:10.1016/j.pmatsci.2007.10.001.
[43] D.M. Stefanescu, Science and engineering of casting solidification: Third edition, 2015.

doi:10.1007/978-3-319-15693-4.
[44] L.F. Mondolfo, Aluminum alloys : structure and properties, Butterworths, 1976.
[45] T. Dorin, M. Ramajayam, S. Babaniaris, T.J. Langan, Micro-segregation and precipitates in as-solidified Al-Sc-Zr-(Mg)-(Si)-(Cu) alloys, Mater. Charact. 154 (2019) 353–362.
[46] J.D. Robson, P.B. Prangnell, Modelling Al3Zr dispersoid precipitation in multicomponent aluminium alloys, Mater. Sci. Eng. A. 352 (2003) 240–250. doi:10.1016/S0921-5093(02)00894-8.
[47] G.M. Novotny, A.J. Ardell, Precipitation of Al3Sc in binary Al-Sc alloys, Mater. Sci. Eng. A. 318 (2001) 144–154. doi:10.1016/S0921-5093(01)01326-0.
[48] Y.W. Riddle, T.H.J. Sanders, Contribution of Al_3Sc to Recrystallization Resistance in Wrought Al-Sc Alloys, Mater. Sci. Forum. 331–337 (2000) 939–944. doi:10.4028/www.scientific.net/MSF.331-337.939.
[49] O. Prach, J. Hornik, K. Mykhalenkov, Effect of the addition of Li on the structure and mechanical properties of hypoeutectic Al-Mg2Si alloys, Acta Polytech. 55 (2015). doi:10.14311/AP.2015.55.0253.
[50] O. Keßler, Precipitation hardening of aluminum alloys Part 1, Der Wärmebehandlungsmarkt. 2 (2001) 5–8. doi:10.1007/BF02672283.
[51] O. Keßler, Precipitation hardening of aluminum alloys Part 2, Der Wärmebehandlungsmarkt. 3 (2001) 5–8.
[52] G.A. Edwards, K. Stiller, G.L. Dunlop, M.J. Couper, The precipitation sequence in Al-Mg-Si alloys, Acta Metall. Mater. 46 (1998) 3893–3904.
[53] J. Roesler, H. Harders, M. Baeker, Mechanical Behaviour of Engineering Materials, 2007. doi:10.1007/978-3-540-73448-2.
[54] M.D.S. Totten George E., G.E. Totten, D.S. MacKenzie, Handbook of Aluminum; Volume 1: Physical Metallurgy and Processes. 2003, 2003. doi:10.1201/9780203912607.
[55] M.A. Meyers, K.K. Chawla, Mechanical Behavior of Materials, 2nd ed., Cambridge University Press, Cambridge, 2008.
[56] R. Labusch, A Statistical Theory of Solid Solution Hardening, Phys. Status Solidi. 41 (1970) 659–669. doi:10.1002/pssb.19700410221.
[57] L.F. Mondolfo, Metallography of aluminum alloys, 1943.
[58] L.S. Toropova, D.G. Eskinm, M.L. Kharakterovam, T. V. Dobatkina, Advanced Aluminum Alloys Containing Scandium: Structure and Properties, Routledge; 1 edition (June 1, 1998), 1998.
[59] N.A. Belov, D.G. Eskin, A.A. Aksenov, Multicomponent phase diagrams. Application for commercial Aluminum Alloys, Elsevier Ltd, 2005.
[60] Ø. Ryen, B. Holmedal, O. Nijs, E. Nes, E. Sjölander, H.-E. Ekström, Strengthening mechanisms in solid solution aluminum alloys, Metall. Mater. Trans. A. 37 (2006) 1999–2006. doi:10.1007/s11661-006-0142-7.
[61] R.L. Fleischer, The strengthening of metals, Reinhold, New York, 1964.
[62] S.B. Kadambi, V.D. Divya, U. Ramamurty, Evaluation of Solid-Solution Hardening in Several Binary Alloy Systems Using Diffusion Couples Combined with Nanoindentation, Metall. Mater. Trans. A Phys. Metall. Mater. Sci. 48 (2017) 4574–4582. doi:10.1007/s11661-017-4250-3.
[63] A. von Zeerleder, Die Ausscheidungshärtung (Vergütung) von Legierungen, unter besonderer Berücksichtigung der Aluminium-Legirungen, Aluminium. 8 (1938) 509–519.
[64] C.S.T. Chang, I. Wieler, N. Wanderka, J. Banhart, Positive effect of natural pre-ageing on precipitation hardening in Al-0.44 at% Mg-0.38 at% Si alloy, Ultramicroscopy. 109 (2009) 585–592. doi:10.1016/j.ultramic.2008.12.002.
[65] M.D.S. Totten George E., Handbook of Aluminum, MARCEL DEKKER, New

YorkMar, 2003. doi:10.1201/9780203912607.
[66] M.A. Meyers, K.K. Chawla, Mechanical Behaviour of Materials, 2009. http://www.smesfair.com/pdf/mechanical eng/smesfair09.pdf.
[67] K. Matsuda, S. Ikeno, H. Gamada, K. Fujii, Y. Uetani, T. Sato, et al., High-resolution electron microscopy on the structure of Guinier-Preston zones in an Al-1.6 mass Pct Mg2Si alloy, Metall. Mater. Trans. A. 29 (1998) 1161–1167. doi:10.1007/s11661-998-0242-7.
[68] J.J. Gracio, F. Barlat, E.F. Rauch, P.T. Jones, V.F. Neto, A.B. Lopes, Artificial aging and shear deformation behaviour of 6022 aluminium alloy, Int. J. Plast. 20 (2004) 427–445. doi:10.1016/S0749-6419(03)00095-0.
[69] D.J. Chakrabarti, Y. Peng, D.E. Laughlin, Precipitation in Al-Mg-Si Alloys with Cu Additions and the Role of the Q' and Related Phases, Mater. Sci. Forum. 396–402 (2002) 857–862. doi:10.4028/www.scientific.net/MSF.396-402.857.
[70] J. Banhart, C.S.T. Chang, Z. Liang, N. Wanderka, M.D.H. Lay, A.J. Hill, Natural aging in Al-Mg-Si alloys - A process of unexpected complexity, Adv. Eng. Mater. 12 (2010) 559–571. doi:10.1002/adem.201000041.
[71] T. Balakrishna Bhat, V.S. Arunachalam, Strengthening mechanisms in alloys, Proc. Indian Acad. Sci. Sect. C Eng. Sci. 3 (1980) 275–296. doi:10.1007/BF02842915.
[72] edited by J.R. Davis, Alloying Understand The Basic, ASM International, 2001. doi:10.1016/S1877-1823(09)70027-X.
[73] M. Warmuzek, Aluminum-silicon Casting alloys. Atlas of Microfractographs, ASM International, New York, 2004.
[74] L. Lu, R. Zhou, D. Lu, Y. Jiang, R. Zhou, Effect of cooling slope and manganese on the microstructure of hypereutectic Al-Si alloy with 2 %Fe, Mater. Res. 17 (2014) 511–517. doi:10.1590/S1516-14392013005000198.
[75] E. Ogris, A. Wahlen, H. Lüchinger, P.J. Uggowitzer, On the silicon spheroidization in Al-Si alloys, J. Light Met. 2 (2002) 263–269. doi:10.1016/S1471-5317(03)00010-5.
[76] W. Prukkanon, N. Srisukhumbowornchai, C. Limmaneevichitr, Modification of hypoeutectic Al – Si alloys with scandium, J. Alloys Compd. 477 (2009) 454–460. doi:10.1016/j.jallcom.2008.10.016.
[77] G. Wang, L. Yan, G. Ren, Z. Zhao, Analyzing as-cast age hardening of 356 cast alloy, J. Mater. Eng. Perform. 20 (2011) 399–404. doi:10.1007/s11665-010-9708-z.
[78] E. Georgatis, A. Lekatou, A.E. Karantzalis, H. Petropoulos, S. Katsamakis, A. Poulia, Development of a cast Al-Mg2Si-Si in situ composite: Microstructure, heat treatment, and mechanical properties, J. Mater. Eng. Perform. 22 (2013) 729–741. doi:10.1007/s11665-012-0337-6.
[79] L.C. Doan, K. Nakai, Y. Matsuura, S. Kobayashi, Y. Ohmori, Effects of Excess Mg and Si on the Isothermal Ageing Behaviours in the Al – Mg2Si Alloys, 43 (2002) 1371–1380.
[80] Z. Zhihao, M. Yi, C. Jianzhong, Effect of Mn on microstructures and mechanical properties of Al-Mg-Si-Cu-Cr-V alloy, China Foundry. (2012) 349–355. doi:10.3969/j.issn.0258-7076.2013.02.001.
[81] O. Prach, O. Trudonoshyn, M. Puchnin, Effects of chemical composition on mechanical properties of Al-Mg-Si-Mn based alloys, Mater. Eng. - Mater. Inžinierstvo. 24 (2017) 11–20.
[82] S. Farahany, N.A. Nordin, A. Ourdjini, T. Abu Bakar, E. Hamzah, M.H. Idris, et al., The sequence of intermetallic formation and solidification pathway of an Al-13Mg-7Si-2Cu in-situ composite, Mater. Charact. 98 (2014) 119–129. doi:10.1016/j.matchar.2014.09.018.
[83] S.D. McDonald, A.K. Dahle, J.A. Taylor, D.H. StJohn, Eutectic grains in unmodified and strontium-modified hypoeutectic aluminum-silicon alloys, Met. Mater. Trans. A. 35

(2004) 1829–1837. doi:10.1007/s11661-004-0091-y.
[84] S. Ji, W. Yang, F. Gao, D. Watson, Z. Fan, Effect of iron on the microstructure and mechanical property of Al-Mg-Si-Mn and Al-Mg-Si diecast alloys, Mater. Sci. Eng. A. 564 (2013) 130–139. doi:10.1016/j.msea.2012.11.095.
[85] A.M. Samuel, F.H. Samuel, C. Villeneuve, H.W. Doty, S. Valtierra, Effect of trace elements on β-Al5FeSi characteristics, porosity and tensile properties of Al-Si-Cu (319) cast alloys, Int. J. Cast Met. Res. 14 (2001) 97–120. doi:10.1080/13640461.2001.11819429.
[86] L. Lodgaard, N. Ryum, Precipitation of dispersoids containing Mn and / or Cr in Al – Mg – Si alloys, Mater. Sci. Eng. A. 283 (2000) 144–152.
[87] J. Zhang, Z. Fan, Y.Q. Wang, B.L. Zhou, Equilibrium pseudobinary Al-Mg2Si phase diagram, Mater. Sci. Technol. 17 (2001) 494–496. doi:10.1179/026708301101510311.
[88] A.M. Si, K.C.H. Kumar, N. Chakraborti, H. Lukas, O. Bodak, L. Rokhlin, Aluminium – Magnesium – Silicon, Crystallogr. Thermodyn. Data. IV (2000) 165–177.
[89] V. Raghavan, Al-Mg-Si-Zn (Aluminum-Magnesium-Silicon-Zinc), J. Phase Equilibria Diffus. 32 (2010) 1–3. doi:10.1007/s11669-010-9803-8.
[90] O.M. Barabash, O. V. Sulgenko, T.N. Legkaya, N.P. Korzhova, Experimental analysis and thermodynamic calculation of the structural regularities in the fusion diagram of the system of alloys Al-Mg-Si, J. Phase Equilibria. 22 (2001) 5–11. doi:10.1007/s11669-001-0049-3.
[91] S.P. Li, S.X. Zhao, M.X. Pan, D.Q. Zhao, X.C. Chen, O.M. Barabash, et al., Solidification and structural characteristics of alpha(Al)-Mg2Si eutectic, Mater. Trans. Jim. 38 (1997) 553–559. doi:10.2320/matertrans1989.38.553.
[92] V. Raghavan, Al-Mg-Si (Aluminum-Magnesium-Silicon), J. Phase Equilibria Diffus. 28 (2007) 189–191. doi:10.1007/s11669-007-9027-8.
[93] Y. Tang, Y. Du, L. Zhang, X. Yuan, G. Kaptay, Thermodynamic description of the Al-Mg-Si system using a new formulation for the temperature dependence of the excess Gibbs energy, Thermochim. Acta. 527 (2012) 131–142. doi:10.1016/j.tca.2011.10.017.
[94] F. Yan, S. Ji, Z. Fan, Effect of Excess Mg on the Microstructure and Mechanical Properties of Al-Mg 2 Si High Pressure Die Casting Alloys, 765 (2013) 64–68. doi:10.4028/www.scientific.net/MSF.765.64.
[95] A. Furihata, K. Matsuda, J.Y. Nakamura, S. Ikeno, Y. Uetani, Age-hardening behavior and HRTEM observation of precipitates in excess Mg type Al-Mg- Si-Ag alloy, 10th Int. Conf. Alum. Alloy. 519–521 (2006) 507–510. doi:10.4028/www.scientific.net/MSF.519-521.507.
[96] J. Zhang, Z. Fan, Y.Q. Wang, B.L. Zhou, Microstructural evolution of the in situ Al-15wt.%Mg2Si composite with extra Si contents, Scr. Mater. 42 (2000) 1101–1106. doi:10.1016/S1359-6462(00)00338-9.
[97] J. Zhang, Y. Wang, B. Yang, B. Zhou, I. Introduction, Effects of Si content on the microstructure and tensile strength of an in situ Al/Mg2Si Si composite, (1999).
[98] R. Franke, D. Dragulin, A. Zovi, F. Casarotto, Progress in ductile aluminium high pressure die casting alloys for the automotive industry, La Metall. Ital. (2007) 19–24.
[99] Rheinfelden Alloys GmbH & Co. KG, Magsimal®-59, 2017.
[100] Rheinfelden Alloys GmbH & Co. KG, Primary Aluminium alloys for Pressure Die Casting, n.d.
[101] Rheinfelden Alloys GmbH & Co. KG, Hüttenaluminium-Druckguss-Legierungen, Ausgabe 3 (2015).
[102] D.G. Altenpohl, P. Furrer, Innovative Aluminum Applications for Automotive Use in Europe, Miner. Met. Mater. Soc. (2000) 59–75.
[103] A356.0 Aluminium casting alloy (7Si-0.3Mg), 2012. http://www.hadleighcastings.com/uploads/A356.0 Alloy Detail.pdf.

[104] S. Ji, W. Yang, F. Gao, D. Watson, Z. Fan, Effect of iron in Al-Mg-Si-Mn ductile diecast alloy, Miner. Met. Mater. Ser. (2016) 317–322. doi:10.1007/978-3-319-65136-1_55.
[105] H. Okamoto, Al-Cr (Aluminum-Chromium), J. Phase Equilibria Diffus. 29 (2008) 112–113. doi:10.1007/s11669-007-9225-4.
[106] S. Wang, K. Matsuda, T. Kawabata, Y. Zou, T. Yamazaki, S. Ikeno, Effect of TM-addition on the aging behaviour of Al-Mg-Si alloys, Mater. Trans. 52 (2011) 229–234. doi:10.2320/matertrans.M2010370.
[107] D.Y. Maeng, J.H. Lee, S.I. Hong, The effect of transition elements on the superplastic behavior of Al-Mg alloys, Mater. Sci. Eng. A. 357 (2003) 188–195. doi:10.1016/S0921-5093(03)00160-6.
[108] J. Davis, Aluminum and Aluminum Alloys, Light Met. Alloy. (2001) 351–416. doi:10.1361/autb2001p351.
[109] Y. Meng, J. Cui, Z. Zhao, L. He, Effect of Zr on microstructures and mechanical properties of an AlMgSiCuCr alloy prepared by low frequency electromagnetic casting, Mater. Charact. 92 (2014) 138–148. doi:10.1016/j.matchar.2014.02.013.
[110] W. Yuan, Z. Liang, Effect of Zr addition on properties of Al-Mg-Si aluminum alloy used for all aluminum alloy conductor, Mater. Des. 32 (2011) 4195–4200. doi:10.1016/j.matdes.2011.04.034.
[111] L. Lityńska, D. Abou-Ras, G. Kostorz, J. Dutkiewicz, TEM and HREM study of Al3Zr precipitates in an Al-Mg-Si-Zr alloy, J. Microsc. 223 (2006) 182–184. doi:10.1111/j.1365-2818.2006.01615.x.
[112] Y. Deng, G. Xu, Z. Yin, X. Lei, J. Huang, Effects of Sc and Zr microalloying additions on the recrystallization texture and mechanism of Al-Zn-Mg alloys, J. Alloys Compd. 580 (2013) 412–426. doi:10.1016/j.jallcom.2013.06.020.
[113] L. Lityńska-Dobrzyńska, Precipitation of Phases in Al-Mg-Si-Cu Alloy with Sc and Zr Additions during Heat Treatment, Solid State Phenom. 130 (2007) 163–166. doi:10.4028/www.scientific.net/SSP.130.163.
[114] M. Cabibbo, E. Evangelista, A TEM study of the combined effect of severe plastic deformation and (Zr), (Sc+Zr)-containing dispersoids on an Al-Mg-Si alloy, J. Mater. Sci. 41 (2006) 5329–5338. doi:10.1007/s10853-006-0306-2.
[115] G. Timelli, S. Ferraro, A. Fabrizi, Effects of chromium and bismuth on secondary aluminium foundry alloys, Int. J. Cast Met. Res. 26 (2013) 239–246. doi:10.1179/1743133613Y.0000000061.
[116] A.F. Norman, P.B. Prangnell, R.S. McEwen, The solidification behaviour of dilute aluminium-scandium alloys, Acta Mater. 46 (1998) 5715–5732. doi:10.1016/S1359-6454(98)00257-2.
[117] E.M. Savitsky, I.V. Terehova, I.V. Burov, Study of rare earth crystals and alloys, in: Fourth Conf. Rare Earth Res., 1964: pp. 409–420. doi:10.1021/ef0341062.
[118] M.O. Shevchenko, V.G. Kudin, V. V. Berezutskii, M.I. Ivanov, V.S. Sudavtsova, Thermodynamic Properties of Al–Sc Alloys, Powder Metall. Met. Ceram. 53 (2014) 243–249. doi:10.1007/s11106-014-9610-6.
[119] H. Okamoto, Phase diagram updates: Al-Sc (Aluminum-Scandium), J. Phase Equilibria. 12 (1991) 612–613. doi:10.1007/BF02645176.
[120] H. Okamoto, Al-Sc (Aluminum-Scandium), J. Phase Equilibria. 21 (2000) 310. doi:10.1007/BF02645082.
[121] R. Hyland, Homogeneous nucleation kinetics of Al3Sc in a dilute Al-Sc alloy, Metall. Trans. A. 23 (1992) 1947–1955. doi:10.1007/BF02647542.
[122] E.A. Marquis, D.N. Seidman, Nanoscale structural evolution of Al3Sc precipitates in Al(Sc) alloys, Acta Mater. 49 (2001) 1909–1919. doi:10.1016/S1359-6454(01)00116-1.
[123] O. Trudonoshyn, O. Prach, Multistep nucleation and multi-modification effect of Sc in hypoeutectic Al-Mg-Si alloys, Heliyon. (2019) 1–12.

doi:10.1016/j.heliyon.2019.e01202.
[124] J. Røyset, N. Ryum, D. Bettella, A. Tocco, Z. Jia, J.K. Solberg, et al., On the addition of precipitation- and work-hardening in an Al-Sc alloy, Mater. Sci. Eng. A. 483–484 (2008) 175–178. doi:10.1016/j.msea.2006.09.164.
[125] C. Watanabe, D. Watanabe, R. Tanii, R. Monzen, Coarsening of cuboidal Al3Sc precipitates in an Al-Mg-Sc alloy, Philos. Mag. Lett. 90 (2010) 103–111. doi:10.1080/09500830903459655.
[126] V. Ocenasek, M. Slamova, Resistance to recrystallization due to Sc and Zr addition to Al-Mg alloys, Mater. Charact. 47 (2001) 157–162. doi:10.1016/S1044-5803(01)00165-6.
[127] J. zhi Dang, Y. feng Huang, J. Cheng, Effect of Sc and Zr on microstructures and mechanical properties of as-cast Al-Mg-Si-Mn alloys, Trans. Nonferrous Met. Soc. China (English Ed. 19 (2009) 540–544. doi:10.1016/S1003-6326(08)60309-X.
[128] Y. Meng, Z.H. Zhao, J.Z. Cui, Effect of minor Zr and Sc on microstructures and mechanical properties of Al-Mg-Si-Cu-Cr-V alloys, Trans. Nonferrous Met. Soc. China (English Ed. 23 (2013) 1882–1889. doi:10.1016/S1003-6326(13)62673-4.
[129] K.B. Hyde, A.F. Norman, P.B. Prangnell, The effect of cooling rate on the morphology of primary Al3Sc intermetallic particles in Al-Sc alloys, Acta Mater. 49 (2001) 1327–1337. doi:10.1016/S1359-6454(01)00050-7.
[130] J. Rakhmonov, G. Timelli, F. Bonollo, The Effect of Transition Elements on High-Temperature Mechanical Properties of Al–Si Foundry Alloys–A Review, Adv. Eng. Mater. 18 (2016) 1096–1105. doi:10.1002/adem.201500468.
[131] E. Clouet, J.M. Sanchez, C. Sigli, First-principles study of the solubility of Zr in Al, Phys. Rev. B - Condens. Matter Mater. Phys. 65 (2002) 1–13. doi:10.1103/PhysRevB.65.094105.
[132] E. Nes, Precipitation of the metastable cubic Al3Zr-phase in subperitectic Al-Zr alloys, Acta Metall. 20 (1972) 499–506. doi:10.1016/0001-6160(72)90005-3.
[133] J.A. Wagner, R.N. Shenoy, The effect of copper, chromium, and zirconium on the microstructure and mechanical properties of Al-Zn-Mg-Cu alloys, Metall. Trans. A. 22 (1991) 2809–2818. doi:10.1007/BF02851375.
[134] V.. Davydov, T.. Rostova, V.. Zakharov, Y.. Filatov, V.. Yelagin, Scientific principles of making an alloying addition of scandium to aluminium alloys, Mater. Sci. Eng. A. 280 (2000) 30–36. doi:10.1016/S0921-5093(99)00652-8.
[135] Z. Yin, Q. Pan, Y. Zhang, F. Jiang, Effect of minor Sc and Zr on the microstructure and mechanical properties of Al-Mg based alloys, Mater. Sci. Eng. A. 280 (2000) 151–155. doi:10.1016/S0921-5093(99)00682-6.
[136] V.I. Elagin, V. V. Zakharov, T.D. Rostova, Scandium-alloyed aluminum alloys, Met. Sci. Heat Treat. 34 (1992) 37–45. doi:10.1007/BF00768707.
[137] C.B. Fuller, D.N. Seidman, D.C. Dunand, Mechanical properties of Al(Sc,Zr) alloys at ambient and elevated temperatures, Acta Mater. 51 (2003) 4803–4814. doi:10.1016/S1359-6454(03)00320-3.
[138] L. Lityńska-Dobrzyńska, J. Dutkiewicz, W. Maziarz, P. Ochin, Structure and properties of Al-Mg-Si alloys with Zr and Sc additions produced by melt spinning and twin rolling casting techniques, Kov. Mater. 48 (2010) 9–15. doi:10.4149/km 2010 1 9.
[139] L. Lityńska-Dobrzyńska, Effect of heat treatment on the sequence of phases formation in Al-Mg-Si alloy with Sc and Zr additions, Arch. Metall. Mater. 51 (2006) 555–560.
[140] J.L. Murray, The Al-Cr (aluminum-chromium) system, J. Phase Equilibria. 19 (1998) 368–375. doi:10.1361/105497198770342102.
[141] V. V. Zakharov, Effect of scandium on the structure and properties of aluminum alloys, Met. Sci. Heat Treat. 45 (2003) 246–253. doi:10.1023/A:1027368032062.
[142] S. Lathabai, P.G. Lloyd, The effect of scandium on the microstructure, mechanical

properties and weldability of a cast Al-Mg alloy, Acta Mater. 50 (2002) 4275–4292. doi:10.1016/S1359-6454(02)00259-8.
[143] D. Pan, S. Zhou, Z. Zhang, M. Li, Y. Wu, Effects of Sc(Zr) on the microstructure and mechanical properties of as-cast Al–Mg alloys, Mater. Sci. Technol. (United Kingdom). 33 (2017) 751–757. doi:10.1080/02670836.2016.1270573.
[144] O. Trudonoshyn, O. Prach, V. Boyko, M. Puchnin, K. Mykhalenkov, Design of a new casting alloys containing Li or Ti+Zr and optimization of its heat treatment, in: Met. 2014 - 23rd Int. Conf. Metall. Mater. Conf. Proc., 2014.
[145] O. Trudonoshyn, M. Puchnin, K. Mykhalenkov, Features of structure formation and changes in the mechanical properties of cast Al-Mg-Si-Mn alloy with the addition of (Ti + Zr), Acta Polytech. 55 (2015) 282–290. doi:10.14311/AP.2015.55.0282.
[146] O. Trudonoshyn, M. Puchnin, O. Prach, Use of the ABI technique to measure the mechanical properties of aluminium alloys: Effect of heat-treatment conditions on the mechanical properties of alloys, Mater. Tehnol. 50 (2016). doi:10.17222/mit.2014.295.
[147] L.C. Doan, K. Nakai, Y. Matsuura, S. Kobayashi, Y. Ohmori, Effects of Excess Mg and Si on the Isothermal Ageing Behaviours in the Al – Mg 2 Si Alloys, 43 (2002) 1371–1380.
[148] D.. Chakrabarti, D.E. Laughlin, Phase relations and precipitation in Al–Mg–Si alloys with Cu additions, Prog. Mater. Sci. 49 (2004) 389–410. doi:10.1016/S0079-6425(03)00031-8.
[149] K.E. Knipling, R.A. Karnesky, C.P. Lee, D.C. Dunand, D.N. Seidman, Precipitation evolution in Al-0.1Sc, Al-0.1Zr and Al-0.1Sc-0.1Zr (at.%) alloys during isochronal aging, Acta Mater. 58 (2010) 5184–5195. doi:10.1016/j.actamat.2010.05.054.
[150] V. Singh, K.S. Prasad, A.A. Gokhale, Microstructure and age hardening response of cast Al-Mg-Sc-Zr alloys, J. Mater. Sci. 39 (2004) 2861–2864. doi:10.1023/B:JMSC.0000021465.99764.b5.
[151] A.L. Dons, The Alstruc homogenization model for industrial aluminum alloys, J. Light Met. 1 (2001) 133–149. doi:10.1016/S1471-5317(01)00007-4.
[152] W.C. Oliver, G.M. Pharr, An improved technique for determining hardness and elastic modulus using load and displacement sensing indentation experiments, J. Mater. Res. 7 (1992) 1564–1583. doi:10.1557/JMR.1992.1564.
[153] C.H. Cáceres, C.J. Davidson, J.R. Griffiths, Q.G. Wang, The Effect of Mg on the Microstructure and Mechanical Behavior of Al-Si-Mg casting alloys, Metall. Mater. Trans. A. 30A (1999) 2611–2618.
[154] Q.G. Wang, C.J. Davidson, Solidification and precipitation behaviour of Al-Si-Mg casting alloys, J. Mater. Sci. 36 (2001) 739–750. doi:10.1023/A:1004801327556.
[155] W.C. Yang, F. Gao, S.X. Ji, Formation and sedimentation of Fe-rich intermetallics in Al-Si-Cu-Fe alloy, Trans. Nonferrous Met. Soc. China (English Ed. 25 (2015) 1704–1714. doi:10.1016/S1003-6326(15)63776-1.
[156] N.C.W. Kuijpers, Kinetics of the β-AlFeSi to α-Al(FeMn)Si transformation in Al-Mg-Si alloys, 2004.
[157] N.C.W. Kuijpers, F.J. Vermolen, C. Vuik, P.T.G. Koenis, K.E. Nilsen, S. van der Zwaag, The dependence of the β-AlFeSi to α-Al(FeMn)Si transformation kinetics in Al-Mg-Si alloys on the alloying elements, Mater. Sci. Eng. A. 394 (2005) 9–19. doi:10.1016/j.msea.2004.09.073.
[158] S. Seifeddine, I.L. Svensson, The influence of Fe and Mn content and cooling rate on the microstructure and mechanical properties of A380-die casting alloys, Metall. Sci. Technol. 27 (2009) 11–20.
[159] O. Prach, O. Trudonoshyn, P. Randelzhofer, Körner, K. Durst, Multi-alloying effect of Sc, Zr, Cr on the Al-Mg-Si-Mn high-pressure die casting alloys, Mater. Charact. 168 (2020). doi:10.1016/j.matchar.2020.110537.

[160] C.L. Chen, G.D. West, R.C. Thomson, Characterisation of Intermetallic Phases in Multicomponent Al-Si Casting Alloys for Engineering Applications, Mater. Sci. Forum. 519–521 (2006) 359–364. doi:10.4028/www.scientific.net/MSF.519-521.359.
[161] C.L. Chen, A. Richter, R.C. Thomson, Investigation of mechanical properties of intermetallic phases in multi-component Al-Si alloys using hot-stage nanoindentation, Intermetallics. 18 (2010) 499–508. doi:10.1016/j.intermet.2009.09.013.
[162] B. Contor, Solidification and Castings, IOP Publishing, 2003.
[163] D. Shimosaka, S. Kumai, F. Casarotto, S. Watanabe, Effect of Cooling Rates during Solidification of Al-5.5%Mg-2.3%Si-0.6%Mn and Al-13%Mg2Si Pseudo-Binary Alloys on Their Secondary-Particle Morphology and Tear Toughness, Mater. Trans. 52 (2011) 920–927. doi:10.2320/matertrans.L-MZ201125.
[164] K. Yang, A.V. Nagasekhar, C.H. Caceres, The Skin Effect in a High Pressure Die Cast Mg-9%Al Alloy, Adv. Mater. Res. 97–101 (2010) 743–747. doi:10.4028/www.scientific.net/AMR.97-101.743.
[165] S. Ji, D. Watson, Z. Fan, M. White, Development of a super ductile diecast Al-Mg-Si alloy, Mater. Sci. Eng. A. 556 (2012) 824–833. doi:10.1016/j.msea.2012.07.074.
[166] K.T. Kashyap, S. Murali, K.S. Raman, K.S.S. Murthy, Casting and heat treatment variables of Al-7Si-Mg alloy, Mater. Sci. Technol. 9 (1993) 189–204. doi:10.1179/mst.1993.9.3.189.
[167] N.D. Johnson, Processing and mechanical properties of cast aluminum containing scandium, zirconium, and ytterbium, 2011. https://digitalcommons.mtu.edu/etds/28.
[168] K.E. Knipling, D.N. Seidman, D.C. Dunand, Ambient- and high-temperature mechanical properties of isochronally aged Al-0.06Sc, Al-0.06Zr and Al-0.06Sc-0.06Zr (at.%) alloys, Acta Mater. 59 (2011) 943–954. doi:10.1016/j.actamat.2010.10.017.
[169] M.R. Ghorbani, M. Emamy, N. Nemati, Microstructural and mechanical characterization of Al-15%Mg2Si composite containing chromium, Mater. Des. 32 (2011) 4262–4269. doi:10.1016/j.matdes.2011.04.020.
[170] K.E. Knipling, D.C. Dunand, D.N. Seidman, Criteria for developing castable, creep-resistant aluminum-based alloys - A review, Int. J. Mater. Res. 97 (2006) 246–265. doi:10.3139/146.101249.
[171] Y.S. Lee, J.H. Cha, S.H. Kim, C.Y. Lim, H.W. Kim, Effect of pre-homogenization deformation treatment on the workability and mechanical properties of AlMg5Si2Mn alloy, Mater. Sci. Eng. A. 685 (2017) 244–252. doi:10.1016/j.msea.2016.12.107.
[172] O. Trudonoshyn, O. Prach, P. Randelzhofer, K. Durst, C. Körner, Heat Treatment of the New High-Strength High-Ductility Al-Mg-Si-Mn Alloys with Sc, Zr and Cr Additions, SSRN Electron. J. (2020). doi:10.2139/ssrn.3678844.
[173] M. Kolar, K.O. Pedersen, S. Gulbrandsen-dahl, K. Teichmann, K. Marthinsen, The Effect of Deformation on the Artificial Aging Response of an Al-Mg-Si Alloy, J. Phys. Sci. Appl. 6 (2010) 435–440. doi:10.17265/2159-5348/2016.06.006.
[174] H. Seyedrezai, D. Grebennikov, P. Mascher, H.S. Zurob, Study of the early stages of clustering in Al-Mg-Si alloys using the electrical resistivity measurements, Mater. Sci. Eng. A. 525 (2009) 186–191. doi:10.1016/j.msea.2009.06.054.
[175] C.D. Marioara, S.J. Andersen, J. Jansen, H.W. Zandbergen, Atomic model for GP-zones in a 6082 Al-Mg-Si system, Acta Mater. 49 (2001) 321–328. doi:10.1016/S1359-6454(00)00302-5.
[176] A.M. Samuel, F.H. Samuel, Effect of alloying elements and dendrite arm spacing on the microstructure and hardness of an Al-Si-Cu-Mg-Fe-Mn (380) aluminium die-casting alloy, J. Mater. Sci. 30 (1995) 1698–1708.
[177] D. Dragulin, M. Belte, B. Ag, AlMg5Si2Mn – Aluminiumdruckgusslegierung unter dem Aspekt einer Wärmebehandlungsperspektive, Druckguss. 3 (2010) 875–876.

APPENDICES

Appendix A.1 Casting cycle for HPDC

An illustration of the cycle using the cold-chamber die casting process is shown in the figure below. Initially, liquid metal is metered into an injection system (a), which is then immediately pushed (b) through a runner system (c) into a die cavity (d) under high pressure. High pressures are maintained on the alloy during solidification. After complete solidification, the die opens (e) and the component is ejected (*f*) [32].

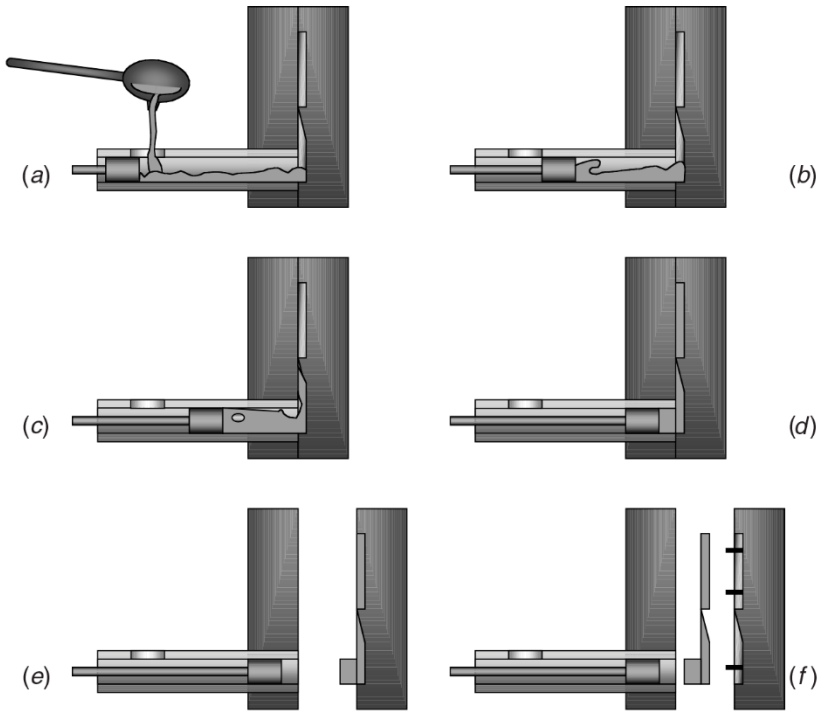

Casting cycle for cold-chamber die casting [32]

Appendix A.2 Designation system of the heat treatment of aluminum alloys

Designation system of the heat treatment of aluminum alloys[72]

Letter	Meaning
F	As fabricated – Applies to products of a forming process in which no special control over thermal or strain hardening conditions is employed
O	Annealed – Applies to product which has been heated to produce the lowest strength condition to improve ductility and dimensional stability
H	Strain Hardened – Applies to products that are strengthened through cold-working. The strain hardening may be followed by supplementary thermal treatment, which produces some reduction in strength.
W	Solution Heat-Treated – An unstable temper applicable only to alloys which age spontaneously at room temperature after solution heat-treatment
T	Thermally Treated - Applies to product that has been heat-treated, sometimes with supplementary strain-hardening, to produce a stable temper.

Appendix A.3 Sequence of the reactions in alloys during equilibrium solidification

Sequence of the reactions in the Z-series of alloys during equilibrium solidification		
TºC	Z1	Z2
745	-	L+ Al_3Zr
685	L+ Al_3Zr	-
622	L+ Al_3Zr+ $Al_{15}(MnFe)_3Si_2$	
618	L+ Al_3Zr+ $Al_{15}(MnFe)_3Si_2$+Al	
591	Al_3Zr+ $Al_{15}(MnFe)_3Si_2$ + Al+ Mg_2Si	

Sequence of the reactions in the S-series of alloys during equilibrium solidification		
TºC	S1	S2
635	-	L+Al_3Sc
622	L+ $Al_{15}(MnFe)_3Si_2$	L+ Al_3Sc+ $Al_{15}(MnFe)_3Si_2$
618	L+ $Al_{15}(MnFe)_3Si_2$ + Al	L+ Al_3Sc+ $Al_{15}(MnFe)_3Si_2$+ Al
591	$Al_{15}(MnFe)_3Si_2$ + Al+ Mg_2Si	$Al_15(MnFe)_3Si_2$ + Al+ Al_3Sc+ Mg_2Si
550	$Al_{15}(MnFe)_3Si_2$ + Al+ Mg_2Si+ Al_3Sc	-

Sequence of the reactions in the CZ-series of alloys during equilibrium solidification		
TºC	CZ11	CZ22
750	-	L+ Al_3Zr
678	L+ Al_3Zr	L+ Al_3Zr+ $Al_{45}Cr_7$
652	L+ Al3Zr+$Al_{45}Cr_7$	-
622	L+ Al_3Zr+ $Al_{45}Cr_7$+ $Al_{15}(MnFe)_3Si_2$	
621	L+ Al_3Zr+ $Al_{45}Cr_7$+ $Al_{15}(MnFe)_3Si_2$+Al	
591	Al_3Zr+ $Al_{45}Cr_7$+ $Al_{15}(MnFe)_3Si_2$+Al+ Mg_2Si	

Sequence of the reactions in the SZ-series of alloys during equilibrium solidification		
TºC	SZ11	SZ21
689	L+ Al_3Zr	L+ Al_3Zr
638	-	L+ Al_3Zr+ Al_3Sc
624	L+ Al_3Zr+ $Al_{15}(MnFe)_3Si_2$	L+ Al_3Zr+ Al_3Sc+ $Al_{15}(MnFe)_3Si_2$
622	L+ Al_3Zr+ $Al_{15}(MnFe)_3Si_2$ + Al	L+ Al_3Zr+ Al_3Sc+ $Al_{15}(MnFe)_3Si_2$+ Al
591	Al_3Zr+ $Al_{15}(MnFe)_3Si_2$ + Al+ Mg_2Si	Al_3Zr+ Al_3Sc+ $Al_{15}(MnFe)_3Si_2$ + Al+ Mg_2Si
550	Al_3Zr+ $Al_{15}(MnFe)_3Si_2$ + Al+ Mg_2Si+ Al_3Sc	-

Appendix A.4 Microhardness after AA

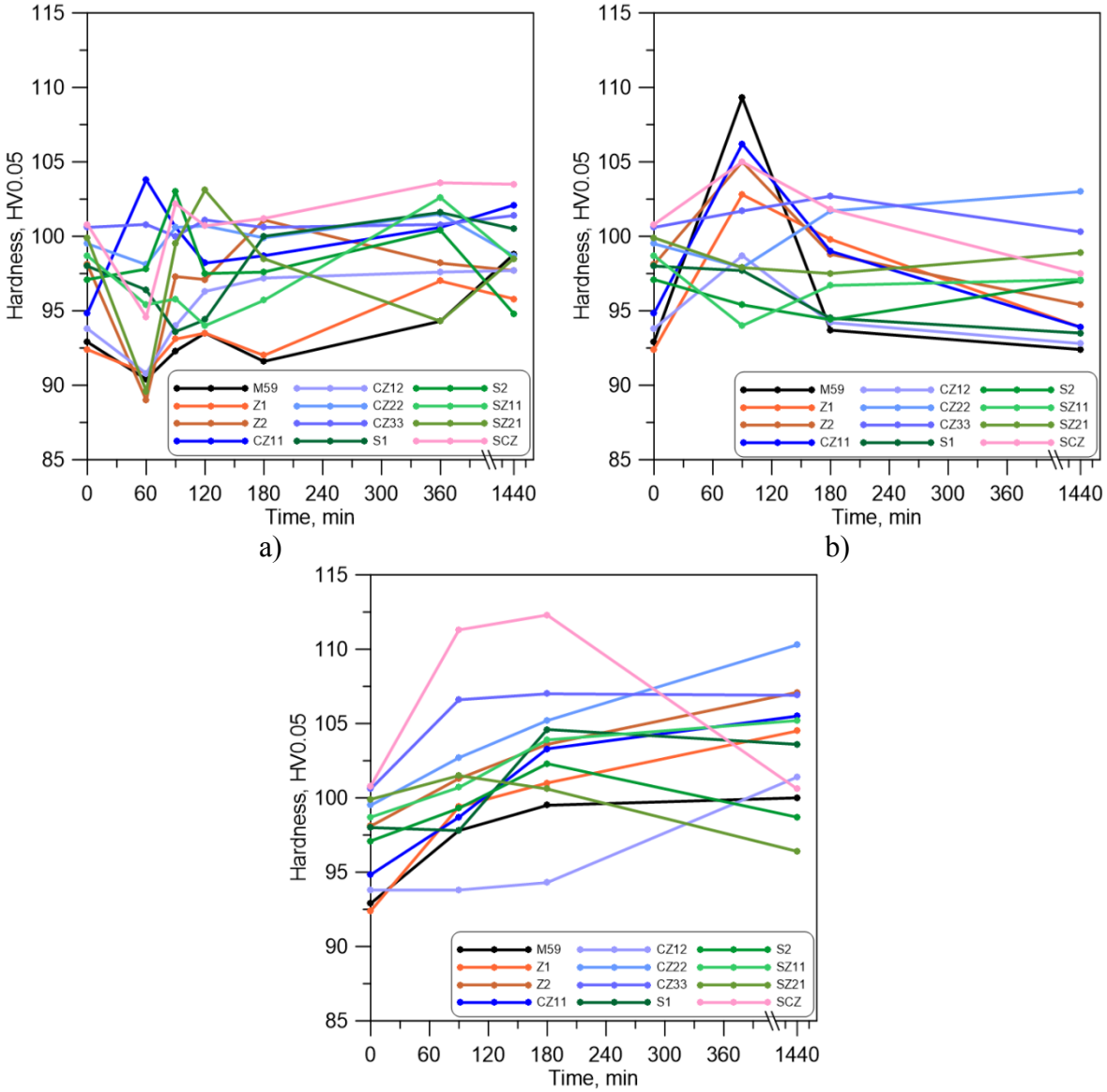

Microhardness as a function of a time at a) 125, b) 175 and c) 225 for all investigated alloys

Appendix A.5 Microstructure after heat treatment

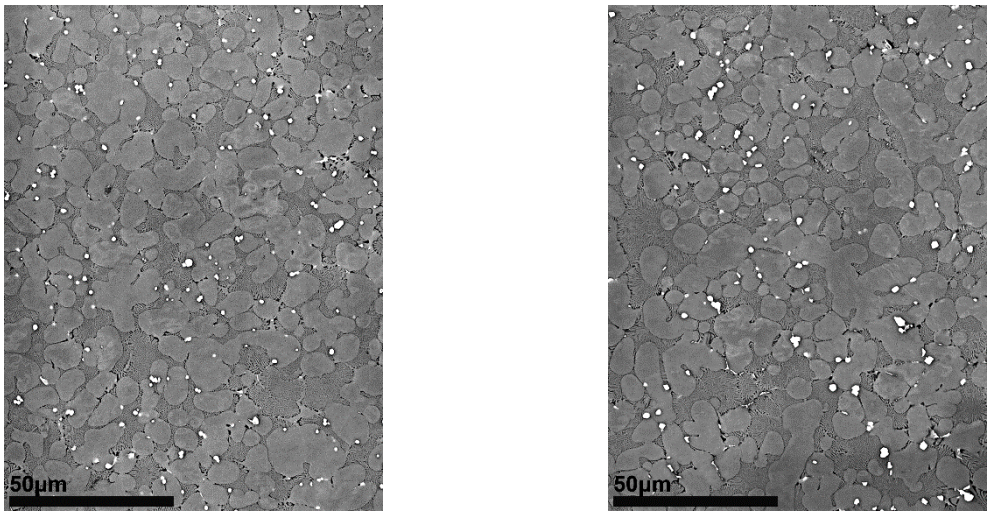

a) b)

SEM-images of the base alloy after artificial aging at a) 175ºC and b) 325 ºC [SC3[1]].

[1] O. Trudonoshyn, O. Prach, P. Randelzhofer, K. Durst, C. Körner „ Heat treatment of the new high-strength high-ductility Al-Mg-Si-Mn alloys with addition of Scandium, Zirconium and Chromium “. The paper is under review.

Appendix A.6 Tensile curves of the studied alloys in the as-cast state

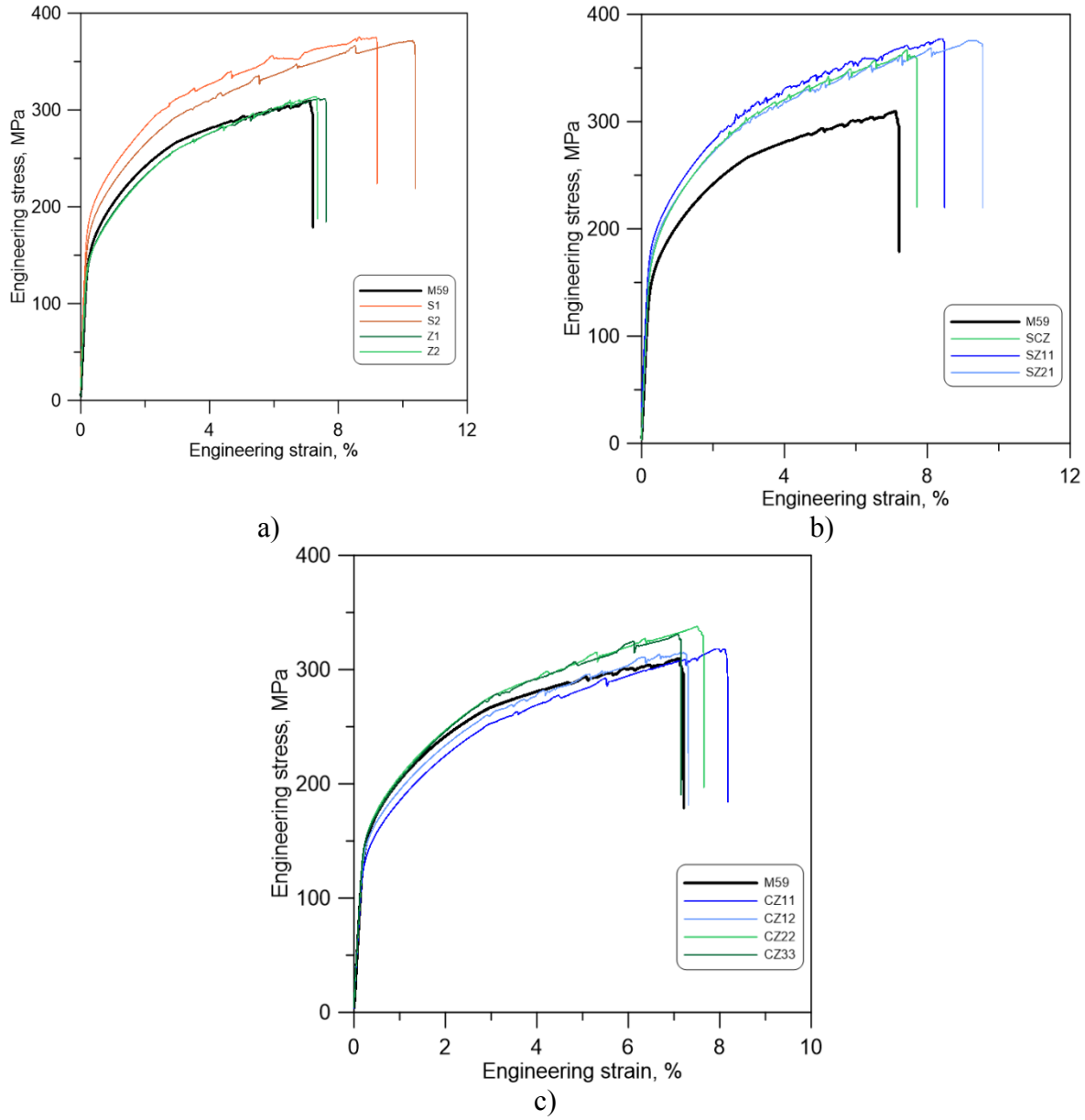

Comparative stress-strain curves for the a) alloys with a single addition and b-c) with combined additions in the as-cast state.

Appendix A.7 Summary of the properties of the studied alloys

Mechanical properties of a desingned alloys in as-cast state

Alloys		HB	YS [MPa]	UTS [MPa]	A [%]
M59 (base alloy)		79.6	163.9±5.6	299.8±6.3	8.3±0.5
Single additions	Z1	85.4	162.6±3.36	304.2±8.43	7.8±0.58
	Z2	84.9	161.8±3.66	296.2±8.58	7.0±1.13
	S1	89.8	190.0±7.1	332.8±9.5	9.3±1.6
	S2	90.9	196.2±6.7	341.9±4.5	10.1±1.1
Combined additions	CZ11	86.5	170.5±9.5	325.6±14.9	9.1±1.7
	CZ12	87.3	171.5±5.2	325.1±10.5	8.43±0.8
	CZ22	88.5	169.1±5.2	309.9±10.4	7.0±1.1
	SZ11	90.9	201.4±8.0	345.8±1.6	9.8±1.9
	SZ21	92.0	206.4±4.2	353.0±6.1	10.2±0.9
	SCZ	91.4	200.1±6.4	348.9±7.8	9.2±0.1

Tensile properties as a function of aging time after AA at 325°C

Alloy	Aging time, [hours]	YS [MPa]	UTS [MPa]	A [%]
M59	1	133.0±3.2	287.4±5.4	8.5±1.5
	3	133.0±2.6	286.5±6.7	9.0±2.4
	5	131.0±3.5	285.0±5.4	9.3±1.2
	15	118.0±5.4	271.2±7.6	12.5±3.4
Z1	1	133.1±2.0	280.2±6.0	7.6±0.5
	3	135.4±2.2	288.0±3.5	7.6±1.2
	5	135.0±2.6	287.0±12.8	11.0±3.4
	15	134.8±1.2	277.4±3.0	13.4±0.7
Z2	1	146.0±4.1	279.1±10.4	8.5±0.7
	3	148.0±4.3	287.0±7.8	10.5±0.5
	5	145.5±5.6	285.3±8.4	10.5±2.5
	15	145.0±3.5	278.2±4.5	11.9±1.2
S1	1	187.0±5.6	329.0±5.4	9.0±0.01
	3	191.7±4.7	331.7±4.6	9.7±0.014
	5	182.0±0.4	325.7±7.0	9.3±0.02
	15	168.7±2.0	318.6±1.0	9.7±0.02
S2	1	261.0±1.3	381.5±4.7	7.0±0.012
	3	265.0±1.2	385.6±5.6	7.0±0.014
	5	236.4±1.3	376.2±0.6	7.5±0.01
	15	215.4±1.6	357.7±1.2	9.7±0.015
CZ11	1	146.0±2.5	315.0±6.0	9.5±0.1
	3	147.6±1.6	318.8±5.8	10.8±1.1
	5	145.0±2.0	317.0±5.6	12.3±0.1
	15	142.0±2.0	305±7.6	13.0±1.2
CZ12	1	148.0±2.0	307.0±7.5	9.0±0.2
	3	149.0±3.0	311.4±13.0	9.0±0.2
	5	143.0±2.0	304.0±20.0	9.0±0.2
	15	140.0±3.0	201.0±7.0	11.0±0.1
CZ22	1	140.0±4.2	300.0±5.6	6.3±1.0
	3	148.7±2.5	304.7±7.2	6.3±0.5
	5	132.0±4.7	287.0±5.0	8.6±0.7
	15	130.0±7.2	276.0±6.5	9.0±1.5
SZ11	1	195.0±5.7	337.5±7.3	10.2±1.2
	3	197.5±5.0	340.1±8.6	10.8±1.1
	5	192.3±6.4	336±2.3	11.0±0.8
	15	175.0±7.0	333.3±5.3	12.2±0.7
SZ21	1	260.0±5.8	384.8±8.3	6.4±0.7
	3	262.5±5.0	388.4±7.8	7.8±0.7
	5	255.0±7.0	370.0±8.3	7.5±1.1
	15	235±5.0	370.4±5.3	8.2±0.4

Tensile properties as a function of aging time after AA at 225°C after 3h.

Alloy	YS [MPa]	UTS [MPa]	A [%]
M59	189.7±4.1	287.6±7.8	4.6±0.3
Z1	191.0±1.7	291.5±0.4	4.7±0.2
Z2	182.2±2.5	288.9±7.4	4.8±0.6
S1	204.5±5.0	326.9±5.3	8.3±0.6
S2	215.3±7.6	337.0±8.1	8.8±1.2
CZ11	187.7±8.7	298.8±12.2	5.9±0.1
CZ12	185.0±5.8	301.1±5.4	6.8±0.8
CZ22	194.0±4.2	290.5±16.3	4.3±1.0
CZ33	189.0±2.3	297.9±12.5	4.8±1.5
SZ11	209.9±10.9	329.1±7.3	7.5±1.2
SZ21	209.8±8.3	334.8±9.3	8.2±0.7

Tensile properties after solution treatment at 520ºC+AA for 3h.

Alloy	Aging temperature [ºC]	YS [MPa]	UTS [MPa]	A [%]
M59	225	130.0±6.6	242.0±11.5	11.5±1.1
	325	100.0±6.2	222.0±11.5	13.5±1.3
Z1	225	144.8±3.6	271.0±7.8	13.3±1.9
	325	100.0±2.0	271.6±8.7	14.5±2.3
Z2	225	155.8±5.2	280.0±7.0	13.1±1.5
	325	137.5±5.0	280.1±7.7	15.1±1.2
S1	225	130.5±3.5	257.5±7.5	15.7±2.5
	325	100.0±4.5	247.8±4.1	16.2±3.9
S2	225	138.5±4.0	263.7±6.7	14.2±3.3
	325	112.0±5.0	264.8±5.0	19.9±3.2
CZ11	325	100.0±3.0	228.5±5.5	14.2±1.2
CZ22	325	120.0±5.0	270.8±2.6	11.9±1.5
SZ11	325	110.0±2.0	254.6±2.6	15.1±1.1
SZ21	325	123.3±2.9	266.9±1.0	16.7±2.1

Acknowledgments

First of all, I would like to express my sincere appreciation to my superviser **Prof. Dr. Karsten Durst**, Head of Physical Metallurgy Department, Institute of Materials Science, TU Darmstadt, for giving me an opportunity to work as a Ph.D. candidate in one of the major research universities in Germany. Without his encouragements, continuous guidance and insight, I could not have finished this dissertation. His effort and patience will never be forgotten.

I would also like to thank my other committee members. **Prof. Dr.-Ing. habil Carolin Körner** for helpful discussions on the current research. **Prof. Dr. Wolfgang Ensinger** and **Prof. Dr. Wolfgang Donner** for their time and inputs.

The colleagues with whom I worked at TU Darmstadt for creating a friendly working environment, their technical support and helps over the year. I was very fortunate to share an office with **Dr.-Ing. Farhan Javaid** and **Dr.-Ing. Jörn Niehuesbernd**, who also gave me a lot of support, both technical and emotional.

I would also like to thank **M.Sc. Peter Randelzhofer** from WTM FAU for his support with castings and discussion.

Current research would not be possible without financial support by G**erman Academic Exchange Service (DAAD)**, Bonn, Germany. I would like to thank for giving me an opportunity to move to Germany and to pursue a PhD.

I am also very grateful to my best friend **Oleksandr Trudonoshyn** for his permanet support, invaluable discussions and friendship over the last 10 years.

Finally, I would like to acknowledge my family for their support over this time. And a special thank to **Ivan Krytskyi**, who believed in me when I doubted myself.

Publications and Contribution to scientific conferences

Publications

1. O. Prach, O. Trudonoshyn, P. Randelzhofer, C. Koerner, K. Durst, Multi-alloying effect of Sc, Zr, Cr on the Al-Mg-Si-Mn high-pressure die casting alloys. Materials Characterization Volume 168, 2020, doi:10.1016/j.matchar.2020.110537
2. O. Trudonoshyn, O. Prach, P. Randelzhofer, K. Durst, C. Körner, Heat Treatment of the New High-Strength High-Ductility Al-Mg-Si-Mn Alloys with Sc, Zr and Cr Additions, SSRN Electronic Journal. (2020). https://doi.org/10.2139/ssrn.3678844.
3. O. Trudonoshyn , O. Prach , A. Slyudova, V. Lisovskii (2020): Structure formation and multistep nucleation in casting Al-Mg-Si alloys, International Journal of Cast Metals Research, DOI:10.1080/13640461.2020.1822632
4. O. Prach, O. Trudonoshyn, P. Randelzhofer, C. Koerner, K. Durst, Effect of Zr, Cr and Sc on the Al–Mg–Si–Mn high-pressure die casting alloys. Materials Science & Engineering A Volume 759, 2019, doi:10.1016/j.msea.2019.05.038
5. Prach, O., Minnert, C., Johanns, K., Durst, K., A new nanoindentation creep technique using constant contact pressure. Journal of Materials Research, 34(14), doi:10.1557/jmr.2019.188
6. Azatuhi Ayrikyan, Olena Prach, Neamul H Khansur, Stephanie Keller, Shintaro Yasui, Mitsuru Itoh, Osami Sakata, Karsten Durst, Kyle G Webber, Investigation of residual stress in lead-free BNT-based ceramic/ceramic composites, Acta Materialia, 148 (2018), doi:10.1016/j.actamat.2018.02.014
7. O. Trudonoshyn, O. Prach, Multistep nucleation and Multi-Modification effect of Scandium in Hypoeutectic Al-Mg-Si Alloys. Heylion doi:10.1016/j.heliyon.2019.e01202
8. O. Prach, O. Trudonoshyn, M. Puchnin, Effects of chemical composition on mechanical properties of Al-Mg-Si-Mn based alloys. Materials Engineering - Materiálové inžinierstvo 24 (2017) 11-20 doi:ojs.mateng.sk/index.php/Mateng/article/view/215/399
9. M. Puchnin, O. Trudonoshyn, O. Prach, F. Pešlová, Comparison of ABI Technique and Standard Methods in Measuring Mechanical Properties of Aluminum alloys. Manufacturing Technology, 16 (2016) 3
10. O. Trudonoshyn, M. Puchnin, O. Prach. Use of ABI technique to measure mechanical properties in aluminum alloys: Effect of heat-treatment conditions on the mechanical properties of alloys. Mater. Tehnol., (2016), doi:10.17222/mit.2014.295
11. M. Puchnin, O. Trudonoshyn, O. Prach, Use of ABI technique to measure mechanical properties in aluminum alloys: Effect of chemical composition on the mechanical properties of the alloys. Mater. Tehnol., (2016) doi:10.17222/mit.2014.294
12. O. Prach, J. Horník, K. Mykhalenkov. Effect of the Addition of Li on the Structure and Mechanical Properties of Hypoeutectic Al-Mg2Si Alloys. Acta Polytechnica 55.4 (2015) doi:10.14311/AP.2015.55.0253

Contribution to scientific conferences

1. O. Prach, K. Durst, Development of a new Al-Mg-Si HPDC alloys with Sc addition, MSE, Darmstadt, 2018
2. O. Prach, K. Durst, Microstructure and local mechanical properties of new Al-Mg-Si casting alloys, INM-Leibniz Saarbrücken, 2016
3. O. Trudonoshyn, O. Prach, M. Puchnin, V. Boyko, K. Mykhalenkov, Design Of A New Casting Alloys Containing Li Or Ti+Zr And Optimization Of Its Heat Treatment. 23d International Conference "METAL 2014", Brno, Czech Republic, 2014